2018-03-15

A simplified down-hole method for monitoring an engineered hydraulic barrier using electrical resistivity tomography

Perrin, Robert

UNIVERSITY OF CALGARY

A simplified down-hole method for monitoring an engineered hydraulic barrier using electrical resistivity tomography

by

Robert Perrin

A THESIS

SUBMITTED TO THE FACULTY OF GRADUATE STUDIES

IN PARTIAL FULFILLMENT OF THE REQUIREMENTS FOR THE

DEGREE OF MASTER OF SCIENCE

GRADUATE PROGRAM IN GEOLOGY AND GEOPHYSICS

CALGARY, ALBERTA

March, 2018

Abstract

In the Athabasca Oil sands in Northern Alberta one of the major risks to mining operations is water infiltration from a saline aquifer at the base of the oil sands. One method of preventing infiltration is by the use of a freeze wall surrounding the mine pit. Monitoring a freeze wall of this scale can be difficult because of the scale of oil sands mining pits. This thesis explores the use of single-borehole electrical resistivity tomography (ERT) as a method of monitoring the entire freeze wall for leaks, which takes advantage of the freeze wall infrastructure to minimize monitoring costs.

The study was conducted by modelling a freeze wall breach, and then simulating an ERT data series from electrode arrays attached to the outside of the freeze pipes that were used to create the freeze wall. By using the freeze pipes for monitoring, the entire wall can be monitored while eliminating the need to drill additional wells for monitoring. The resulting simulated data were inverted using a simplified parameterized inversion scheme and were analyzed for their potential to show a leak in the freeze wall.

The results of the study indicated that the use of single-borehole ERT can be used to monitor for leaks along the entire freeze wall, and the inverted models can be used to automate a corrective action to fix the freeze wall at a leak location. The results also indicated that determining the volume of saline water that has leaked is not possible using this simplified inversion scheme.

Acknowledgements

I would like to thank my supervisors Dr. Adam Pidlisecky and Dr. Brandon Karchewski. Dr. Pidlisecky's enthusiasm is what drove me to pursue this project in the direction that it has gone and I am grateful for his mentoring. We have similar taste in bikes, so I knew this would work out. Dr. Karchewski has shown great patience throughout this process, watching me wander off in different directions to see for myself before reeling me back in, which has allowed me to grow in ways that I did not expect when I set out. I appreciated our monthly meetings where the topic of conversation would inspire my work, while adding a little spice (ie. the Banach-Tarski paradox).

I would also like to thank Dr. Dawson, Dr. Henderson, and Dr. Butler for inspiring me to pursue a graduate education. I would not have done this without their encouragement and support. I would also like to thank Pat, Drew, Adam, Ross, Maria, Megan, Cynthia, and Dave for humouring me and listening to my mad ramblings without heading for the exit.

I would also like to thank my parents for giving me the opportunities that I have had, that led me to where I am.

Finally, I would like to thank Sarah, Ben, and Rory for supporting me through my evening coding sessions and my weekends at the library. I greatly appreciate the hours that you have spent keeping me motivated throughout this process, and the weekends that you have given up while I have been playing mad science. If it weren't for your support, this would not have been possible.

Table of Contents

List of Figures and Illustrations

Chapter 1

Introduction

For the engineering of mine water management programs in the Athabasca Oil Sands in Northern Alberta, one of the hazards to mining operations is the presence of saline water beneath the oil sands. This risk was realized in 2009 when one of the major oil sands operators in the area flooded their mine pit with saline water from beneath the oil sand (Donovan, 2011). Since then, efforts have been made to either avoid mining in areas that may be prone to saline water intrusion, or find ways to mitigate saline water intrusion. One method of avoiding saline water intrusion is by building a "freeze wall" to hydraulically isolate the mining pit from the saline aquifer (Schmall and Maishman, 2007). Monitoring of these hydraulic barriers is typically done through a combination of temperature and water-pressure monitoring, but in certain cases these methods can fail, such as if there is a brine leak in the freeze pipes (Schmall and Maishman, 2007). There are some situations where monitoring of engineered hydraulic barriers has been done with electrical methods (Daily and Ramirez, 2000). Monitoring of the freeze wall creation and maintenance may benefit from the addition of electrical resistivity tomography (ERT).

ERT has been used from the surface for monitoring the movement of saline water (Hayley et al., 2009), but the depth of the saline aquifer beneath the oil sands means that surface ERT surveys would not be sensitive to the zone of interest. A solution to this is cross-borehole ERT, which images the resistivity structure between two boreholes (Slater, 2007). While cross-borehole ERT is an effective tool for mapping the distribution of electrical resistivities between boreholes, it is difficult to implement over a large scale to monitor a freeze wall; borehole pairs would need

to be installed at a fine interval over the length of the wall, which may be cost prohibitive for the project.

A method that may be effective in monitoring a freeze wall is single-borehole ERT from boreholes centred within the freeze wall. Single-borehole ERT is a cost-effective alternative to cross-borehole ERT as the freeze pipes used to create the freeze wall can be instrumented on their exterior, negating the need to drill additional monitoring boreholes.

In this thesis, I explore the potential use of single-borehole ERT to monitor a freeze wall in the Athabasca Oil Sands region. I will discuss the sensitivities of single-borehole ERT to both the thickness of the freeze wall and the resistivity of the surrounding formation; the relationship between leaking of saline water through the wall and its effect on the electrical resistivities measured; how single-borehole ERT data can be used to monitor the entire length of the freeze wall; and the limitations of using single-borehole ERT for this purpose.

1.1 Existing work

ERT is a technique that originated in the mid 19th century. Fox (1843, 1830a,b, 1838) performed experiments in which the electrical resistivity between veins of various metal ores and the surrounding host rocks were compared.

Following this early work, few advances were made until Wenner (1912) used a 4-pin resistivity measurement system called a Thompson Bridge to measure the resistivity of a material, where 2 of the 4 pins are used to conduct a current into the test material, and the other two pins are used to measure the resistance of the material. Wenner (1912) found that the technique was more effective in measuring the resistance of a material as there was no error due to the resistances of the mea-

surement apparatus. Wenner (1916) applied the resistivity measurement technique to measuring the effective resistivity of the ground by placing the 4 pin resistivity measurement system on the ground.

In the 1920's, Conrad and Marcel Schlumberger carried the work of Wenner forward and applied the 4-pin resistivity system to borehole electrical surveying in a method they called Electrical Coring (Schlumberger et al., 1932). There were several studies performed by the Sclumbergers from the 1920's to the 1940's where they showed that the method had significant promise for mapping variations in the resistivity of the subsurface from both the surface and from boreholes (Schlumberger, 1920a,b, 1927; Schlumberger and Schlumberger, 1928, 1930a,b, 1935; Schlumberger et al., 1933). The work performed by the Schlumbergers involved taking measurements of the apparent resistivities of the subsurface and making interpretations of their meanings directly from raw data curves without further analysis; many of their methods for downhole electrical resistivity logging are still in use today. They recognized the effect of total dissolved solids in porewater on the bulk apparent resistivity of the formation (Schlumberger et al, 1933) in what they described as the electrochemical phenomenon in boreholes.

From the geoelectric studies in the 1920's and 1930's the feasibility of this method for subsurface exploration was realized and there was an increase in the amount of research and development into the method for various purposes in the years after the Schlumbergers.

Following World War II, the destruction of infrastructure in Germany meant that it was necessary to secure local drinking water supplies (Hallenbach, 1952). One of the problems faced in the exploration for suitable drinking water aquifers in Germany was the location of saline ground water. This lead to the emergence of the field of hydrogeophysics, where the work conducted by the Schlumbergers in determining the effect of total dissolved solids on the apparent resistivity

of the ground was used to map the location of saline water in the subsurface (Hallenbach, 1952; Flathe, 1954). These methods for mapping the distribution of saline water in the subsurface were studied by several researchers over the next few decades, mostly for locating the saline water table in coastal areas (Krulc and Mladenović, 1969; Zohdy, 1964; Zohdy and Jackson, 1969).

Until the 1970's, the interpretation of electrical resistivity data were conducted by calculating resistivity data curves over simplified blocky models of various combinations and finding the simplified model that best fits the data (Pekeris, 1940). This forward modelling approach is described further in a detailed report for the USGS by Van Nostrand and Cook (1966). Marquardt (1963) introduced an algorithm called ridge regression that offered an improved method of estimating unknown parameters. Ridge regression was used in several later studies to invert resistivity data to estimate an earth model (Inman, 1975; Inman et al., 1973; Pelton et al., 1978).

With the spreading availability of computers in the 1970's and 1980's, and the emerging use of tomography in the medical imaging field, improvements in the interpretation of geoelectrical data were made by incorporating the improvements from these fields. Dines and Lytle (1979) describe how the methods being used for computerized x-ray tomography could be used to produce an earth model using cross-borehole electromagnetic instruments. The method described by Dynes and Lytle was a simplified approach that was one of the works that formed the basis for cross-borehole methods and surface methods that followed.

The early work in inversion of electrical resistivity involved solving for the resistivity of objects with fixed sizes and locations (Dines and Lytle, 1979; LaBrecque and Ward, 1988; Tripp et al., 1984). With improved computing power, Daily and Owen (1991) improved on these methods by solving for the resistivity of a uniform mesh of cells within the survey domain, which allowed inversion of more complicated resistivity structures than before. As computing power increased, and

with the improvement of inversion techniques for electrical resistivity data, cross-borehole resistivity techniques were used to track the movement of high TDS fluids (Binley et al., 1996; Daily, 1991; LaBrecque, 1996; Nimmer et al., 2008; Perri et al., 2012; Chambers et al., 2007; Slater et al., 1997; Slater and Binley, 1996; Schima et al., 1996). In addition to exploiting the electrical conductivity contrast between saline water and fresh water, ERT has been used for many other purposes such as monitoring CO_2 injection (Picotti et al., 2013; Commer et al., 2016; Bergmann et al., 2012); monitoring steam injection (Ramirez et al, 1993); monitoring engineered hydraulic barriers (Daily and Ramirez, 2000); and monitoring heat tracer experiments (Hermans et al, 2015). For projects where the zone of interest is deep, the resolution of surface ERT is very poor compared to cross-borehole ERT (Perri et al., 2012). For this reason, many of the projects where the zone of interest is deep use cross-borehole ERT as opposed to surface methods.

For cross-borehole ERT, the aspect ratio of the survey setup is the ratio of the borehole separation to the length of the instrumented zone. To maximize resolution, the optimal survey aspect ratio is 0.5 (LaBrecque, 1996), which means that the borehole separation needs to be half of the instrumented zone thickness (zone of interest). Figure 1.1.1 presents an illustration of the survey aspect ratio for a cross-borehole ERT survey. For monitoring at the depth of the Basal McMurray aquifer in the Athabasca Oil Sands, the zone of interest can be as thin as 5 m (Jo and Ha, 2013), which means that to achieve optimal resolution using cross-borehole ERT would require boreholes to be separated by 2.5 m. The tight borehole spacing requirements for cross-borehole ERT monitoring of freeze walls presents two significant issues: the costs associated with drilling monitoring wells at the density required to monitor the entire wall; and that the freeze wall thickness may approach the borehole separation, which will require a more complicated 3-D inversion approach to image changes out of the plane of the survey (Feng et al., 2014).

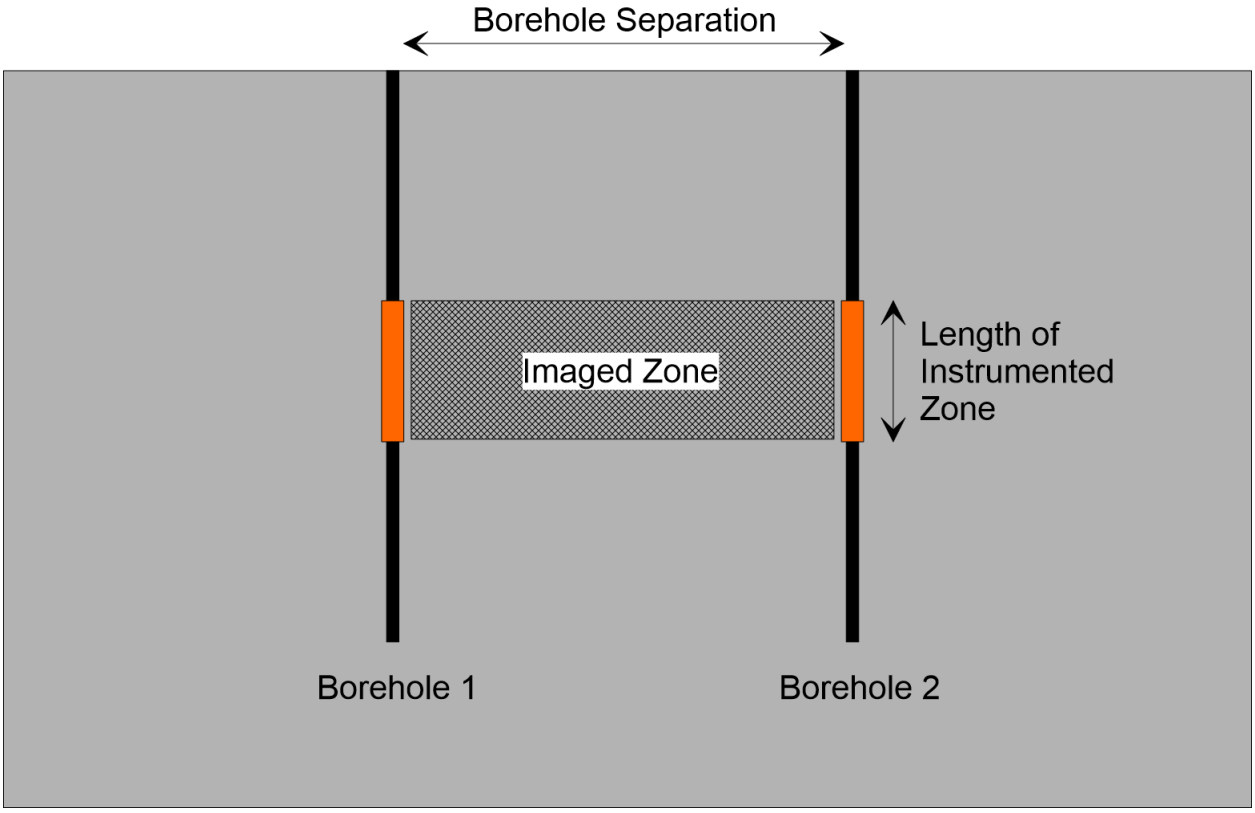

Figure 1.1.1: An illustration of the aspect ratio of a cross-borehole ERT survey. On each borehole, the instrumented zone is coloured orange, and the aspect ratio is the ratio of the borehole separation to the length of the instrumented zone.

1.2 Scope of the study

When designing a geophysical monitoring program, the scale of the project can have a major impact on the applicability of the methods. On a small scale, cross-borehole ERT has proven to be a very effective method for monitoring the migration of saline water in the subsurface, as shown by many authors (cf. Binley et al., 1996; Daily, 1991; LaBrecque, 1996; Nimmer et al., 2008; Perri et al., 2012; Chambers et al., 2007; Slater et al., 1997; Slater and Binley, 1996; Schima et al., 1996). On the scale of a freeze wall that would be required to protect an oil sands mining pit (several kilometers), cross-borehole ERT may provide information across the wall at specific locations, but is not suitable as a complete geophysical monitoring solution for the entire wall. A more useful geophysical monitoring solution for a freeze wall of this scale should achieve the objectives of the geophysical survey without disrupting the other aspects of the design of the freeze wall. Installation of the freeze wall requires drilling of holes for cooling pipes; if these pipes were instrumented with electrode arrays, it would reduce the additional cost of monitoring since separate monitoring boreholes would not need to be drilled, and since the freeze pipes need to be installed along the entire route, the entire length of the freeze wall could be monitored. To deal with the volume of data that this setup would require, it may be more efficient to treat each monitoring location as a single 1-D survey and to combine the results of all of the wells to determine the location of a leak and to trigger a necessary response.

This study explores the use of single-borehole ERT as a method to monitor the health of the freeze wall to address the following questions:

1. Can the method detect a breach in the freeze wall?

2. Can the method quantify the amount of contaminant that leaks across the wall in

the case of a breach?

These questions are explored throughout this thesis while considering the role of the geophysical monitoring within the context of the mining operation that the freeze wall is protecting. The geophysical monitoring method that this thesis discusses is meant to allow the mining operation to be aware of a leak in the freeze wall and to take actions to repair the wall.

It is important to consider what effort level is required to achieve the specific goals for the project, and what the benefits of additional efforts would be. With all geophysical methods, there is limited data available to understand relatively complex problems, and because of this there are always ways to refine the result of a survey. An example of this is inversion: inversion of geophysical data provides a more refined view of the subsurface than the raw data, but inversion comes at a computational cost. The goal of this project is to answer the questions stated above while providing some understanding of what the optimal combination of the usefulness of the survey results and the computational effort required to achieve those results.

1.3 Contributions of this research

This research is intended to demonstrate how a simplified approach to geophysical imaging can be used to aid in the detection of a very specific situation. In this work the aim of the geophysical imaging is only to detect if there is a leak or not, which does not require the level of imaging that is typically performed with geophysical surveys and can be accomplished by making simplifying assumptions in the approach to geophysical imaging. This type of simplified geophysical detection has the potential to aid in a wide range of engineering projects that require real-time detection of changes in the physical properties of the earth. This research approaches the problem of leak

detection in a way that can be framed as a classification problem, which is an ideal problem to apply recent advances in machine learning to. The next steps for this research may involve the use of machine learning to detect leaks in a freeze wall to understand how it can be used for earlier detection, or for detection with a higher degree of certainty in the presence of noise.

Chapter 2

Background Information

This section provides context and background theory on the following elements of the freeze wall monitoring system that this thesis investigates:

1. the regional setting
2. freeze wall
3. the ERT method
4. the use of single-borehole ERT, including advantages and limitations
5. inverse methods for single-borehole ERT

These items will be discussed in the following subsections.

2.1 Regional setting

Open-pit oil sands mining in the Athabasca Oil Sands region takes place on a large scale, there are approximately 475,000 Ha of surface mineable oil sands, and of this, 89,500 Ha is under active development in some way (Government of Alberta, 2017). In portions of the Lower McMurray Formation, there are zones where the sands are saturated with water instead of oil, often referred to as the basal McMurray aquifer (Hackbarth, 1980). In some areas, the basal McMurray aquifer can have high salinity, due to the dissolution of an evaporite layer within the underlying Devonian section (Broughton, 2013; Mahood et al., 2012). The mechanism by which the basal McMurray

aquifer becomes connected to the deeper saline aquifer, while interesting, is beyond the scope of this study. While dewatering during mining operations is a common practice, it becomes complicated when the water being removed is saline, as this water needs to be treated prior to disposal.

The general stratigraphic section through the mining zone consists of the McMurray Formation underlain by the Devonian limestone. Figure 2.1.1 presents a schematic cross section for the region, with the McMurray Formation plotted in black.

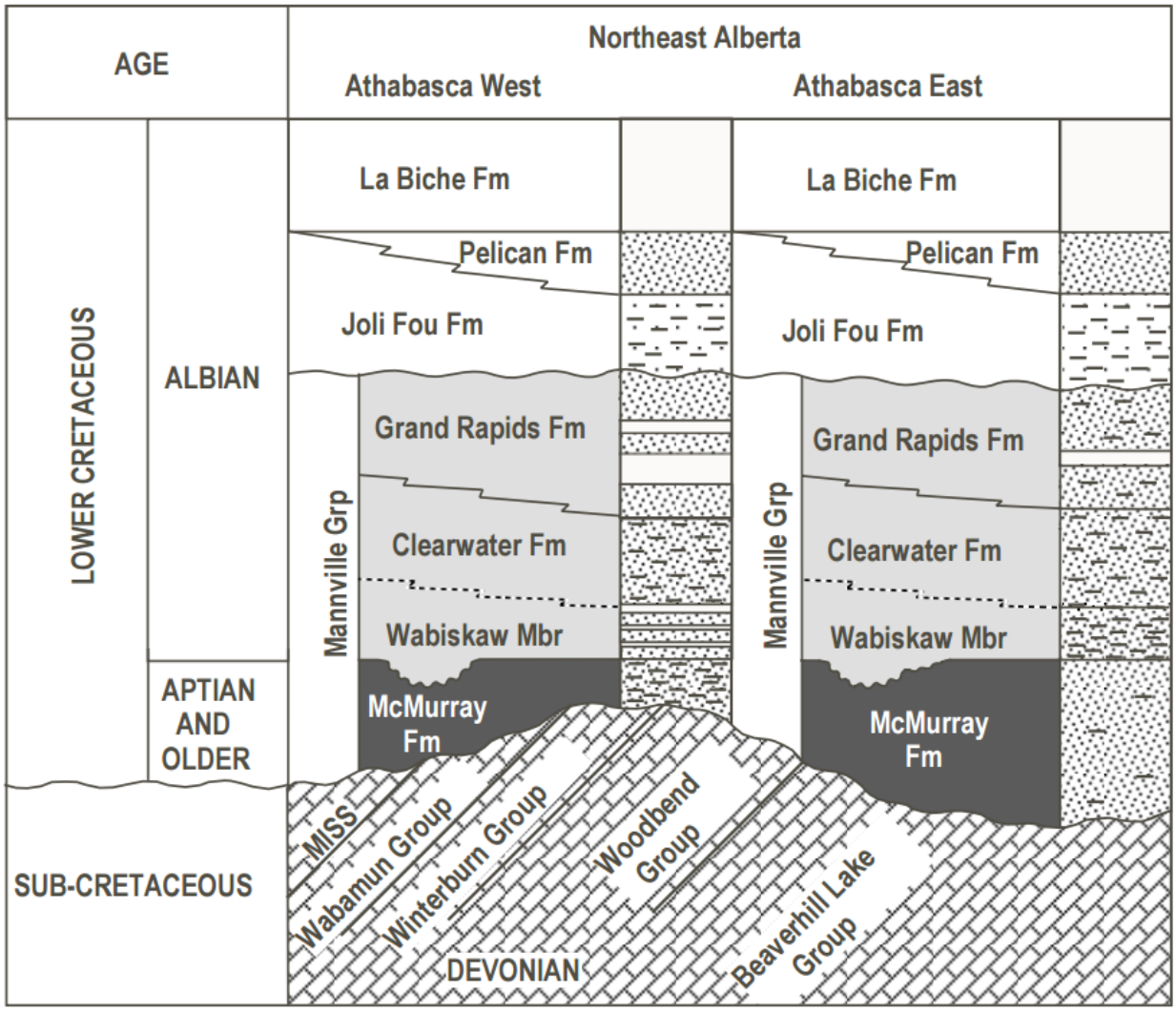

Figure 2.1.1: Schematic cross-section, Fort McMurray area (Wightman and Pemberton, 1997)

The basal McMurray aquifer, where it is present, sits at the base of the McMurray, on top of

the Devonian. Figure 2.1.2 presents a sample well cross section through the oil sands, which forms the basis for which the geological model for the tests in this thesis.

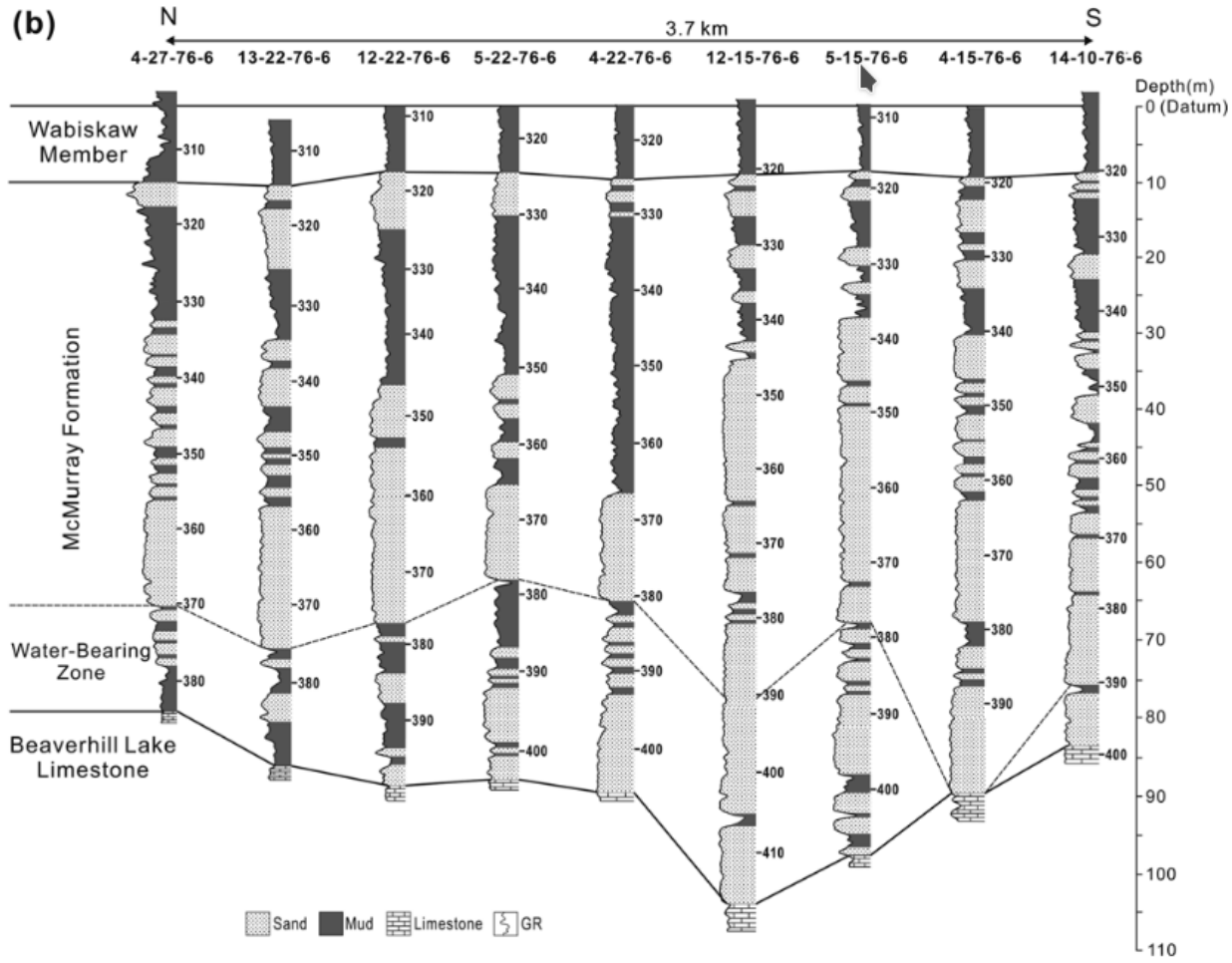

Figure 2.1.2: Well log cross-section, Fort McMurray area (Jo and Ha, 2013)

The basal McMurray aquifer has a relatively high hydraulic conductivity compared to the surrounding layers (Hackbarth, 1980), meaning that during mining operations the basal aquifer presents a pathway for water to enter the mine; it is this infiltration that the freeze wall is meant to prevent.

2.2 Freeze wall

Artificially freezing the ground has been used as a means for controlling groundwater flow for excavations for over 100 years (Schmall and Maishman, 2007; Sopko, 2017). It involves drilling pipes (high density polyethylene (HDPE) or steel) at a dense interval over the span of the proposed frozen zone and circulating a chilled brine through the pipes to freeze the surrounding ground. Figure 2.2.1 presents a schematic of a freeze wall.

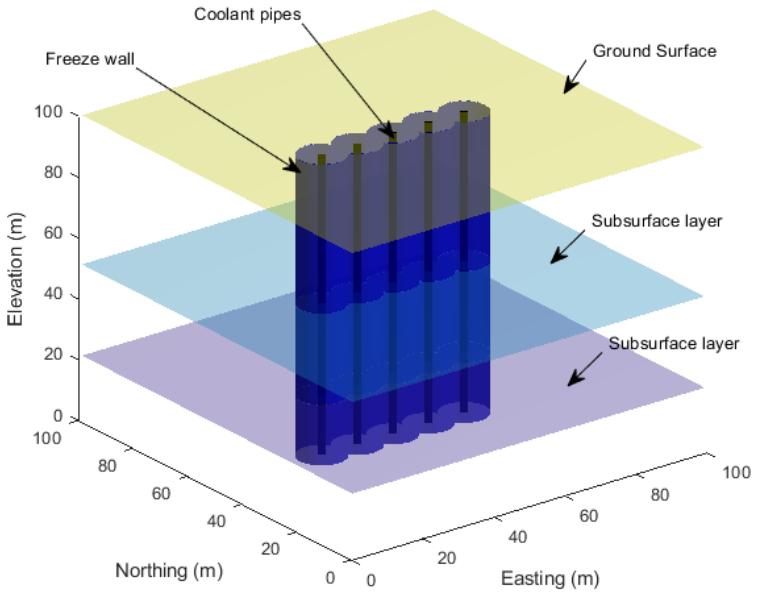

Figure 2.2.1: Schematic of a freeze wall (modified from Sopko, 2017)

For the creation of a long-term freeze wall, a dense array of freeze pipes may be used during the formation of the wall (Figure 2.2.2), and once the wall is created every second pipe may be turned off during the maintenance phase to prevent overgrowing the wall and to reduce refrigeration costs.

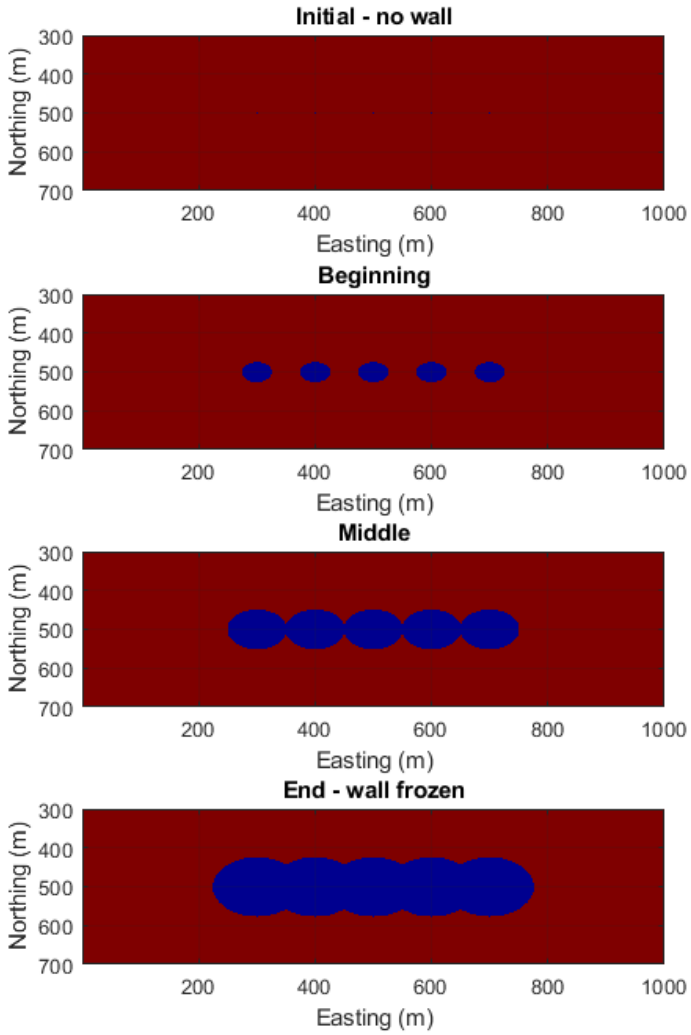

Figure 2.2.2: Schematic of the creation of a freeze wall (modified from Sopko, 2017). The freeze wall is blue and the surrounding soil is red.

In some cases, changes in the movement of groundwater may cause a thinning of the freeze wall which will require the wall to be repaired. Methods of repairing sections of the freeze wall include drilling additional freeze wells or changing the brine temperature (Sopko et al., 2013). For a wall that is in maintenance, the order of repair steps from least to most costly would be: turn

on the freeze pipes in the affected area; change the brine temperature; and drill additional freeze wells.

2.3 Electrical Resistivity Tomography (ERT)

Electrical resistivity tomography (ERT) is a geophysical method that is used to map variations in electrical resistivity across a survey area. The ERT method is based on Ohm's Law for resistance across a circuit, which states:

$$R = V/I \tag{2.1}$$

where R is the electrical resistance,

V is the voltage (potential) difference across the circuit,

I is the electrical current.

When applied over a bulk of soil, the resistivity becomes a function of resistance, cross sectional area, and length of the sample:

$$\rho = R\frac{A}{l} \tag{2.2}$$

where ρ is the resistivity,

R is the resistance,

A is the effective cross sectional area,

l is the effective length of the sample.

The ERT method uses the concept presented in equation (2.2) to map the distribution of electrical resistivities in the ground by applying current between an electrode pair, known as a dipole, and measuring the electrical potential difference at dipoles at different points along a survey area. Figure 2.3.1 presents a schematic that illustrates a sample ERT survey setup. In Figure 2.3.1, the current dipole is marked by electrodes A and B; the dipole generates current flow lines that radiate

outward from the current dipole and create lines of equal electrical potential normal to the current flow lines. Electrical potential differences are measured at the dipole marked by electrodes M and N in Figure 2.3.1, and are used to estimate the electrical resistivity of the ground through which the current is flowing.

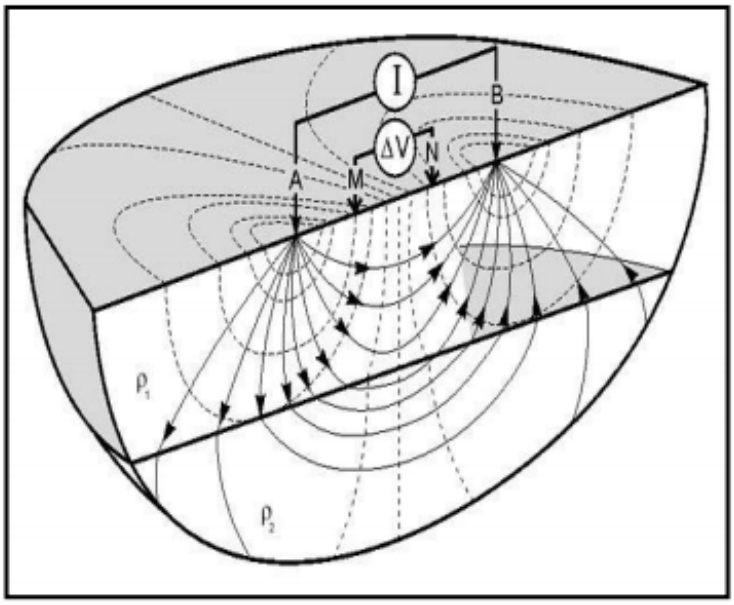

Figure 2.3.1: Conceptual schematic of electrode setup (Meligonitis et al., 2016). Current electrodes are labelled A and B, potential electrodes are labelled M and N, and the equipotential lines are indicated by dashed lines.

Apparent resistivities, which are an estimated average resistivity between the dipoles, are calculated through the following equation:

$$\rho_a = K\frac{\Delta V}{I} \tag{2.3}$$

where ρ_a is the apparent resistivity,

ΔV is the voltage difference across the potential dipole,

I is the current,

K is the geometric factor.

The geometric factor K, can be defined generally as

$$K = \frac{2\pi}{\left[\frac{1}{AM} - \frac{1}{AN} - \frac{1}{BM} + \frac{1}{BN}\right]} \tag{2.4}$$

where A and B are the current electrodes,

M and N are the potential electrodes.

The electrical potential field generated when current is passed across an electrode dipole can be described using Poisson's equation, which states:

$$-\nabla \cdot (\sigma \nabla \phi) = I(\delta(r - r^{+}) - \delta(r - r^{-})) \tag{2.5}$$

where σ is the electrical conductivity model,

ϕ is the potential field,

I is the input current,

δ is the Dirac delta function,

r^{+} and r^{-} are the locations of the positive and negative current electrodes respectively.

The survey setup illustrated by Figure 2.3.1 is on the ground surface, but the method is also commonly applied down boreholes (Slater et al., 2000; Binley et al., 1996). Figure 2.3.2 presents an example of a cross-borehole electrode configuration, where the zone that is imaged is the region that lies between the boreholes. In the cross-borehole electrode configuration, the current-potential dipole setup that was presented in Figure 2.3.1 is not applied; instead, configurations are used

that place the current electrodes in one borehole and the potential electrodes in the other borehole (dipole-dipole array), or configurations that place the current dipole across the boreholes and the potential dipole across the boreholes (cross-borehole array) (LaBrecque, 1996). Figure 2.3.3 presents a schematic of these two cross borehole electrode configurations.

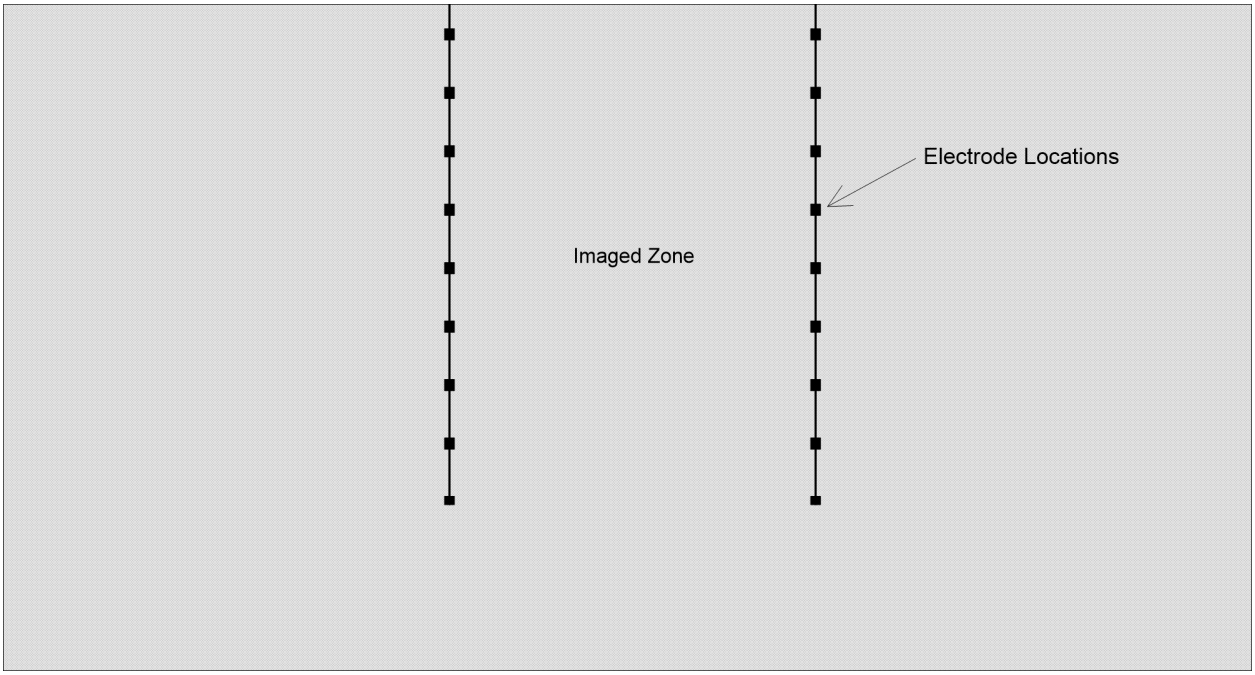

Figure 2.3.2: Conceptual schematic of downhole electrode setup in the cross-borehole configuration

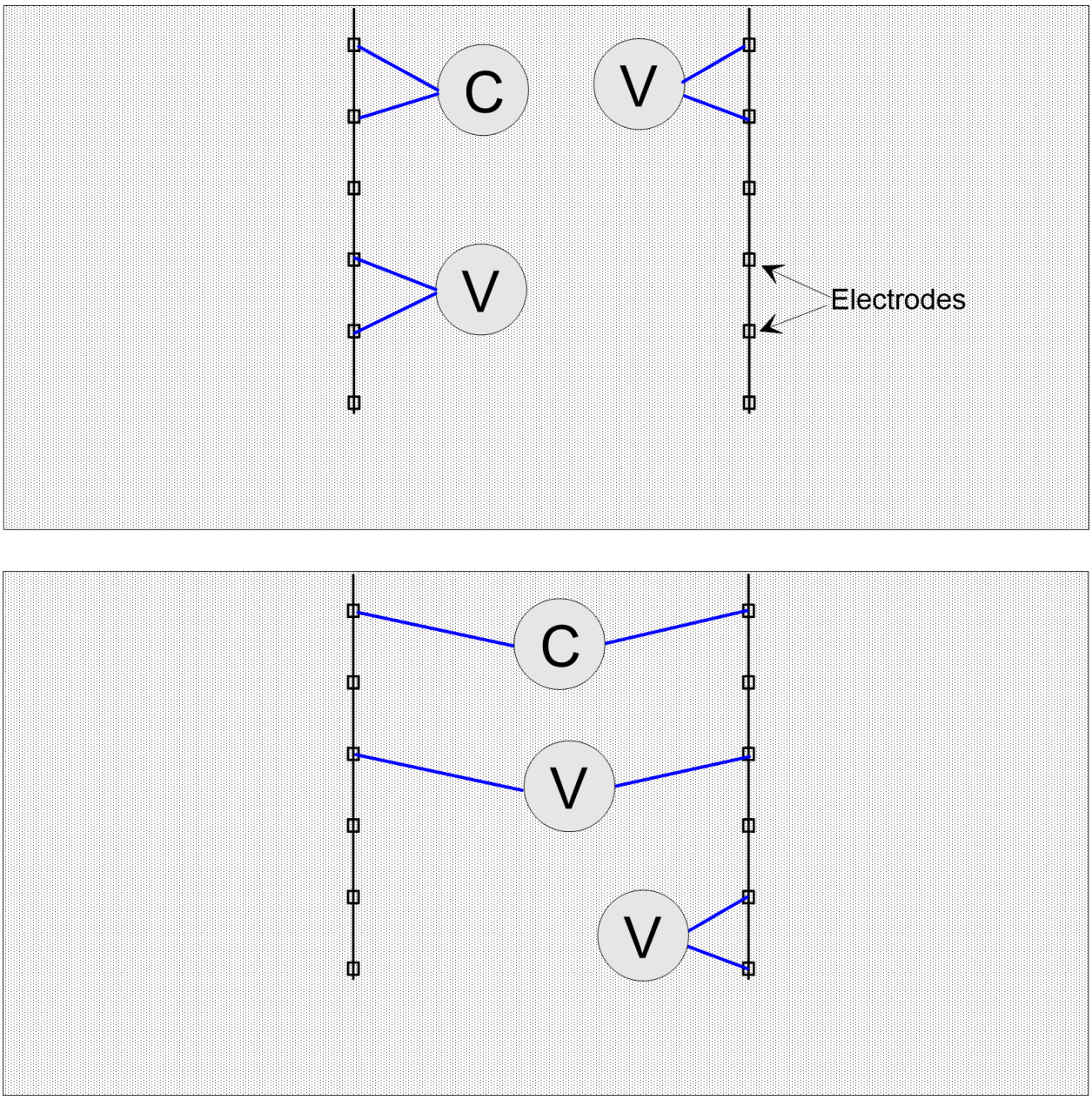

Figure 2.3.3: Schematic diagram of two cross-borehole electrode array configurations (modified from LaBrecque, 1996). The upper schematic illustrates the dipole-dipole configuration, and the lower schematic illustrates the cross-borehole configuration.

2.4 Single borehole ERT

While the cross-borehole and 3-D borehole ERT configurations have been shown to have strong potential when mapping saline water movement, they are not practical for monitoring a hydraulic barrier on the scale of a mine pit for several reasons including the costs associated with drilling enough holes to cover the survey area. A drawback of 3-D borehole ERT that may have an impact on its use in this case is the reduced sensitivity of 3-D ERT away from the boreholes (Singha and Gorelick, 2005); this may make it difficult to image resistivities that are out of the plane of the freeze wall. One possible alternative to cross-borehole or 3-D borehole ERT is single-borehole ERT. An illustration of the single-borehole electrode configuration is presented in Figure 2.4.1.

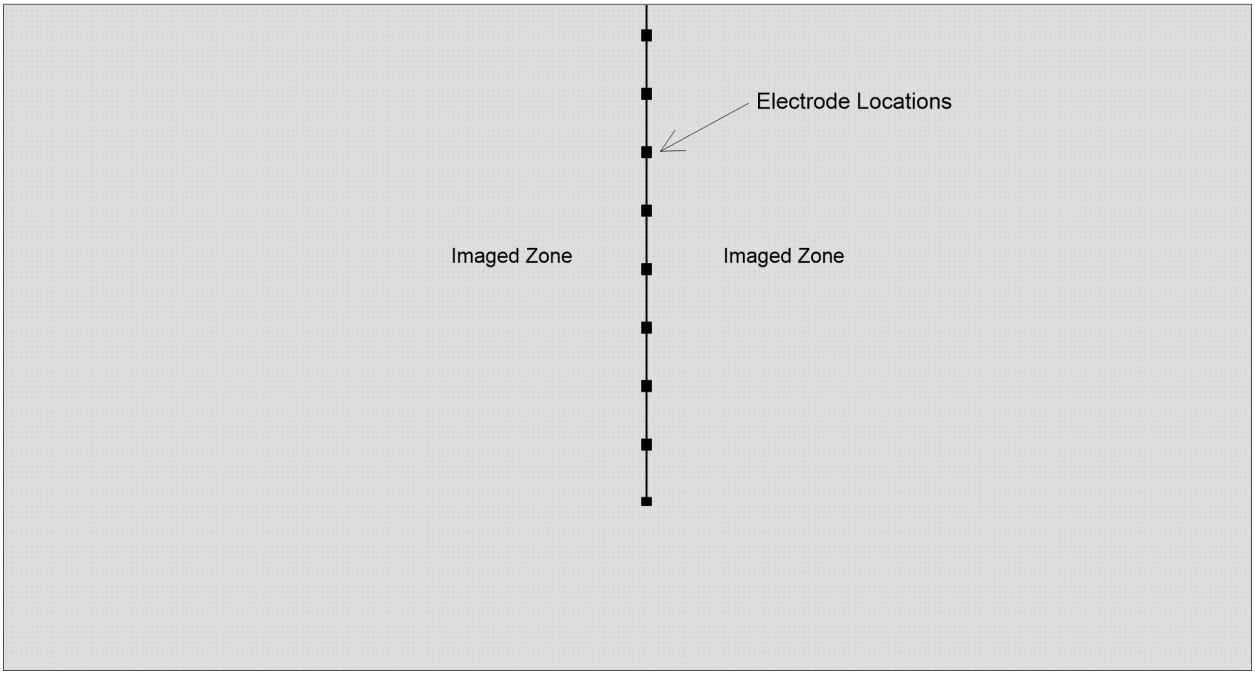

Figure 2.4.1: Conceptual schematic of downhole electrode setup in the single borehole configuration

Single boreholes have been used to conduct deep ERT surveys (Friedel et al., 2004; Tsourlos et al., 2003). Single boreholes have also been used to monitor water content changes in the vadose

zone Pidlisecky et al. (2013). There are a number of advantages to using single-borehole ERT instead of cross-borehole ERT: the number of boreholes required is half, which reduces installation costs substantially; qualitative interpretations of single-borehole ERT can be made very rapidly based on the raw data, which reduces data analysis costs; and it is far less computationally intensive to perform a sensitivity analysis in 1-D..

In the case of the conceptual freeze wall presented in Figure 3.1.2, the freeze pipes that are used to create the wall can be used to hold the instrumentation; downhole electrode arrays can be mounted on the outside of the freeze pipes. This offers an opportunity for cost savings as it requires no additional drilling for ERT monitoring holes, while offering an array of holes at a tight spacing along the freeze wall.

2.4.1 Limitations of single borehole ERT

The major limitation to using single-borehole ERT is that there are directional ambiguities in the results (Tsourlos et al., 2003). This means that it is possible to determine that there are variations in bulk resistivity as the radial distance from the borehole increases, but it is not possible to determine in which direction the changes occur, only an azimuthally averaged effect. Figure 2.4.2 presents an illustration of this concept.

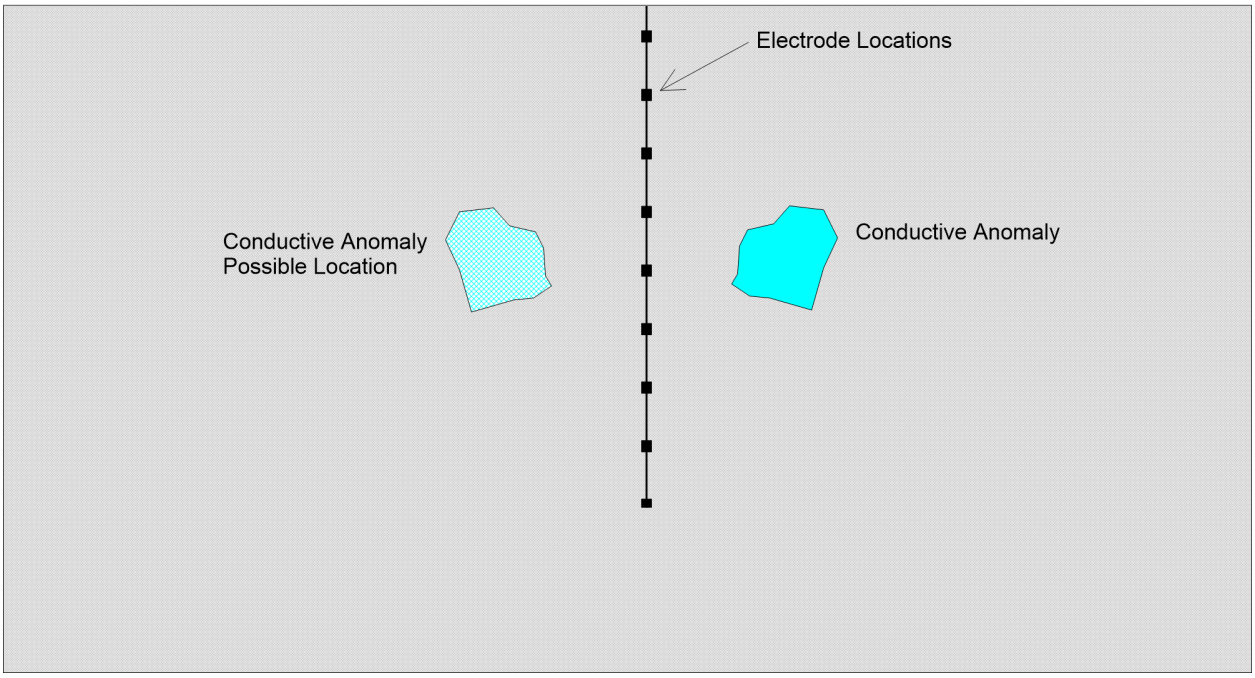

Figure 2.4.2: Illustration of the directional ambiguity associated with single-borehole ERT. In the image, a conductive anomaly exists on the right side of the borehole, but the survey data would be indistinguishable from the survey data if the anomaly was on the left side of the borehole.

The directional ambiguity may be a limitation when using a single borehole ERT setup by itself, but the specific situation in this thesis helps to negate the drawbacks of the single borehole setup. In this monitoring setup, the objective of the survey is to identify a leak and to determine its location. In the case of a leak, it is known which side of the wall the conductive anomaly will be on (the mine side), so the directional ambiguity is inconsequential. The location of the leak may still be determined using the results from several of the boreholes surrounding the leak.

2.5 Inverse methods

In geophysics, inversion is the process of estimating the physical properties of the earth from the measured effects of the survey. The physical property depends on the type of survey being performed; in the case of ERT, the physical property is electrical resistivity. The estimated earth model is the one that, when a geophysical forward model is applied to it, gives the lowest possible misfit between the modelled data and the real data. Residual misfit, or error, can come from a number of sources including: error in the measurement locations; noise in the measured data; an inaccurate mathematical model describing the earth; or an inaccurate numerical approximation of the mathematical model.

A common approach to inversion is a pixel-based approach such as tomography. In this approach, the earth within the survey domain is discretized into cells and the inversion estimates the physical property for each cell. A commonly used ERT inversion software package (Loke, 1999) performs this type of inversion. Figure 2.5.1 presents an example of the type of estimated earth model for this process. The type of inversion model presented in Figure 2.5.1 is a good approach in an exploration setting where there is not a lot known about the survey domain and it is important to map the variations in resistivity throughout the area. One of the drawbacks to this method, especially as the domain size increases, is the computational cost: each cell represents one parameter that requires a solution in the inversion, which can be computationally expensive. Another drawback is that this type of inversion is often under-determined, meaning that there are more parameters than there are unique data points and for which there is not one unique solution. Under-determined problems such as this require regularization in the form of smoothing to obtain a unique solution.

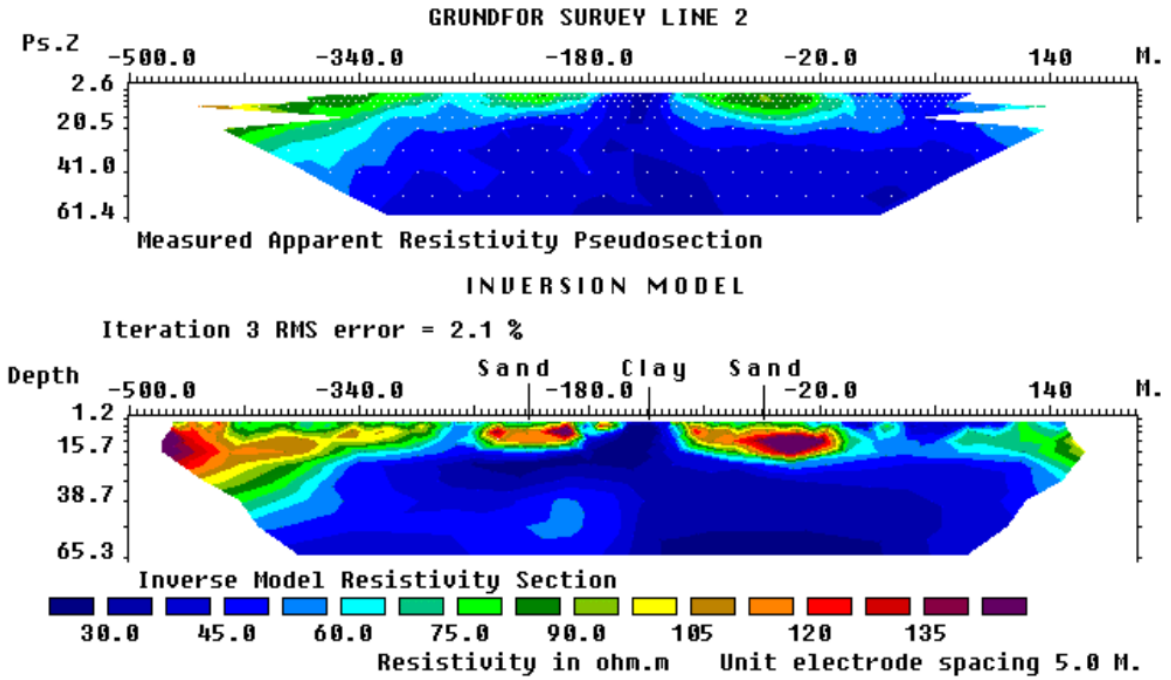

Figure 2.5.1: Illustration of a typical pixel-based ERT inversion output (Loke, 1999). The upper slide shows the survey apparent resistivities, and the lower slide shows the inverted resistivity model.

In surveys where the objective is more specific than exploration, a simplified parametric inversion approach can help to overcome the drawbacks of the commonly used pixel-based approach. In a parametric inversion approach, the model parameters are reduced to only specific parameters related to the goals of the project. This type of inversion requires some a priori information about the survey domain, as there are assumptions that must be made in the parameterization. A simple example of this type of inversion would be solving for the depth to the interface between a clay and sand unit, if you knew that there was a clay and a sand unit. This type of inversion greatly reduces the number of parameters, which has the effect of reducing computational cost and helping to avoid the use of regularization.

For the freeze wall a simplified parametric inversion approach would be appropriate because the area surrounding the boreholes is mapped and the objective of the monitoring survey is specific: identify a change in resistivity on one side of the freeze wall.

Chapter 3

Proposed Experimental Method

Since the freeze wall for this thesis is hypothetical, there are a number of steps required to explore the monitoring solution. Figure 3.0.1 presents the steps that were used in this experimental procedure.

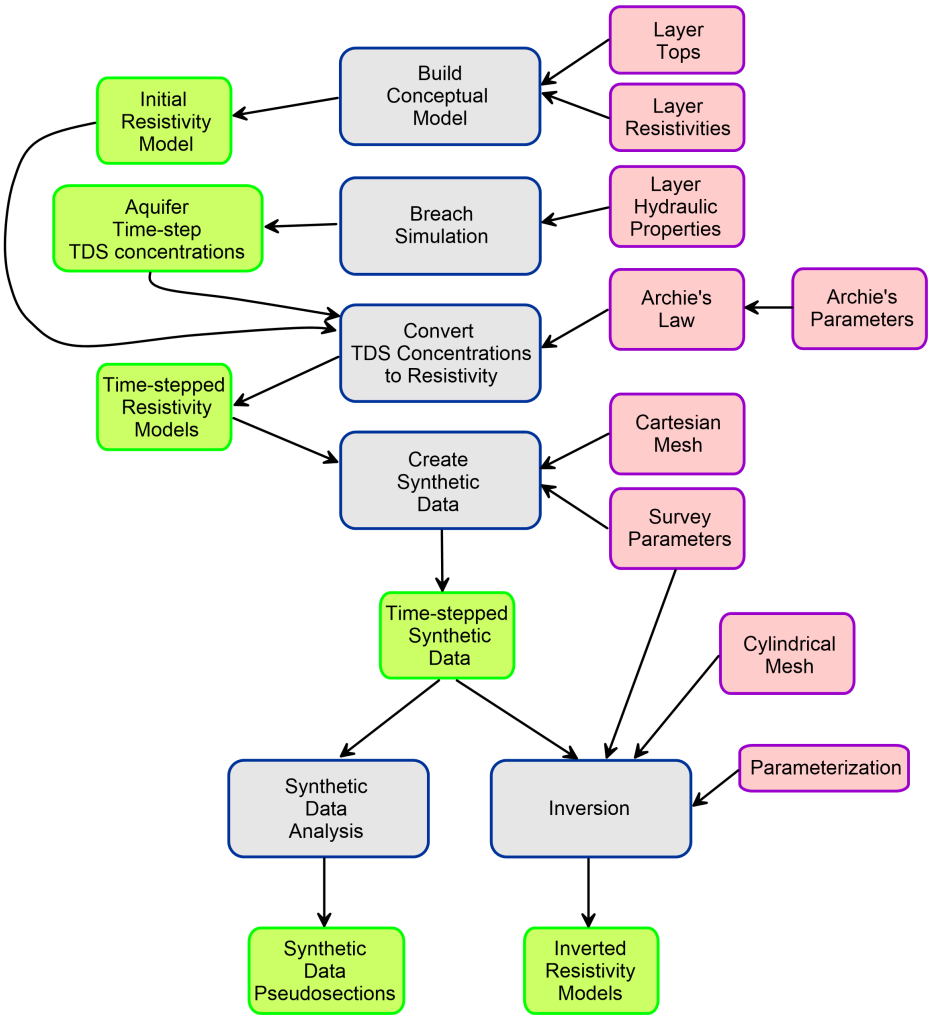

Figure 3.0.1: Proposed experimental method flowchart. Processes are shaded blue, process inputs are shaded purple, and process outputs are shaded green.

These steps are detailed further in the following subsections.

3.1 Build conceptual model

For this thesis, the initial scenario is a simplified case where the oil sand resource is underlain by a very saline basal aquifer which is being separated from the active mining area by a freeze wall. Figure 3.1.1 presents a schematic that illustrates the simplified freeze wall.

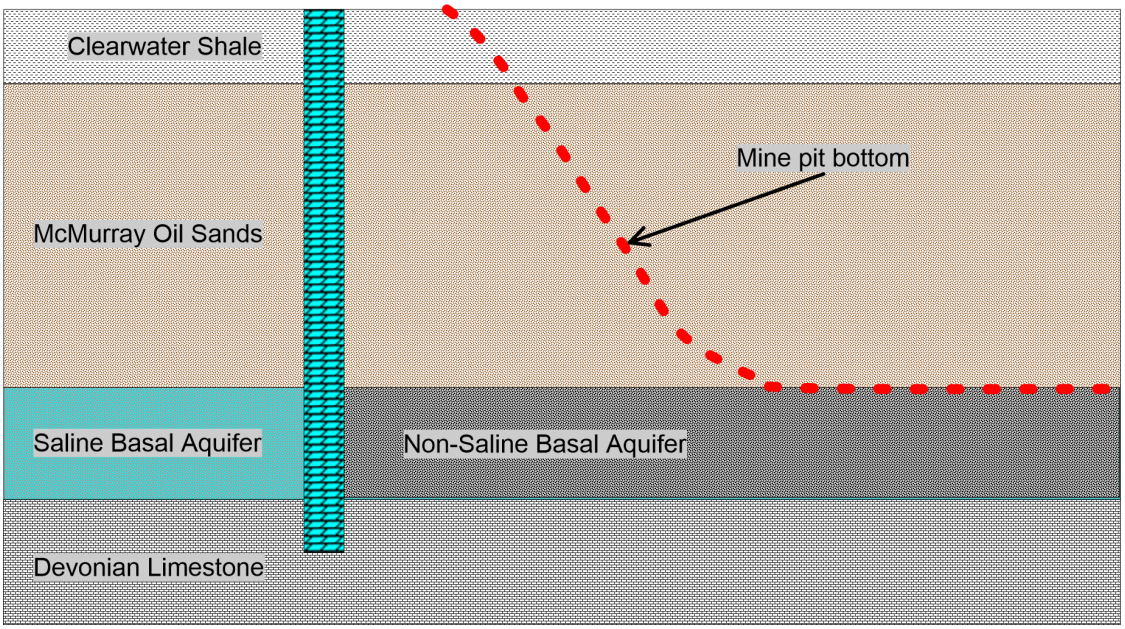

Figure 3.1.1: Simplified stratigraphic section for this thesis. The freeze wall is shown as a vertical wall separating the saline basal aquifer from the mine pit. The mine pit bottom is represented by a red dashed line.

In the ideal case, such as the one illustrated in Figure 3.1.1, the saline basal aquifer will be isolated from the mine pit side of the wall; and after pumping and disposing of the saline water on the mine side of the wall it will be non-saline.

Figure 3.1.2presents a plan view of a length of the freeze wall. The freeze wall is created by drilling tightly spaced holes along the wall alignment, inserting plastic casing into the holes, and pumping cooled brine through the casing. The freeze pipes are also the ERT monitoring well

locations proposed by the current study; at each well, the electrode array will be mounted to the outside of the freeze pipe.

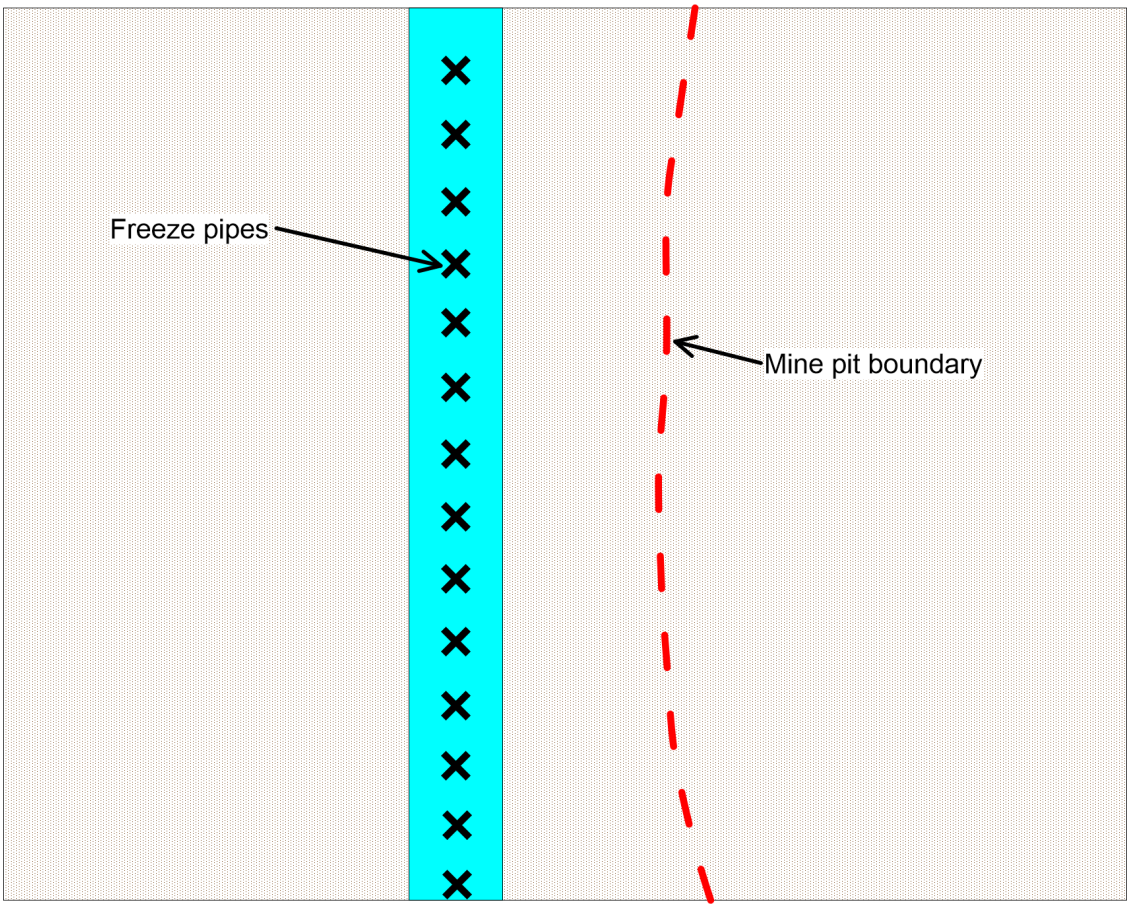

Figure 3.1.2: Map view wall layout. The freeze pipe locations are indicated with X's.

3.2 Breach simulation

The simulation of the freeze wall breach for this thesis is beyond the scope of the project and has been conducted in a simplified way that gives an estimate of how a breach may propagate, but is missing many of the complexities that would be present in a detailed simulation of a freeze wall breach. The intent of the breach simulation is only to provide context for the simulation of the survey data, which is the scope of this project. To simulate the freeze wall breaches for this

thesis, it is assumed that the breach takes place only in the basal aquifer, and that the layers above and below the aquifer are aquitards. This simplifies the contaminant transport problem from a 3D problem to a 2D problem. To simulate the breach, the following simplified contaminant transport equation that considers the dispersion and advection components of contaminant transport (Duriez, 2005) was used:

$$\frac{\partial C}{\partial t} = \left[D_x \frac{\partial^2 C}{\partial x^2} + D_y \frac{\partial^2 C}{\partial y^2}\right] - \left[v_x \frac{\partial C}{\partial x} + v_y \frac{\partial C}{\partial y}\right] \tag{3.1}$$

where C is the concentration of the contaminant;

D_x and D_y are the dispersion coefficients in the x and y directions respectively;

v_x and v_y are the pore water velocities in the x and y directions respectively.

The velocities v_x and v_y are calculated using Darcy's Law

$$v = \frac{K}{n_e} \frac{\partial h}{\partial l} \tag{3.2}$$

where K is the hydraulic conductivity;

n_e is the effective porosity;

$\partial h / \partial l$ is the hydraulic gradient.

The time series update was calculated on a Cartesian mesh with 1 x 1 m cells and a 1 second time step using a forward time difference approximation to equation (3.1)

$$C_{t+\Delta t} = C_t + \left[D_x \frac{\partial^2 C}{\partial x^2} + D_y \frac{\partial^2 C}{\partial y^2}\right] - \left[v_x \frac{\partial C}{\partial x} + v_y \frac{\partial C}{\partial y}\right] \tag{3.3}$$

To simulate the initial conditions, a matrix of chloride concentrations is created with high concentrations on the outside of the freeze wall and low concentrations on the mine pit side of the

freeze wall. An initial matrix of hydraulic head level is also created with a constant head level on the outside of the wall and a gradational head on the inside of the wall that drops to the base level of the mine pit. Matrices of constant hydraulic conductivities and dispersion coefficients are created for the model, and the wall is placed into the model by setting the hydraulic conductivity and dispersion coefficients to a very low value along the freeze wall. In the early stages of simulating the breach, the hydraulic conductivity and dispersion coefficients along the wall prevent contaminant transport across the wall. To initiate the breach, at the breach location along the wall, the hydraulic conductivity and dispersion coefficients are changed to match the surrounding cells. The parameters for the breach simulation are discussed in more detail in Section 4.1.1.

3.3 Convert TDS concentrations to resistivity

The goal of this monitoring setup is to detect the migration of saline (high TDS) water across the freeze wall to an area with non-saline (low TDS) water. The salinity of water is not something that can be directly mapped using geophysical techniques, but the salinity of water does have a predictable effect on the electrical conductivity of the water. Campanella and Weemees (1990) describe how the bulk electrical resistivity of the ground is a function of several properties including groundwater resistivity, pore-space geometry, and soil type. There are several methods that one can use to calculate the bulk electrical resistivity of soils. Two popular methods of estimating the bulk electrical resistivity of soils are Archie's equation (Archie, 1942) and Waxman-Smits equation (Waxman and Thomas, 1974). Archie's equation assumes that the soil is composed of sand and does not consider the effects of clays on the bulk electrical resistivity. The Waxman-Smits equation is a more complex equation that considers the effect of clays, but requires parameters

that are difficult to estimate. In this work, the basal aquifer is not expected to contain clay, which justifies the use of Archie's equation. Archie's equation is:

$$\rho_T = \frac{a\rho_w}{\phi^m S_w^n} \tag{3.4}$$

where ρ_T is the bulk resistivity,

ρ_w is the resistivity of the pore water,

ϕ is porosity,

S_w is water saturation,

m is the cementation exponent,

a is the tortuosity,

n is the saturation exponent.

The estimation of these parameters is not trivial and has been studied extensively (cf. Awolusi et al., 2005; Azar et al., 2008; Chen, H. and Fang, J., 2011; Hamada et al., 1995; Hamada, 2010; Maute et al., 1992). The parameters m, n, and ϕ are generally obtained from lab tests on core samples, ρ_w is roughly known from water samples taken, and at depths below the water table S_w is 1. In equation (3.4), the resistivity of the pore fluid is a function of TDS and temperature and can be estimated using Crain's method (Crain, 1974), which states:

$$\rho_w = (\frac{40000}{T * TDS})^{0.88} \tag{3.5}$$

where T is the water temperature in degrees Fahrenheit,

TDS is the total dissolved solids in parts per million,

ρ_w is the resistivity of the pore water in Ωm.

Figure 3.3.1 presents the calculated formation resistivities for a range of TDS and porosity values.

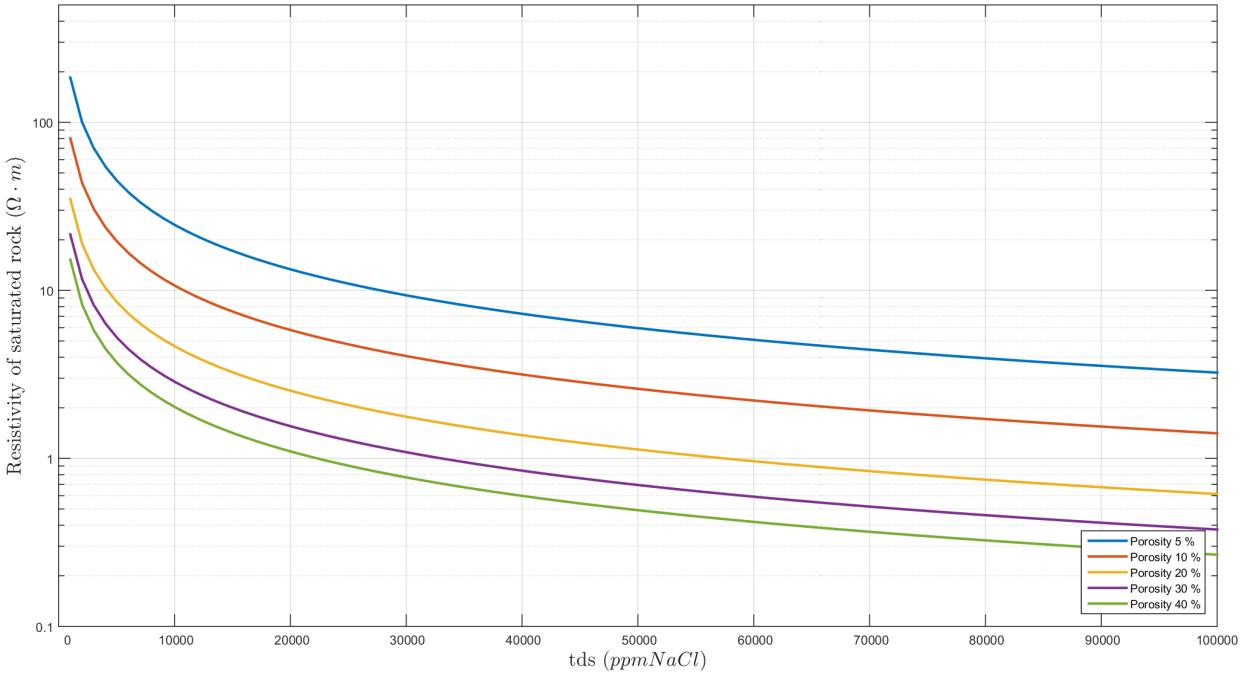

Figure 3.3.1: Formation resistivities for a range of total dissolved chloride values and formation porosities

Figure 3.3.1 shows that the relationship between TDS and bulk resistivity is not linear, and because of this the sensitivity of the conversion from TDS to bulk resistivity is different depending on TDS. At low TDS values, bulk resistivity is much more sensitive to changes in TDS than at higher TDS values, meaning that this method will be more effective if the changes in TDS that the method described herein is designed to detect are at the low end of the TDS range described in Figure 3.3.1.

3.4 Create synthetic data

The synthetic data were created using a finite volume approximation of Poisson's equation (2.5) in Cartesian coordinates. The discrete functions for gradient (∇) and divergence ($\nabla\cdot$) in Cartesian coordinates are:

$$\nabla f = \hat{x}\frac{\partial f}{\partial x} + \hat{y}\frac{\partial f}{\partial y} + \hat{z}\frac{\partial f}{\partial z} \tag{3.6}$$

$$\nabla \cdot \hat{f} = \frac{\partial (f_x)}{\partial x} + \frac{\partial (f_y)}{\partial y} + \frac{\partial (f_z)}{\partial z} \tag{3.7}$$

To numerically solve equation (2.5) for electrical potential ϕ, numerical gradient and divergence approximations are necessary. Following Pidlisecky and Knight (2008), once numerical finite difference operators have been created for gradient and divergence, equation (2.5) can be written in matrix notation as:

$$(\mathbf{DS}(\sigma)\mathbf{G})u = \mathbf{A}(\sigma)\hat{\phi} = q \tag{3.8}$$

where **D** is the divergence matrix,

$\mathbf{S}(\sigma)$ is the diagonal matrix containing the electrical conductivity values,

G is the gradient matrix,

$\hat{\phi}$ is a vector of electrical potentials,

$\mathbf{A}(\sigma)$ is the combined forward operator,

q is a vector containing the current pairs.

We solve equation (3.8), to yield the potential field:

$$\hat{\phi} = \mathbf{A}^{-1}(\sigma)q \tag{3.9}$$

The result from equation (3.9) is a vector of electrical potential values for the cells in the model.

On the basis of the survey potential electrode locations potential differences can be calculated across each measurement pair. These measurements are then multiplied by the geometric factor K to provide apparent resistivity ρ. Apparent resistivities are then calculated using the following:

$$\rho_{app} = \Delta\hat{\phi}K \tag{3.10}$$

where the geometric factor K is calculated by the following:

$$K = \frac{4\pi}{\frac{1}{r_{AM}} - \frac{1}{r_{AN}} - \frac{1}{r_{BM}} + \frac{1}{r_{BN}} + \frac{1}{r_{A'M}} - \frac{1}{r_{A'N}} - \frac{1}{r_{B'M}} + \frac{1}{r_{B'N}}} \tag{3.11}$$

where r_{AM} is the distance from current electrode A to potential electrode M.

Figure 3.4.1 presents an example of the suite of electrode locations used for a full survey. In Figure 3.4.1, the lines plotted represent the current locations below the top of the survey for each reading. This is an example of a dipole-dipole array for a series of 15 current-potential dipole spacings (n-spacings).

The potential close to the current electrode locations increases very rapidly as illustrated in Figure 3.4.2. This rapid increase in electrical potential approaching the current electrodes can cause significant discretization errors at cells close to the electrodes. There can also be discretization errors at layer boundaries, or wherever the electrical field is caused to curve rapidly. These discretization errors can be solved by refining the mesh, but at a computational cost. The increased computation time in a 3-D forward calculation using a highly refined mesh can render the method impractical for most users. A solution is to use adaptive mesh refinement, which is currently an area of research, to refine the mesh where it is needed and to leave it coarse where it is not. This method is beyond the scope of this thesis, but for future work it is a method that should be employed. The mesh for this thesis is refined near the borehole and coarse away from the borehole and mesh is uniform with depth; this mesh is presented in Figure 3.4.3.

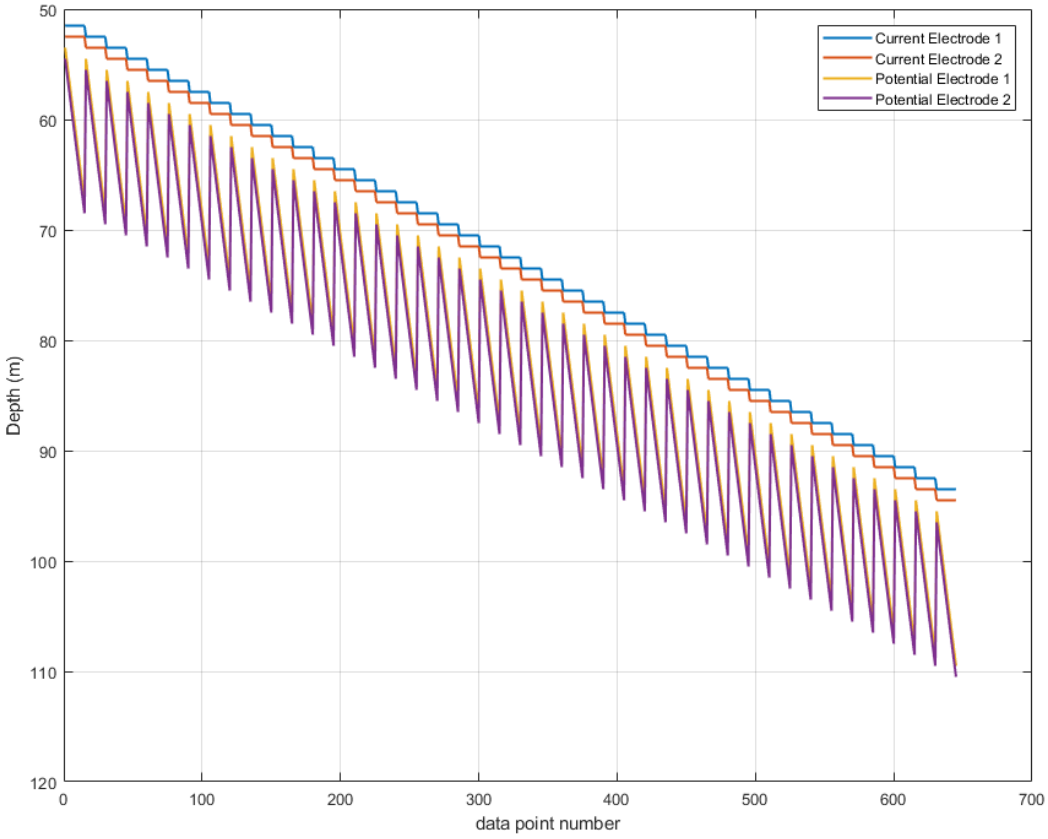

Figure 3.4.1: Survey sequence for test model. In this diagram, for each data point on the x-axis, the current injection electrode depths are indicated by the red and blue lines, and the electrical potential measurement locations are indicated by the yellow and purple lines. For each current injection location there are multiple measurement locations where the potential dipole length is the same as the current dipole length. This survey sequence is a typical dipole-dipole survey configuration.

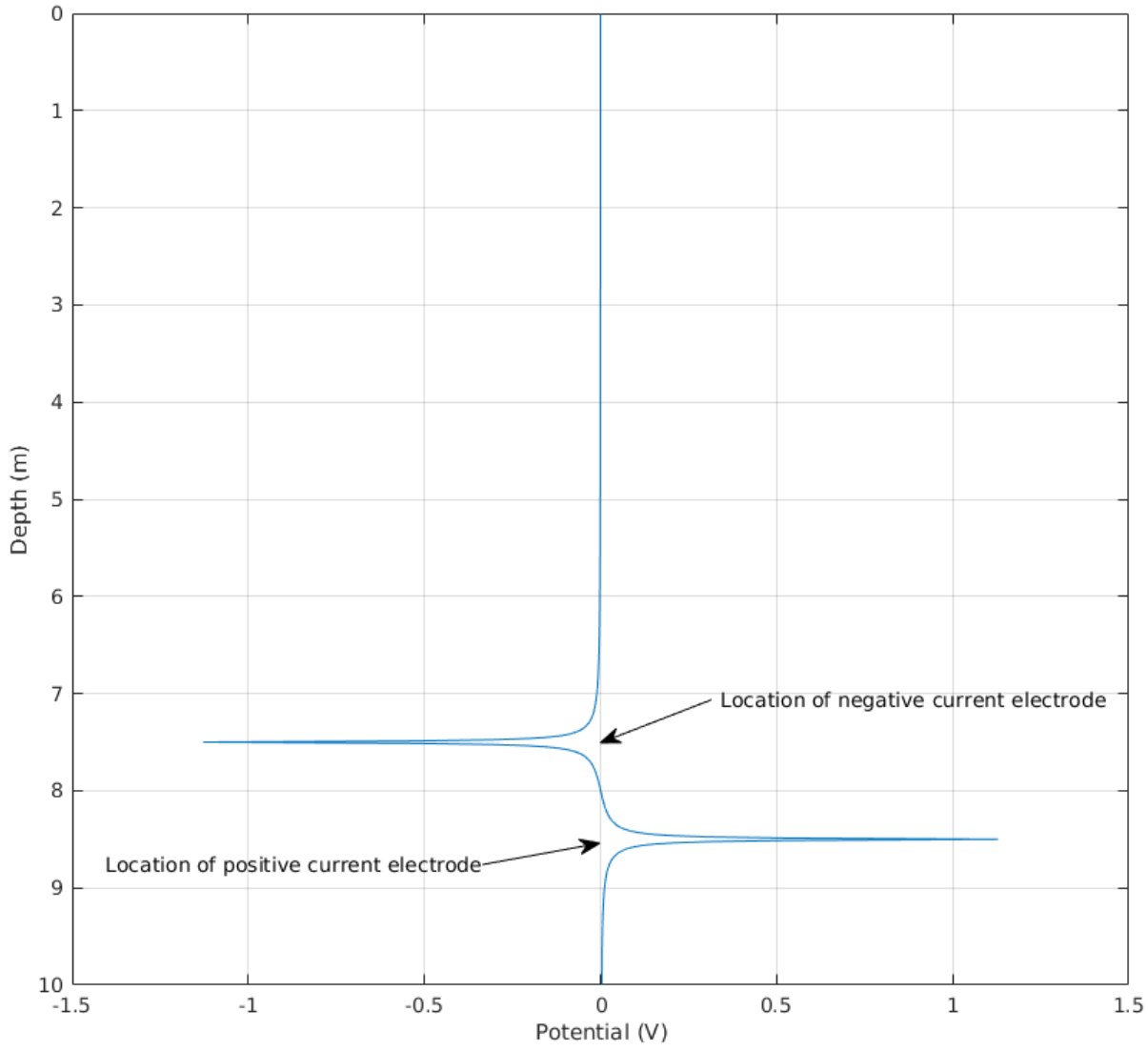

Figure 3.4.2: Illustration of the potential near a current electrode

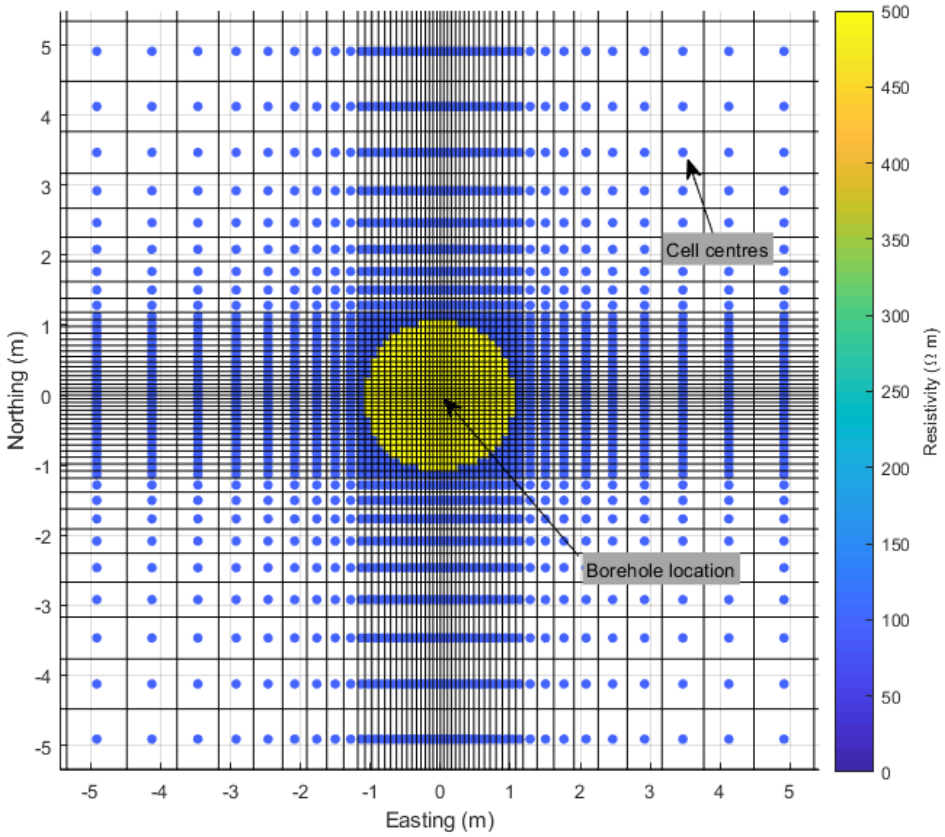

Figure 3.4.3: Illustration of the mesh used for the forward calculations in this thesis

3.5 Synthetic data analysis

The apparent resistivity data can be plotted in pseudosections, where the position of a data-point on the y-axis depends on the depth of the current-potential centre point, and the position of the data-point on the x-axis depends on the offset between the current-potential electrodes. Figure 3.5.1 presents a pseudosection schematic that shows where each apparent resistivity datapoint is plotted, where n-level represents the relative distance between the borehole and the location of the datapoint. In Figure 3.5.1, each apparent resistivity datapoint is coloured to match the colour of the potential dipole. Figure 3.5.2 presents an example of a pseudosection generated from a single-borehole in a layered model.

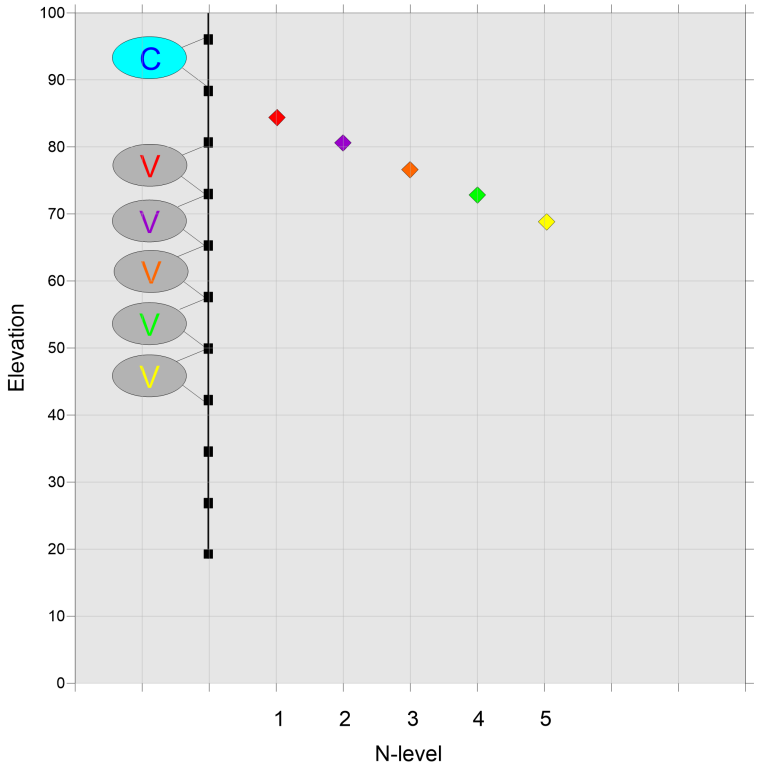

Figure 3.5.1: Illustration of a borehole ERT pseudosection schematic. This illustration shows where apparent resistivities are plotted for one current dipole and 5 potential dipoles. A full pseudosection would include points from a series of current electrodes and potential electrodes.

The pseudosections by themselves are useful in identifying where the stratigraphic boundaries

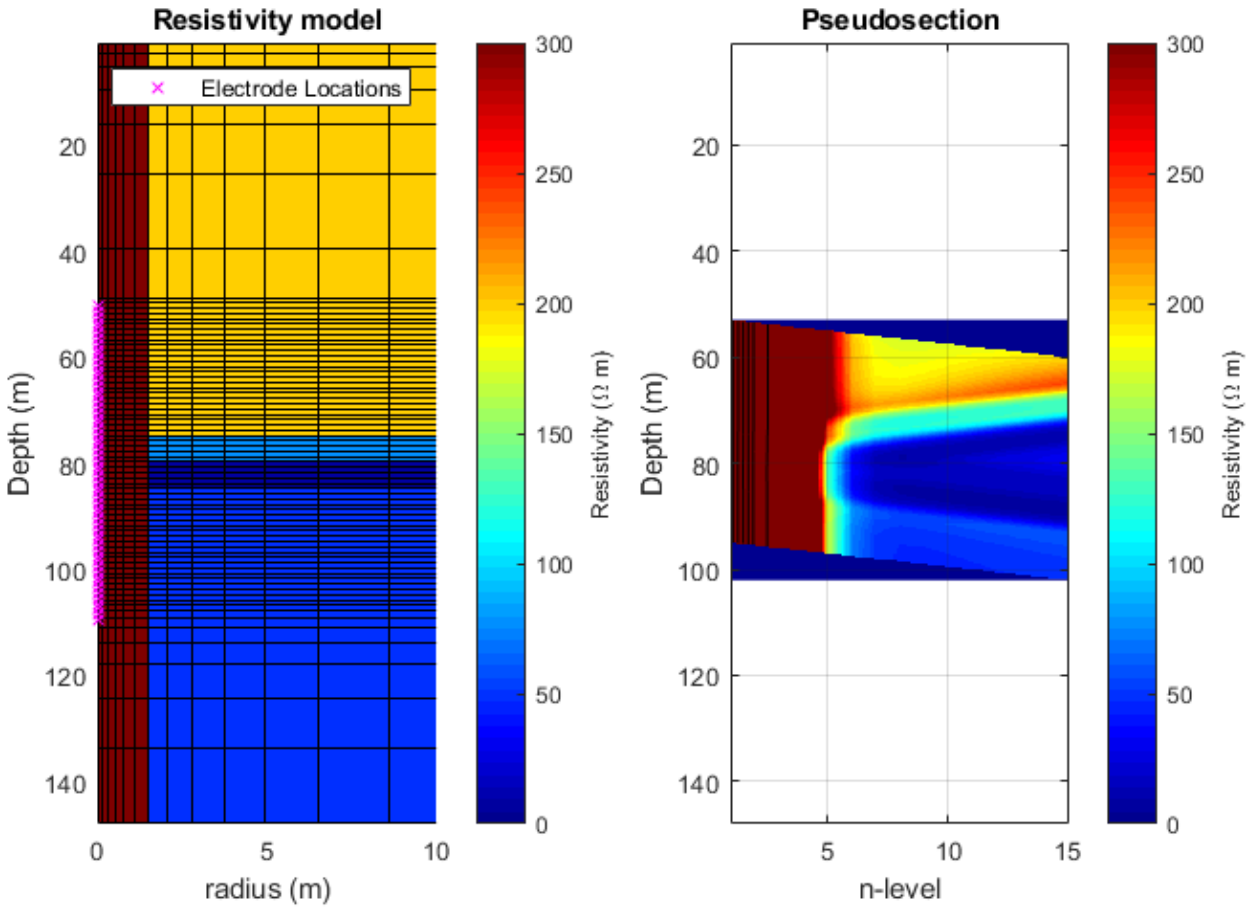

Figure 3.5.2: Illustration of a sample pseudosection for a layered model

are, but over time, the pseudosection differences can be a very powerful diagnostic tool. To illustrate the effect of a change in resistivity surrounding a borehole on the pseudosection, data were simulated over the two models illustrated in Figure 3.5.3. The two models illustrated in Figure 3.5.3 are different in the layer between 70 and 75 m depth and differ by 10 Ωm. The two pseudosection plots and the difference plot are presented in Figure 3.5.4.

In Figure 3.5.4, the difference in the pseudosections between the models is significant and coherent, which indicates that it should be possible to identify a change surrounding a borehole on the basis of the pseudosections alone. For a situation such as the one presented in this thesis, where there are a number of boreholes along the wall, it should be possible to determine the location of

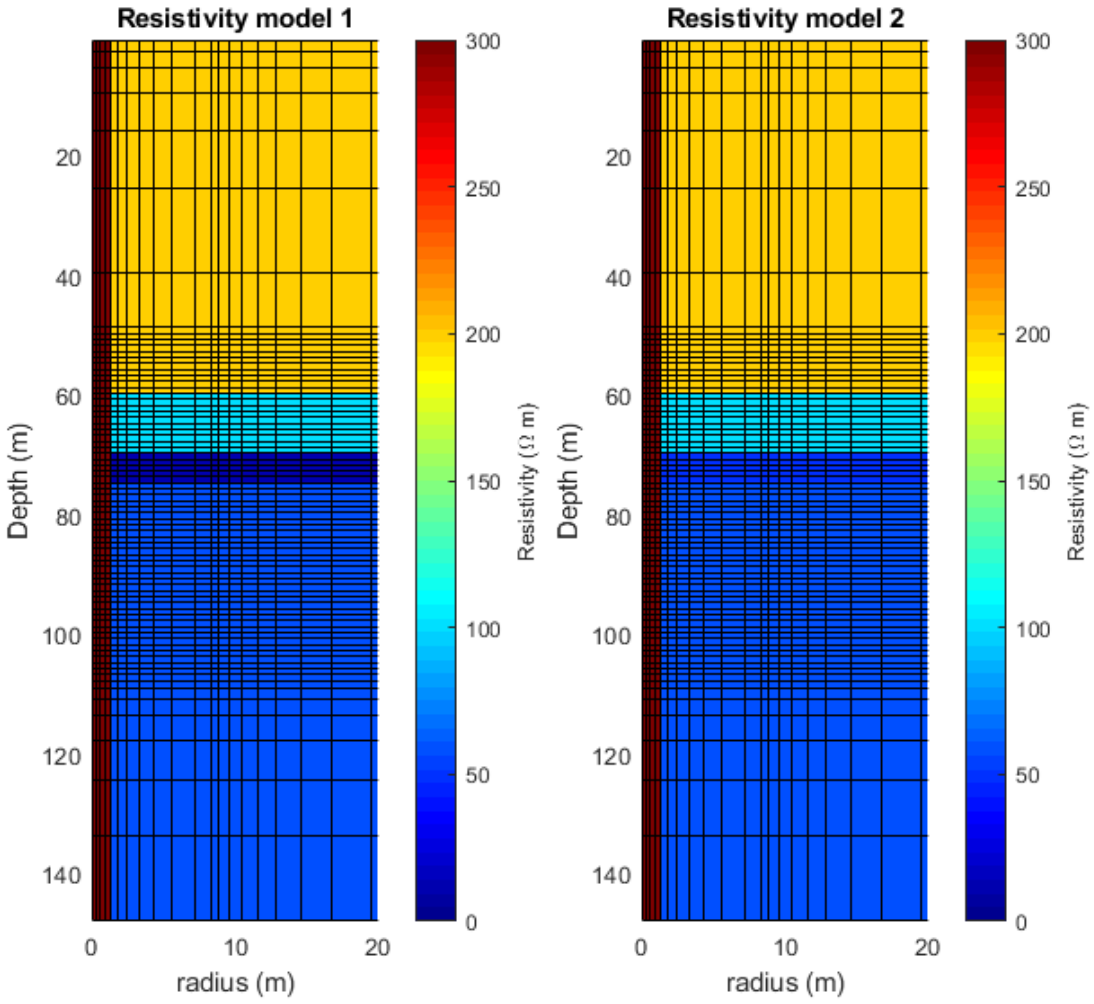

Figure 3.5.3: Two models for which data were simulated to illustrate pseudosection difference plot. The models differ in the zone centred on 72 m depth.

a change in resistivity using the apparent resistivity pseudosections from several boreholes along the length of the freeze wall. To illustrate the effect of a small change of resistivity in a layer of the model a slice is taken out of the pseudosection 1 from Figure 3.5.4 at a depth of 72 m and is presented in Figure 3.5.5. For models where the formation resistivity at 72 m depth changes by 10 to 50 Ωm, the relative differences to the slice presented in Figure 3.5.5 are presented in Figure 3.5.6.

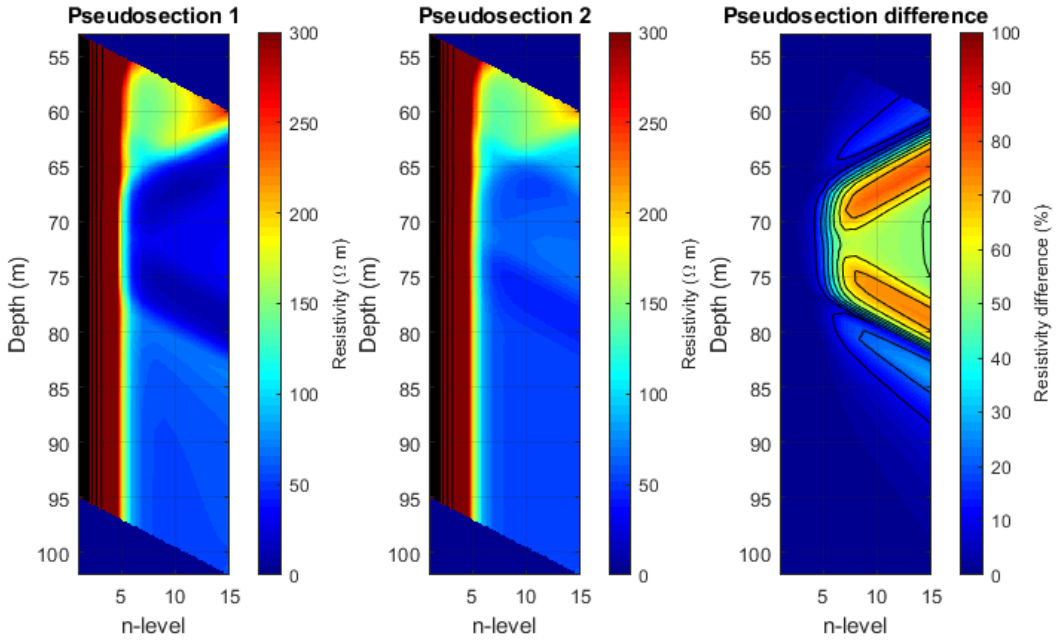

Figure 3.5.4: Sample pseudosections and difference plot for models in Figure 3.5.3

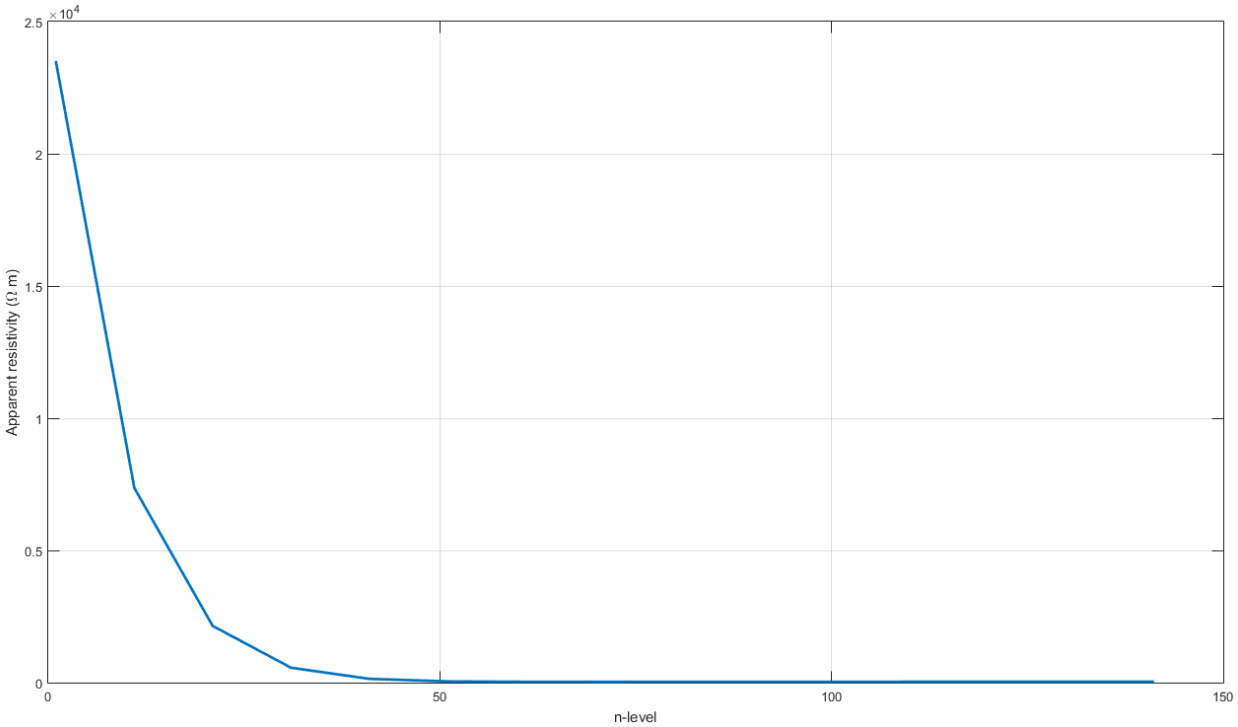

Figure 3.5.5: Pseudosection slice at 72 m depth for Figure 3.5.4

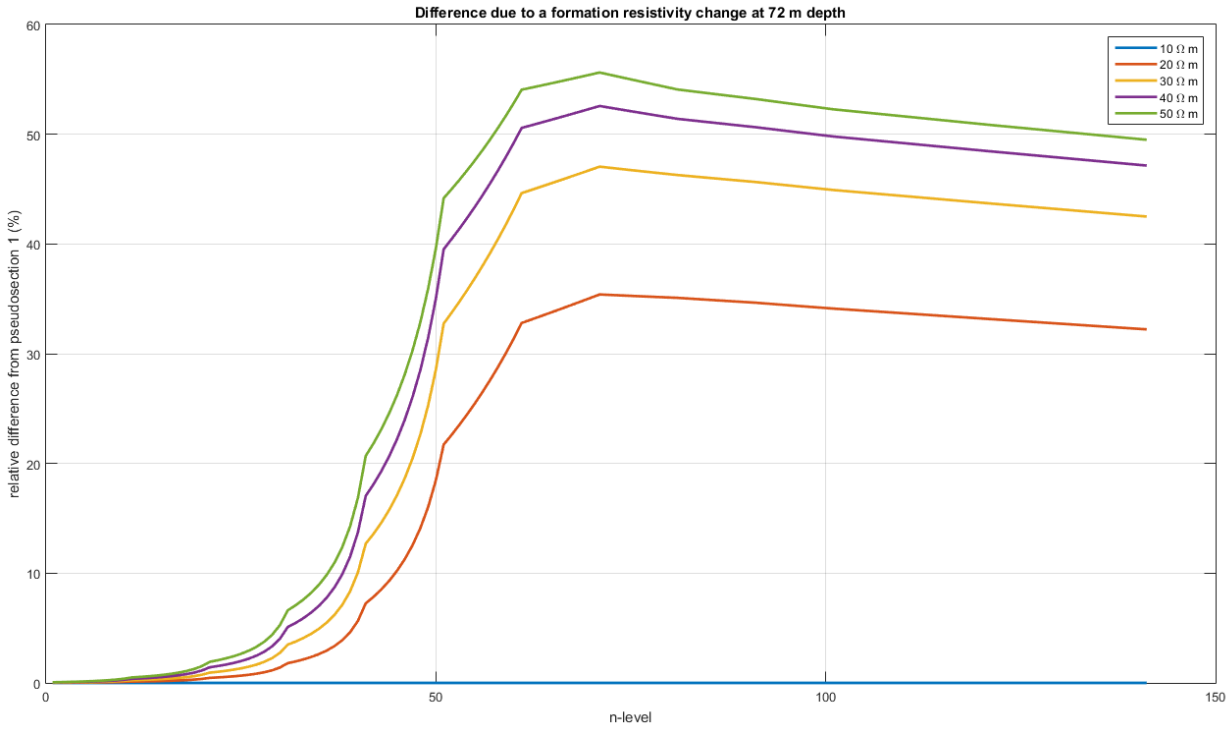

Figure 3.5.6: Pseudosection slice differences for formation resistivity changes at 72 m depth

3.6 Inversion

To invert the experimental data, the present work uses a simplified inversion approach where each borehole is inverted using a cylindrical discretization with no azimuthal variation in resistivities, which is similar to the method presented by Pidlisecky et al. (2013). This approach reflects the fact that there is no azimuthal information available from a single borehole ERT array. The main benefit of the approach is reduced computation time; each forward calculation using the 3-D Cartesian discretization can take tens of minutes to hours, and a forward calculation using a simplified cylindrical discretization can take a few seconds. These run time differences can be very significant during the inversion process to the point where a 3-D inversion approach would be impractical for real-time monitoring. The cylindrical parameterization and the inversion are described further in the following subsections.

3.6.1 Cylindrical parameterization

In this approach to estimating the thickness of the freeze wall and to estimating the resistivity of the surrounding material it is useful to use the following parameters: radius of the frozen section surrounding the borehole, the resistivity of the frozen section surrounding the borehole, and the resistivity of the unfrozen formation. Figure 3.6.1 presents a schematic illustrating the conceptual model surrounding the borehole. In Figure 3.6.1, the electrode array is pictured as being centred in a portion of the frozen wall. The distance from the electrode array out to the width of the frozen wall is considered in this thesis to be the wall radius (r_i), the electrical resistivity of the area within the wall radius is considered to be the wall resistivity (ρ_i), and the electrical resistivity of the material beyond the wall radius is considered to be the formation resistivity (ρ_f).

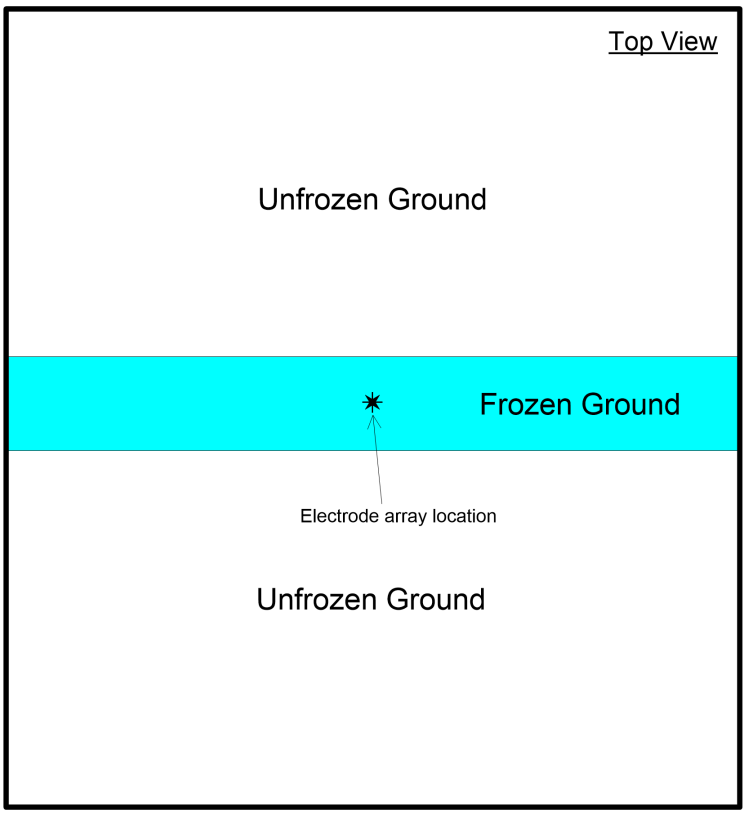

Figure 3.6.1: Illustration of the conceptual schematic surrounding the borehole

The simplified cylindrical parameterization is illustrated in Figure 3.6.2. In Figure 3.6.2, the model is simplified to two shells: the inner shell, and the outer shell. This leaves three parameters for each layer in the model: the inner radius, the inner resistivity, and the outer resistivity.

In Figure 3.6.2, the outer shell ρ_f does not correspond to a shell that has a uniform electrical resistivity; frozen ground can have resistivities several orders of magnitude higher than that of unfrozen ground, and saline pore-fluid on one side of the wall can cause the resistivity to be an order of magnitude lower than the resistivity of ground with non-saline pore-fluid. The resistivity of frozen ground can be described by the following equation (McGinnis et al., 1973):

$$\rho = \rho_0 e^{b(T_f - T)} \tag{3.12}$$

where ρ_0 is the resistivity of the unfrozen ground,

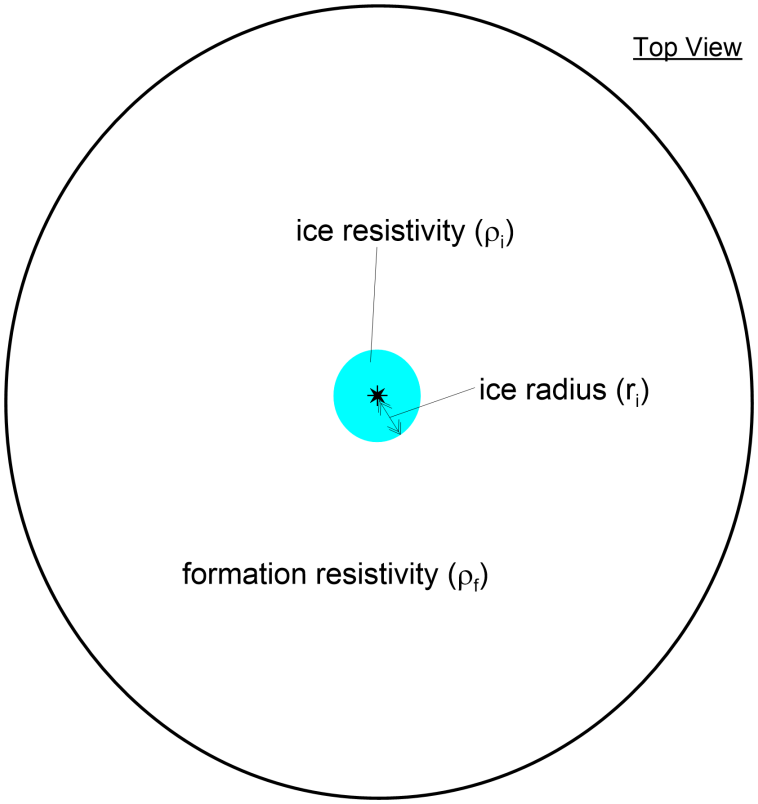

Figure 3.6.2: Illustration of the simplified cylindrical parameterization. The simplified model has been reduced to three parameters: ρ_i, r_i, and ρ_f.

b is a curve fitting coefficient,

T_f is the freezing temperature of the pore water,

T is the ground temperature.

Figure 3.6.3 presents a plot of resistivities for the basal McMurray Formation using $\rho_0 = 150\Omega \cdot m$. The curve presented in Figure 3.6.3 was plotted using a b coefficient of 0.3. The electrical resistivity of the soil increases rapidly as the temperature decreases due to the high resistivity of ice compared to water.

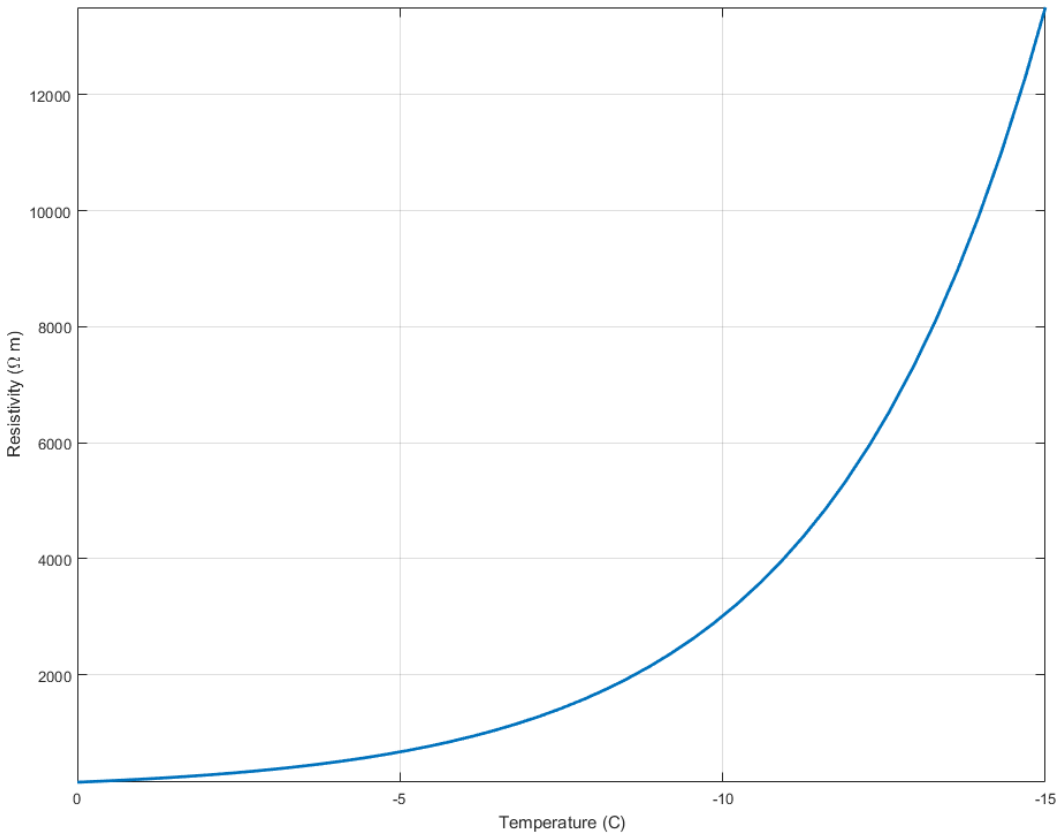

Figure 3.6.3: Illustration of how resistivity changes with temperature below the freezing point for soils with an unfrozen resistivity of 150 (Ωm)

3.6.2 Cylindrical forward operator comparison with Cartesian

The cylindrical forward operator for this thesis differs from the Cartesian forward operator in how it solves Poisson's equation (2.5). In the cylindrical case, the functions for gradient (∇) and divergence ($\nabla\cdot$) are:

$$\nabla f = \hat{r}\frac{\partial f}{\partial r} + \frac{1}{r}\hat{\theta}\frac{\partial f}{\partial \theta} + \hat{z}\frac{\partial f}{\partial z} \tag{3.13}$$

$$\nabla \cdot \hat{f} = \frac{1}{r}\frac{\partial (r f_r)}{\partial r} + \frac{1}{r}\frac{\partial (f_\theta)}{\partial \theta} + \frac{\partial (f_z)}{\partial z} \tag{3.14}$$

where r is the radial distance,

θ is the azimuth angle (in radians),

z is the depth.

The present work assumes no changes with respect to azimuthal angle θ, since the survey data does not allow resolution in this direction which reduces equations (3.13) and (3.14) to:

$$\nabla f = \hat{r}\frac{\partial f}{\partial r} + \hat{z}\frac{\partial f}{\partial z} \tag{3.15}$$

$$\nabla \cdot f = \frac{1}{r}\frac{\partial (r f_r)}{\partial r} + \frac{\partial (f_z)}{\partial z} \tag{3.16}$$

To illustrate that these forward formulations are similar, forward calculations were run on the same model, discretized in the two coordinate systems (i.e. 3-D Cartesian and cylindrical) and compared. The model is a cylinder with a uniform electrical resistivity inside a homogeneous whole space. Figures 3.6.4 and 3.6.5 present the discretizations of this model in Cartesian and cylindrical coordinates, respectively.

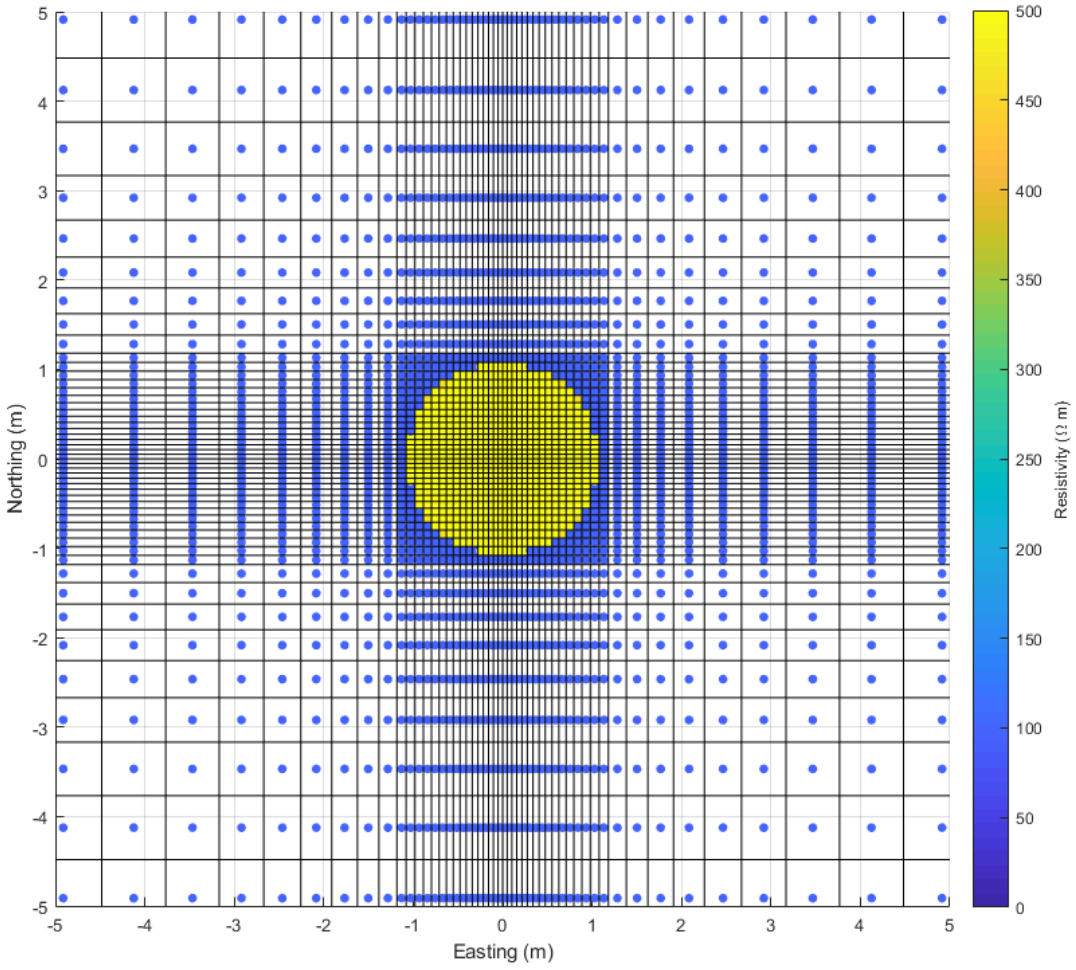

Figure 3.6.4: Illustration of the cartesian mesh. Dots represent cell centres, and the colors represent resistivity

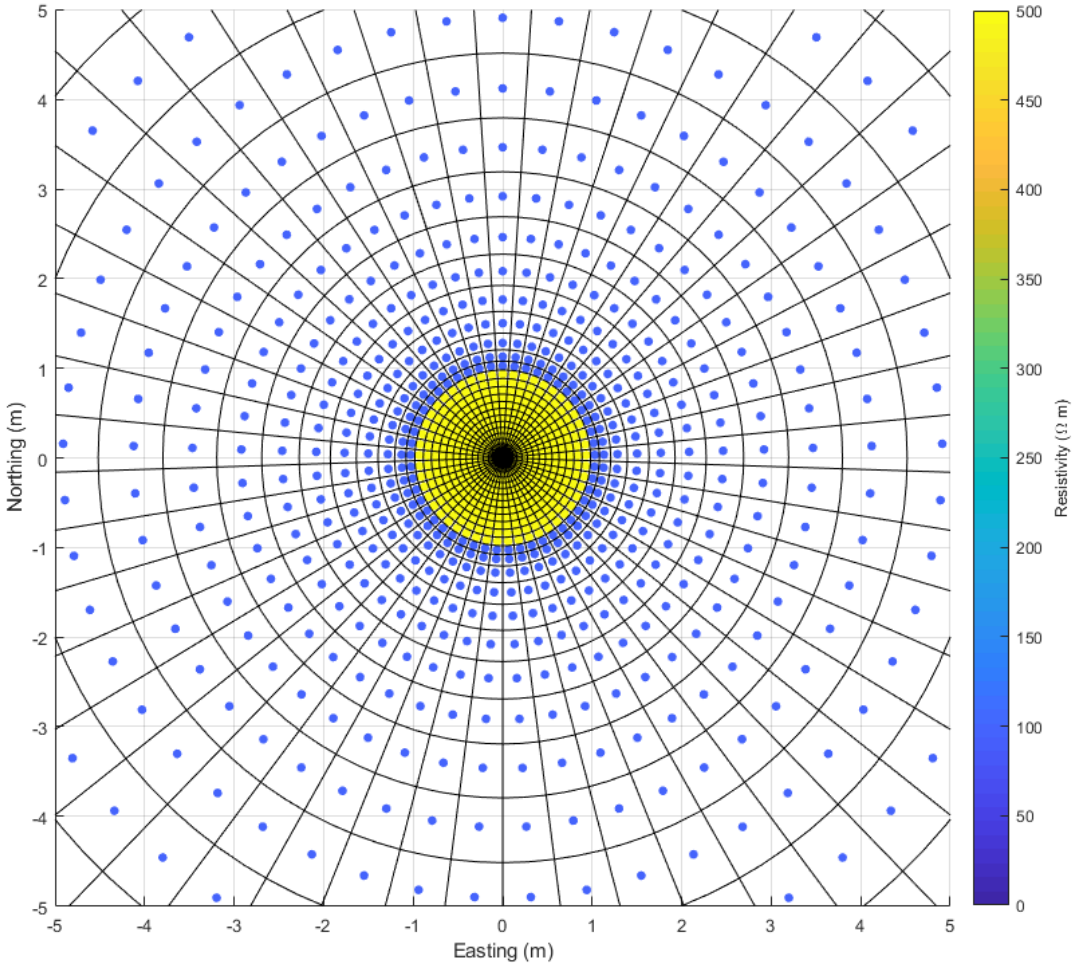

Figure 3.6.5: Illustration of the cylindrical mesh. Dots represent cell centres and the colors represent resistivity

In Figures 3.6.4 and 3.6.5, it is expected that there will be errors due to the approximation of a cylinder in Cartesian space, and that those errors will decrease as the mesh is refined.

Figure 3.6.6 presents the forward calculated apparent resistivities for one current dipole in the middle of the cylinder and 15 n-spacings for the two forward operators.

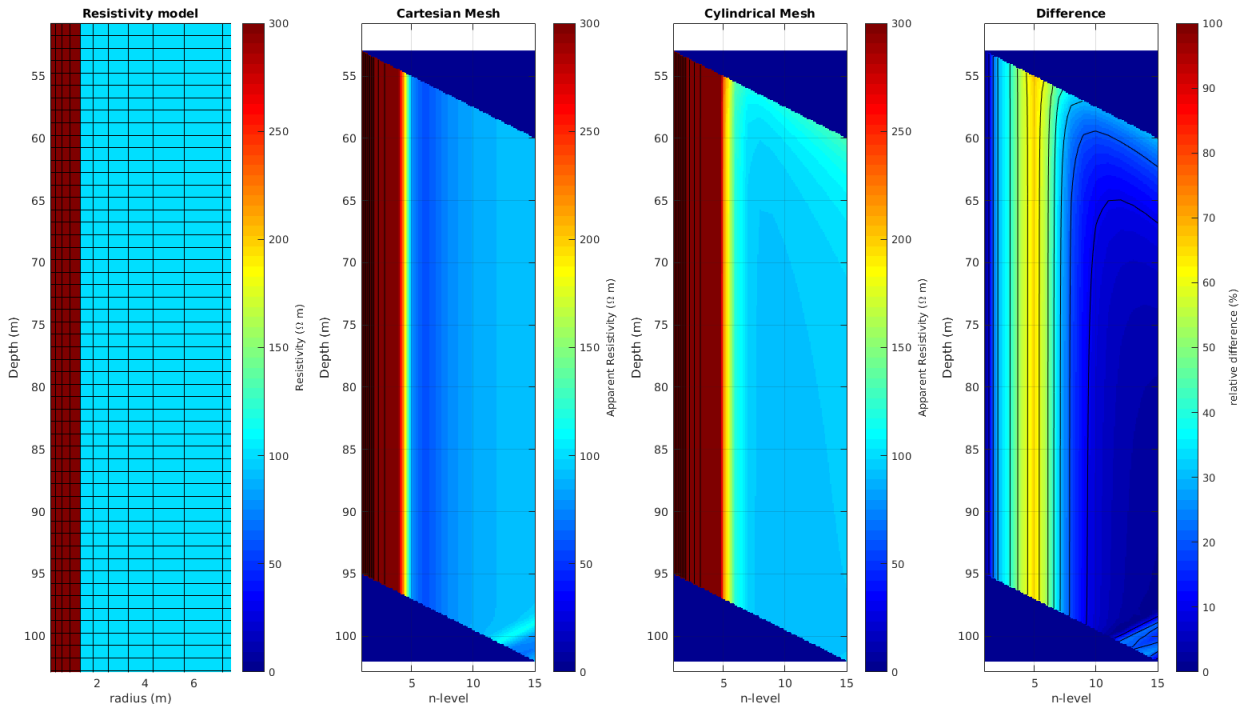

Figure 3.6.6: Comparison of the apparent resistivities for the cylindrical model using the cylindrical forward operator and the Cartesian forward operator. There are significant differences immediately adjacent to the high-resistivity portion of the model near the borehole.

In Figure 3.6.6, there is significant difference between the pesudosections using the Cartesian and cylindrical meshes. The difference at an n-level of 5 can exceed 50%. This error results from two factors, both associated with the approximation of the cylindrical geometry in the Cartesian mesh: the discretization of the cylindrical geometry is coarse and there is azimuthal variation in the discretization. Figures 3.6.7 and 3.6.8 present the azimuthal variation in discretization for the cylindrical mesh and the Cartesian mesh, respectively. In Figures 3.6.7 and 3.6.8, the discretization is highly variable with azimuth in the Cartesian case and consistent in the cylindrical case. In addition to variations in azimuth, the cell volumes are different between the two meshes. Figure 3.6.9 presents an illustration of the Cartesian and cylindrical meshes and shows how cells with

similar locations can have different volumes. These two meshes will require very fine discretization in order for the discretization error difference to be reduced to an acceptable level. This is only the case for this simulation, as field-collected data will not have discretization error. To completely test the cylindrical forward operator, a physical model or field-collected data should be used.

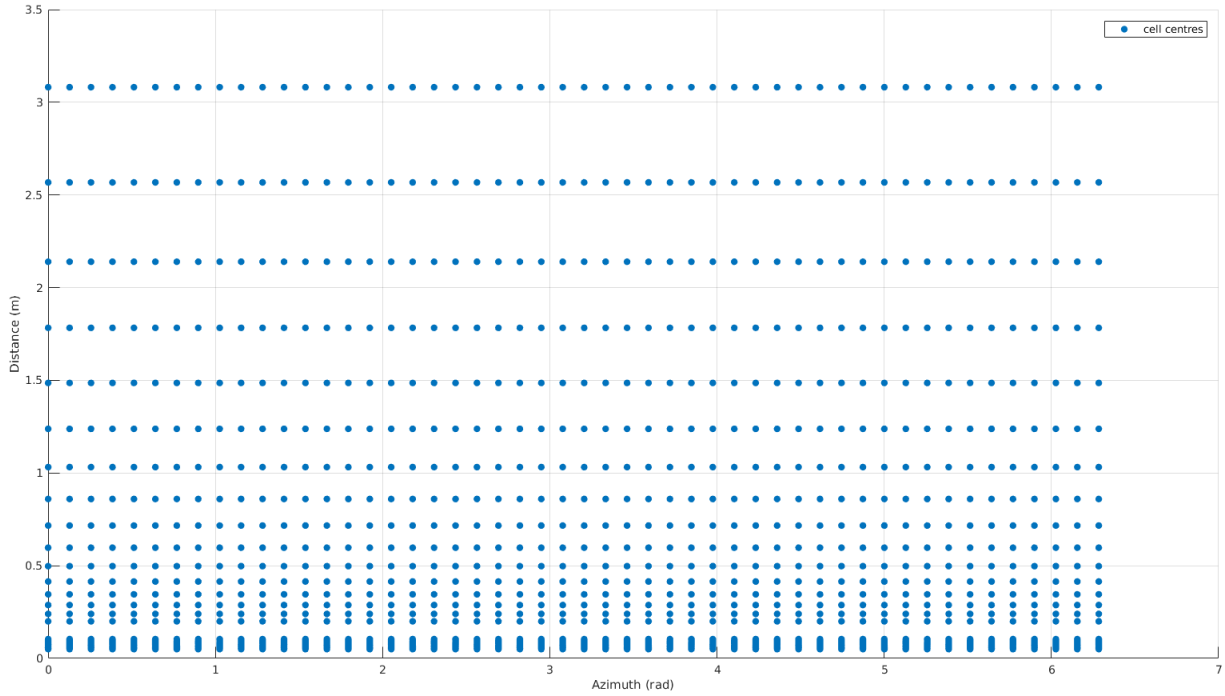

Figure 3.6.7: Plot of the discretization with azimuth for the cylindrical mesh.

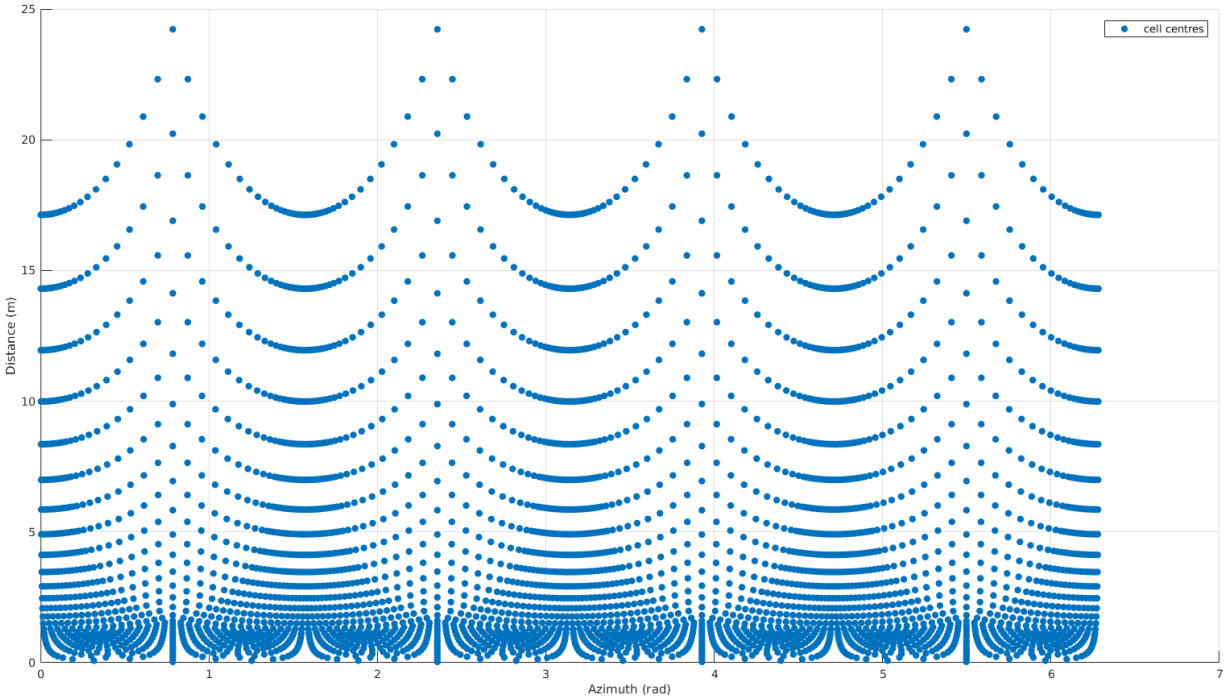

Figure 3.6.8: Plot of the discretization with azimuth for the Cartesian mesh.

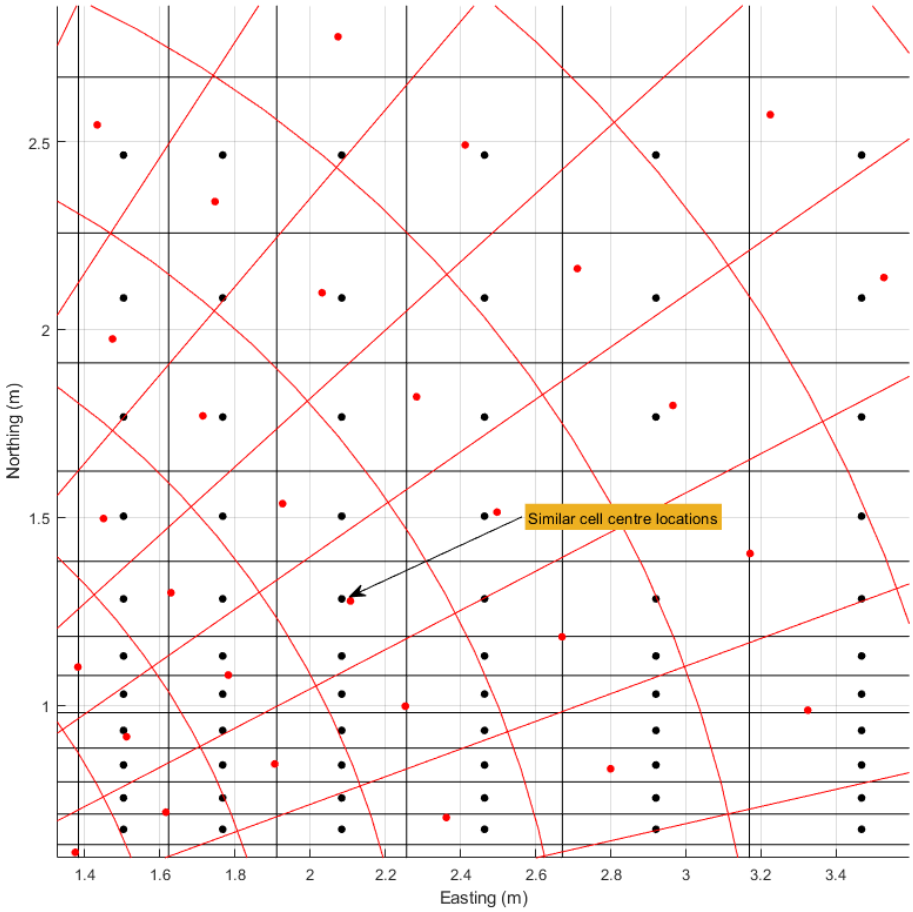

Figure 3.6.9: Comparison between the Cartesian (black) and cylindrical (red) meshes. For the indicated approximately co-located cell centre, there is a significant difference in the cell volume for the two meshes.

3.6.3 Inversion algorithm

The inversion algorithm used in this thesis is a gradient descent method that is modified to solve for three parameters (wall thickness r_i, wall resistivity ρ_i, and formation resistivity ρ_f). Inversion algorithms, in general, attempt to predict a set of model parameters that minimizes an objective function:

$$min\ \phi(\hat{m}) \tag{3.17}$$

where $\phi(\hat{m})$ is the objective function $\|\hat{d}_{obs} - f(\hat{m})\|_2$,

$\hat{d}_{obs}$ is the measured data,

$f(\hat{m})$ is the forward modelled data,

$\hat{m}$ is the set of model parameters $(\hat{\rho}_f, \hat{\rho}_i, \hat{r}_i)$.

This can be visualized in 2-parameter space as the minimum point in a 2-D dish (Figure 3.6.10). In Figure 3.6.10, the location of the true solution is identified and it is at the point where the misfit is minimized (in this case, zero). The minimum is found by taking the derivative of the misfit with respect to each of the estimated model parameters, setting it to zero, and using a root finding algorithm to find the model that corresponds to zero slope on the misfit function.

$$\frac{\partial(\phi(\hat{m}))}{\partial \hat{m}} = 0 \tag{3.18}$$

In equation (3.18), the objective function can also be written as:

$$\phi(\hat{m}) = \hat{\varepsilon}^T \hat{\varepsilon} \tag{3.19}$$

where $\hat{\varepsilon}$ is the misfit $\hat{d}_{obs} - f(\hat{m})$

Combining equations (3.18) and (3.19) gives:

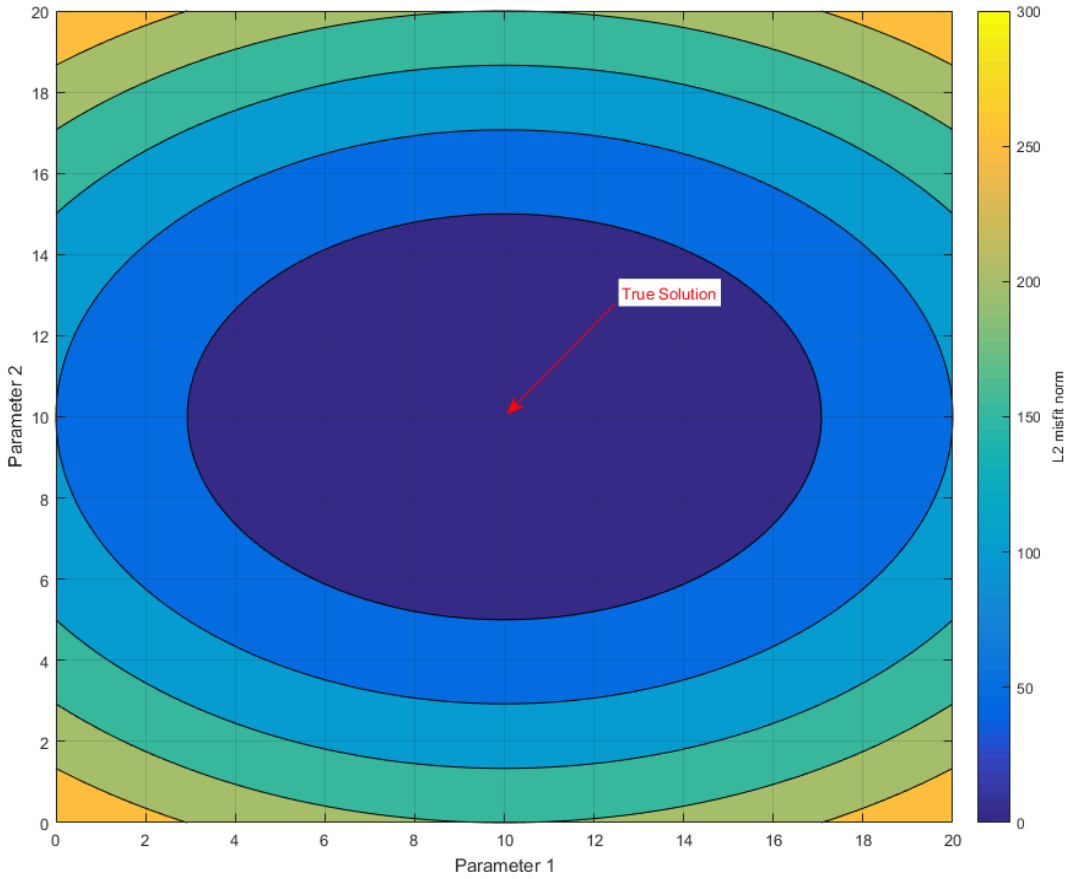

Figure 3.6.10: An illustration of misfit space with the location of the true model solution identified

$$\frac{\partial}{\partial \hat{m}}((\hat{d}_{obs} - f(\hat{m}))^T(\hat{d}_{obs} - f(\hat{m}))) = 0 \tag{3.20}$$

which reduces to:

$$\left(\frac{\partial f(\hat{m})}{\partial \hat{m}}\right)^T(\hat{d}_{obs} - f(\hat{m})) = 0 \tag{3.21}$$

In equation (3.21) $f(\hat{m})$ is unknown at the correct solution and can be approximated using a first order Taylor series:

$$\left(\frac{\partial f(\hat{m})}{\partial \hat{m}}\right)^T (\hat{d}_{obs} - f(\hat{m}_k) - \frac{\partial f(\hat{m})}{\partial \hat{m}} \Delta\hat{m}) = 0 \tag{3.22}$$

In equation (3.22) the partial derivative $\frac{\partial f(\hat{m})}{\partial \hat{m}}$ is the Jacobian matrix J and the difference $\hat{d}_{obs} - f(\hat{m}_k)$ has been defined as $\hat{\varepsilon}$ which can be used to rewrite equation (3.22) as:

$$J^T(\hat{\varepsilon} - J\Delta\hat{m}) = 0 \tag{3.23}$$

and re-arranged as:

$$\Delta\hat{m} = (J^T J)^{-1} J^T \hat{\varepsilon} \tag{3.24}$$

An iterative update of the model parameters of the form:

$$\hat{m}_{k+1} = \hat{m}_k - \Delta\hat{m} \tag{3.25}$$

Is combined with equation (3.24) to give the iterative parameter update equation:

$$\hat{m}_{k+1} = \hat{m}_k - (J^T J)^{-1} J^T \hat{\varepsilon} \tag{3.26}$$

To avoid overshooting the correct solution, a relaxation factor γ is applied to equation (3.26) to form:

$$\hat{m}_{k+1} = \hat{m}_k - \gamma(J^T J)^{-1} J^T \hat{\varepsilon} \tag{3.27}$$

For this inversion algorithm, the parameters being solved for are the radius of the freeze wall r_i, the log of the resistivity of the freeze wall ρ_i, and the log of the formation resistivity ρ_f (illustrated in Figure 3.6.11). The log of the resistivity parameters were used to force the resulting resistivity to be positive. In Figure 3.6.11, there are a total of 12 parameters. The apparent resistivities calculated

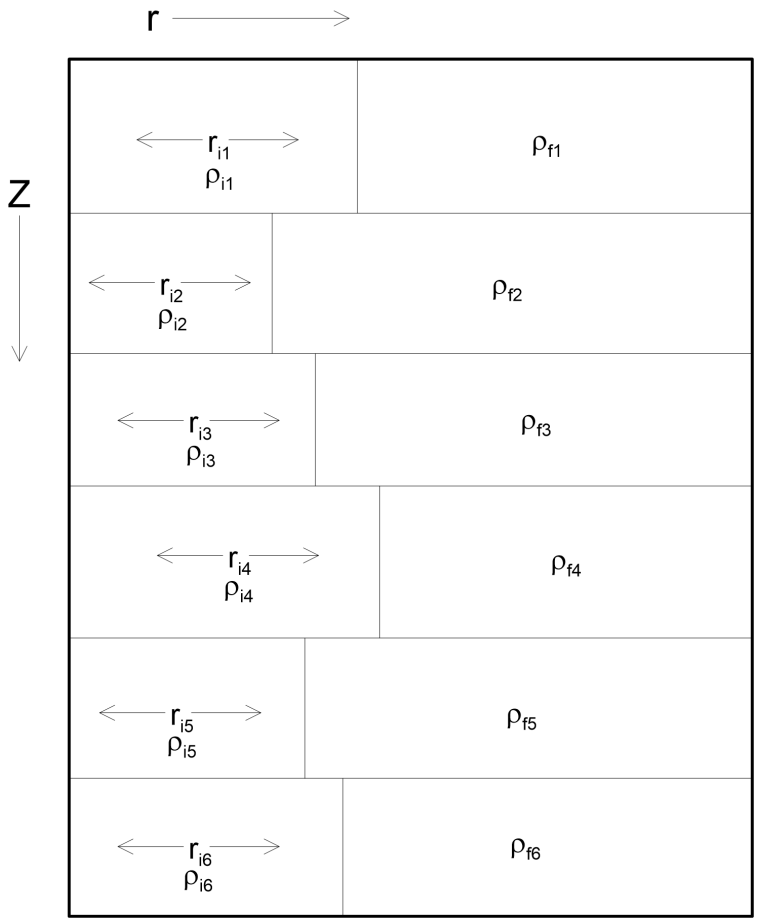

Figure 3.6.11: An illustration of the parametrization for this inversion scheme. There are three parameters for each layer: r_i, ρ_i, and ρ_f.

based on these parameters will have different sensitivities to the radius and the formation resistivity values. To solve the inversion problem using this parameterization, it is important to understand what the shape of the misfit space is, so that the algorithm can be designed appropriately.

To illustrate the misfit space, there were two experiments run: the first experiment is a two parameter test using r_i and ρ_f and assuming that ρ_i is correct; and the second experiment is a three parameter test using r_i, ρ_i, and ρ_f.

In the first experiment, two sets of misfit data were calculated using a range of r_i and ρ_f values for 1 layer: the first data-series assumed that all other parameters are correct (Figure 3.6.12); and the second data-series assumed significant errors in all other parameters (Figure 3.6.13).

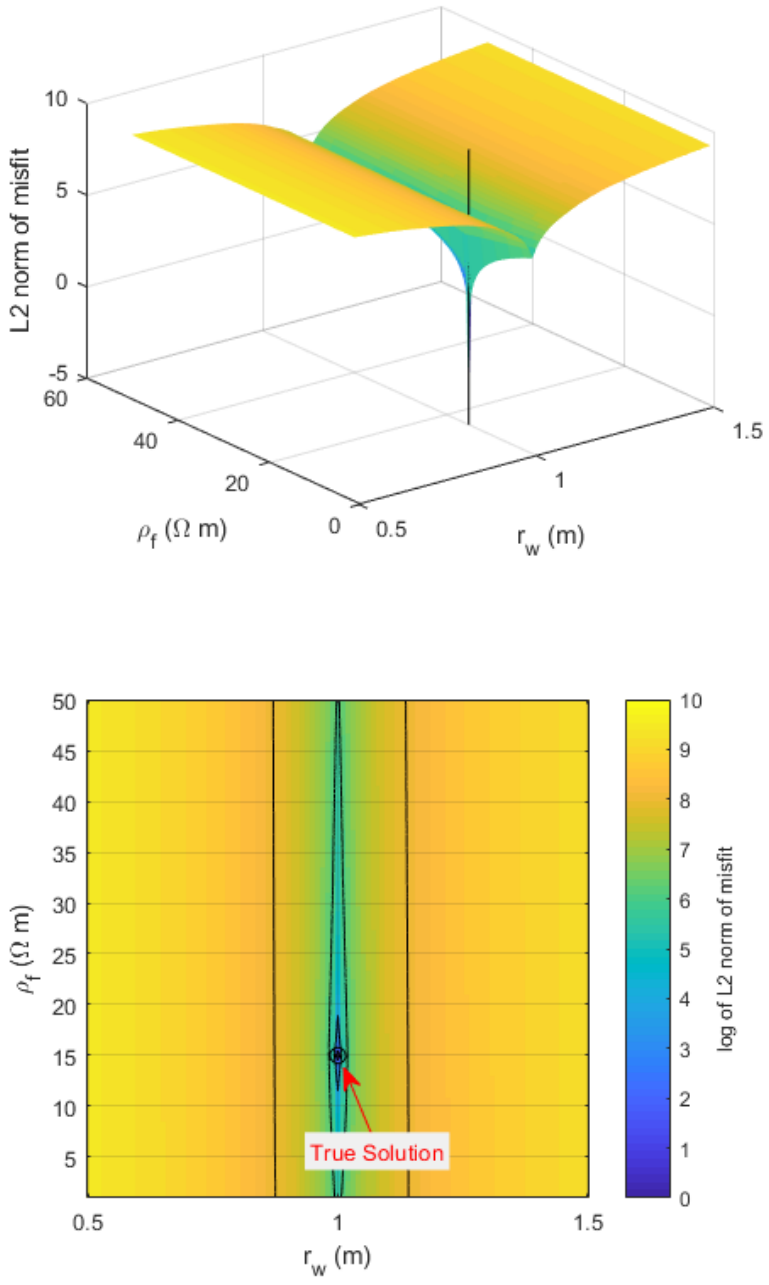

Figure 3.6.12: An illustration of the misfit space for this parameterization for 1 depth level (2 parameters), assuming all other layers are correct. The true solution is marked as a black stick.

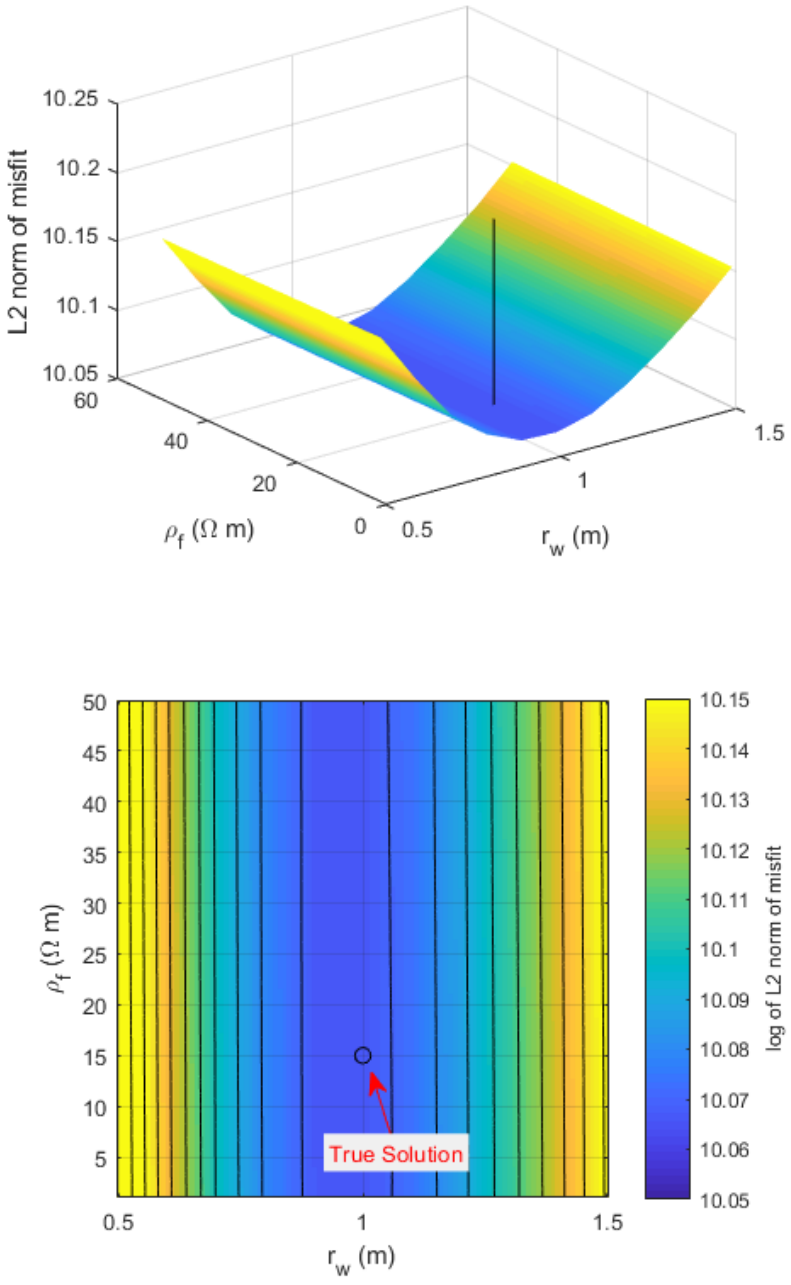

Figure 3.6.13: An illustration of the misfit space for this parameterization for 1 depth level (2 parameters), assuming significant error in the surrounding layers. The true solution is marked as a black stick.

In Figures 3.6.12 and 3.6.13, shapes of the misfit surfaces indicate that the modelled apparent resistivities are more sensitive to changes in r_i than to changes in ρ_f within the reasonable ranges of these two parameters; the model is not sensitive to ρ_f at all until r_i is correct. This is clearly illustrated in Figure 3.6.12, where the minimum in the ρ_f axis is only unique at the correct r_i value.

In the second experiment, two sets of misfit data were calculated using a range of r_i, ρ_i, and ρ_f values for 1 layer: the first data-series assumed that all other parameters are correct (Figure 3.6.14); and the second data-series assumed significant errors in all other parameters (Figure 3.6.15).

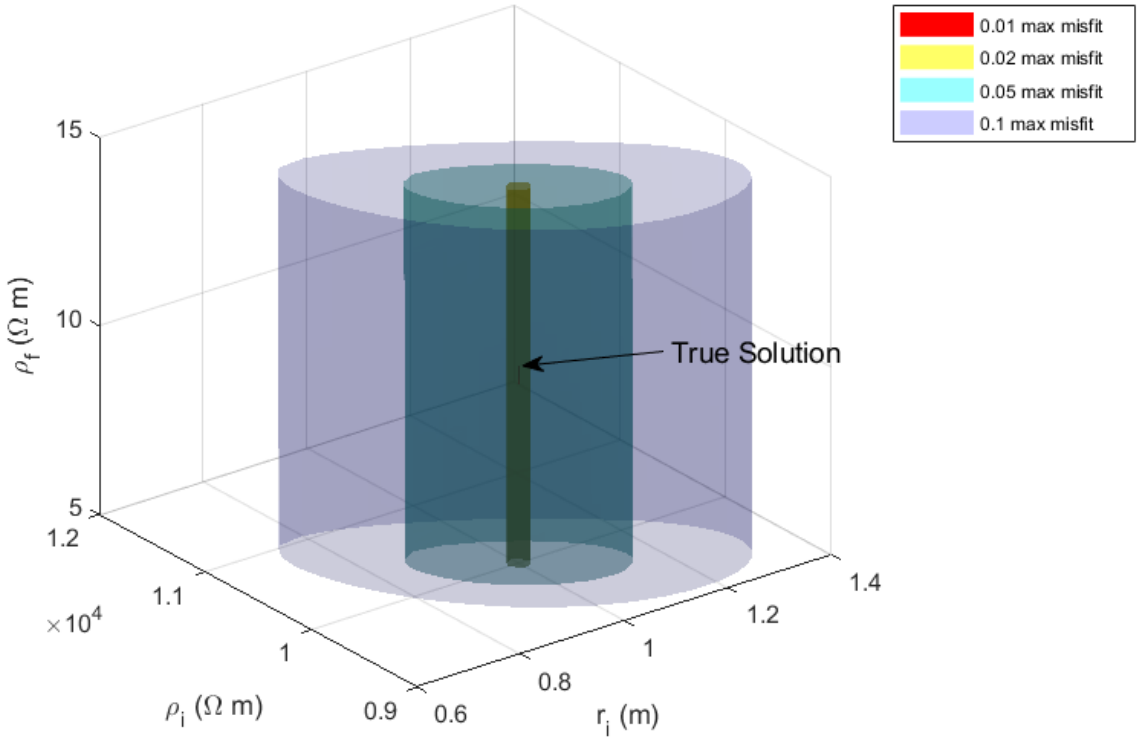

Figure 3.6.14: An illustration of the misfit space for this parameterization for 1 depth level (3 parameters), assuming all other layers are correct. The correct solution is within the red section in the middle of the space, which is slightly elongated in the z-direction and indicates that the solution is less sensitive to the z parameter (ρ_f) than to the x and y parameters (ρ_i and r_i), but the solution is still clear.

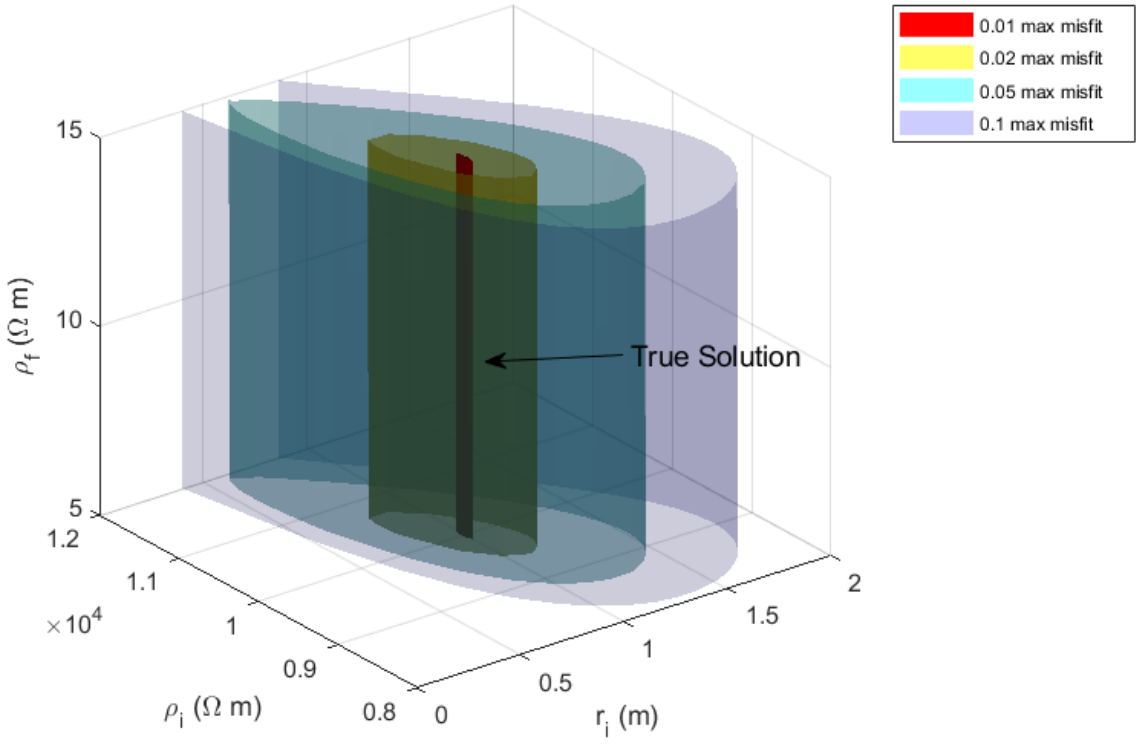

Figure 3.6.15: An illustration of the misfit space for this parameterization for 1 depth level (3 parameters), assuming significant error in the surrounding layers. The correct solution is within the red section in the middle of the space, which is greatly elongated in the z-direction and indicates that the solution is less sensitive to the z parameter (ρ_f) than to the x and y parameters (ρ_i and r_i), and the solution is not clear.

In Figures 3.6.14 and 3.6.15, the images show little change in the vertical direction, which indicates that the apparent resistivity misfit is not as sensitive to ρ_f, within a reasonable range, as it is to r_i and ρ_i. This result is similar to the conclusion from the 2-parameter tests in Figures 3.6.12 and 3.6.13. In Figure 3.6.14, the misfit is only sensitive to ρ_f once r_i and ρ_i are correct.

On the basis of the misfit surfaces presented in Figures 3.6.12 to 3.6.15, the inversion algorithm

used in this thesis solves sequentially for r_i, ρ_i, then ρ_f, and then repeats the sequence until the algorithm converges on the solution. In Figure 3.6.13, the minimum along the r_i axis is relatively broad, which indicates that the inversion procedure may need to be run iteratively to reach the best estimate.

The shape of the iso-surfaces plotted in Figure 3.6.13 can be further explained using the Jacobian for each parameter. The Jacobian columns represent the sensitivity to various data points due to changes in each parameter, one column for each parameter. A broad estimate of the sensitivity of the data with respect to each parameter can be made by taking the vertical sum of the Jacobian. For a 3-parameter model, a sample of the absolute value of the vertical sum of the Jacobian matrix is presented in Figure 3.6.16. In Figure 3.6.16 the vertical sums for the ice wall radius and resistivity are nearly the same, and the vertical sums for the formation resistivity are significantly lower. This indicates that the data is much more sensitive to changes in the radius and resistivity of the freeze wall than the formation resistivity. Because of this, the inversion algorithm will not converge to the correct formation resistivity until the freeze wall parameters are near the correct solution.

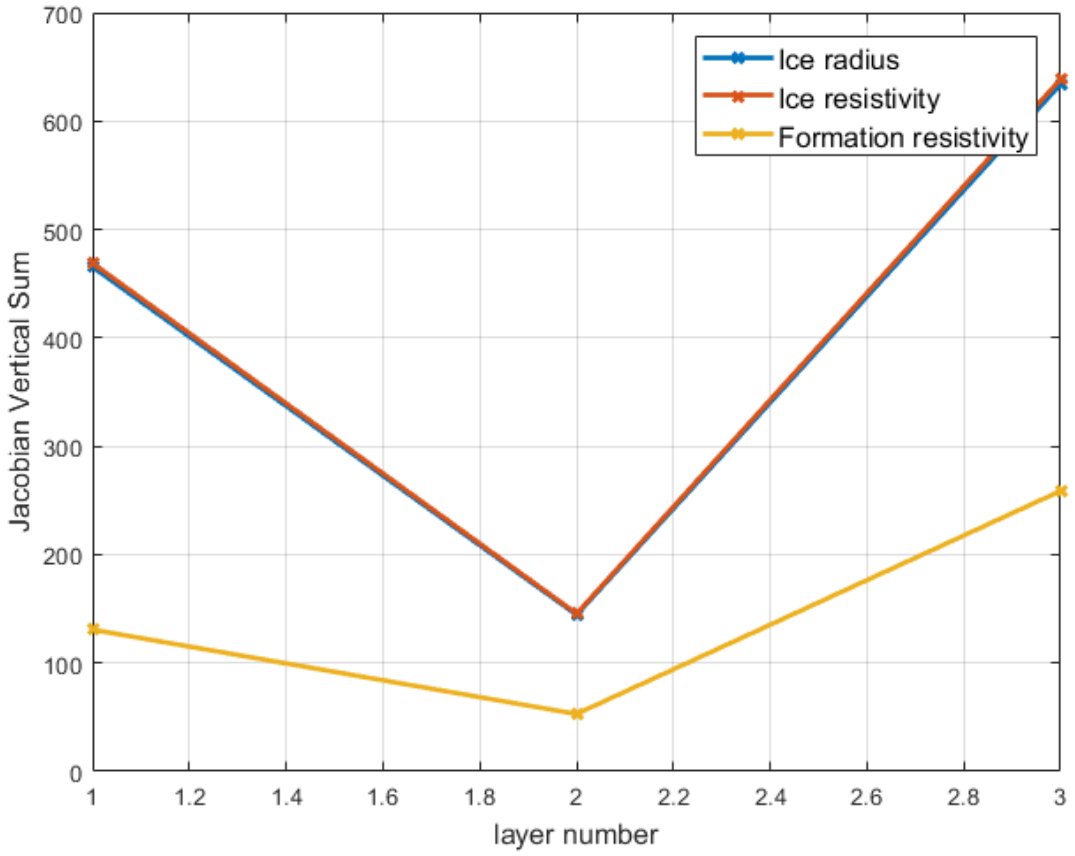

Figure 3.6.16: An illustration of the vertical sum of the Jacobian for the three parameters r_i, ρ_i, and ρ_f for a 3-layer model. In this figure, the vertical sum of the Jacobian represents the sensitivity of the data to changes in a particular parameter. The sensitivities of the r_i and ρ_i parameters are higher than for ρ_f.

In the mining environment that this inversion scheme is intended to be used in, there is a great deal of a priori information about the location of horizon boundaries and the specific properties of the stratigraphic layers. Because of this a priori information, the model layer boundaries for the inversion can be determined based on known stratigraphic boundaries, which reduces the dimensionality of the inversion and allows for the inversion to be run without regularization.

The inversion algorithm uses a Gauss-Seidel style parameter update and consists of the following steps:

Algorithm 1 Cylindrical parametric inversion

recall $\hat{m} = \hat{r}_i, \hat{\rho}_i, \hat{rho}_f$

estimate initial $\hat{r}_i$;

estimate initial $\hat{\rho}_i$ using the 1st n-level from apparent resistivity pseudosection;

estimate initial $\hat{\rho}_f$ using the last n-level from apparent resistivity pseudosection;

while $\|\hat{d}_{obs} - f(\hat{r}_{i(k)}, \hat{\rho}_{i(k)}, \hat{\rho}_{f(k)})\|$ is above stopping threshold **do**

Solve for new $\hat{r}_i$: $\hat{r}_{i(k+1)} = \hat{r}_{i(k)} - \gamma(J_{\hat{r}_i}^T J_{\hat{r}_i})^{-1} J_{\hat{r}_i}^T (d_{obs} - f(\hat{r}_{i(k)}, \hat{\rho}_{i(k)}, \hat{\rho}_{f(k)}))$;

Update $\hat{r}_i$: $\hat{r}_{i(k)} = \hat{r}_{i(k+1)}$;

Solve for new $\hat{\rho}_i$: $\hat{\rho}_{i(k+1)} = \hat{\rho}_{i(k)} - \gamma(J_{\hat{\rho}_i}^T J_{\hat{\rho}_i})^{-1} J_{\hat{\rho}_i}^T (d_{obs} - f(\hat{r}_{i(k)}, \hat{\rho}_{i(k)}, \hat{\rho}_{f(k)}))$;

Update $\hat{\rho}_i$: $\hat{\rho}_{i(k)} = \hat{\rho}_{i(k+1)}$;

Solve for new $\hat{\rho}_f$: $\hat{\rho}_{f(k+1)} = \hat{\rho}_{f(k)} - \gamma(J_{\hat{\rho}_f}^T J_{\hat{\rho}_f})^{-1} J_{\hat{\rho}_f}^T (d_{obs} - f(\hat{r}_{i(k)}, \hat{\rho}_{i(k)}, \hat{\rho}_{f(k)}))$;

Update $\hat{\rho}_f$: $\hat{\rho}_{f(k)} = \hat{\rho}_{f(k+1)}$;

end while

3.6.4 Inversion test

To demonstrate the cylindrical parametric inversion algorithm, a dataset was generated using a cylindrical forward operator on a sample model. The sample model and the apparent resistivity pseudosection for that model are presented in Figure 3.6.17.

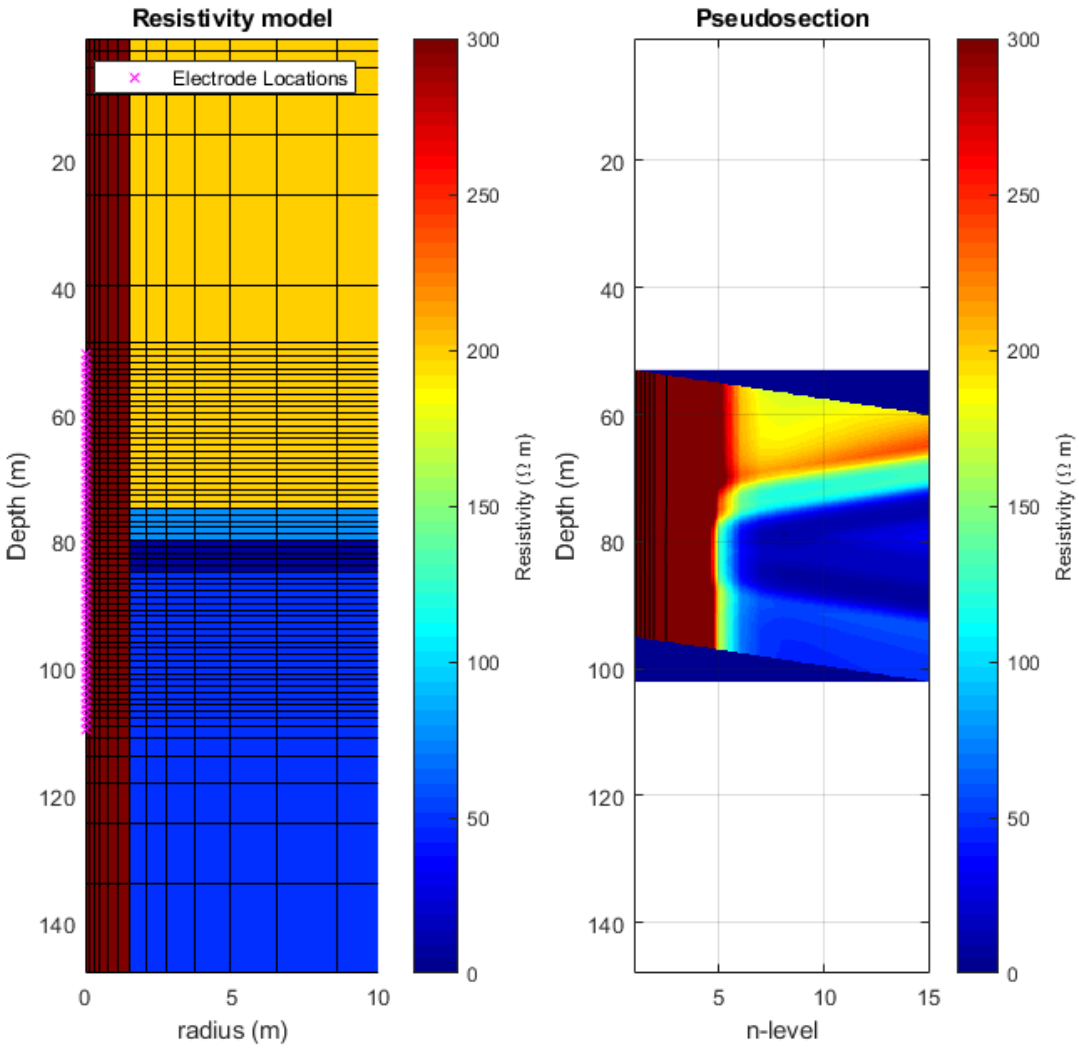

Figure 3.6.17: An illustration of the test model and the apparent resistivity pseudosection generated from that model

To begin the inversion, initial guesses for r_i, ρ_i, and ρ_f need to be made. The initial guess for r_i can be made on the basis of how thick the wall is expected to be. The initial guess for ρ_i is

estimated as what the resistivity of the ice is expected to be on the basis of Equation (3.12). On the basis of Figure 3.6.14, the shape of the misfit space is smooth and convex within a range of $\pm 30\%$ of the true r_i and ρ_i values, meaning that the inversion should converge if the initial guess is within this range. The initial guess for ρ_f is the mean value of the apparent resistivities at the largest n-spacing.

For the model presented in Figure 3.6.17, the initial model is presented in Figure 3.6.18. Figure 3.6.19 presents the r_i, ρ_i, and ρ_f parameter changes through the inversion process. In Figure 3.6.19, the thick black lines represent the initial guesses, and the thick blue lines represent the final estimates. In Figure 3.6.19 the r_i parameter initially moves in the wrong direction, but through the iterative procedure is steered back in the right direction after 3 iterations. The final estimates in Figure 3.6.19 are presented in Figure 3.6.20.

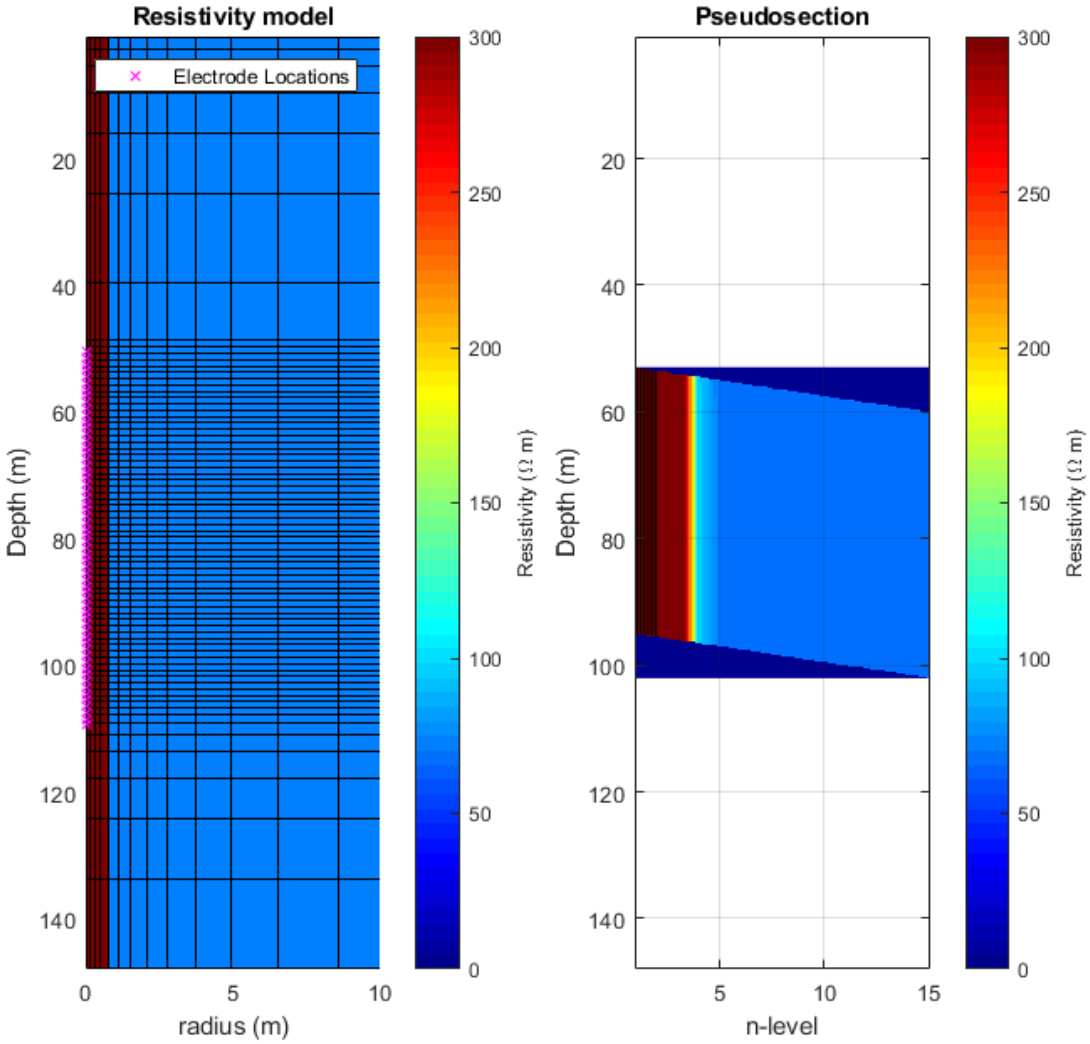

Figure 3.6.18: An illustration of the test model and the apparent resistivity pseudosection generated from that model

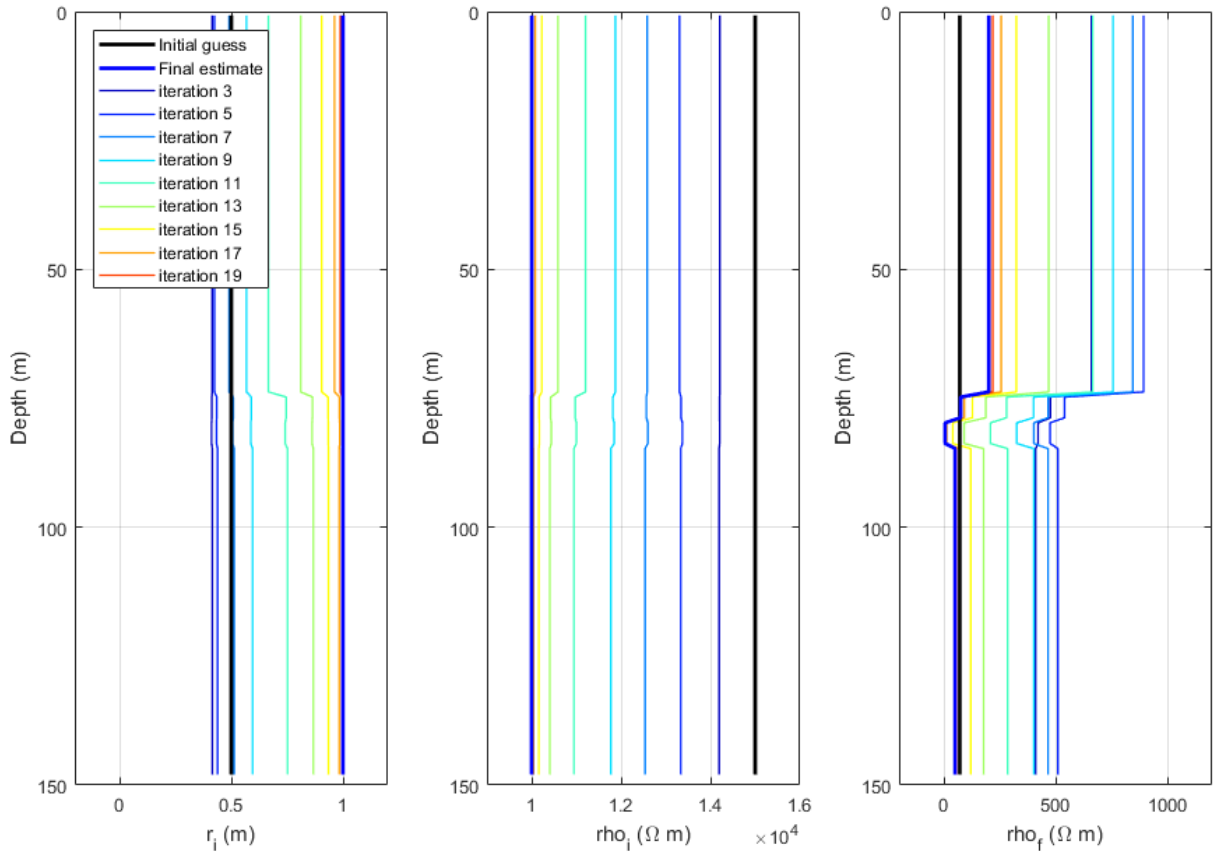

Figure 3.6.19: Illustration of the r_i, ρ_i, and ρ_f parameters through the inversion process. Each of the parameters settles on the correct value, even though the initial iteration direction may not be correct.

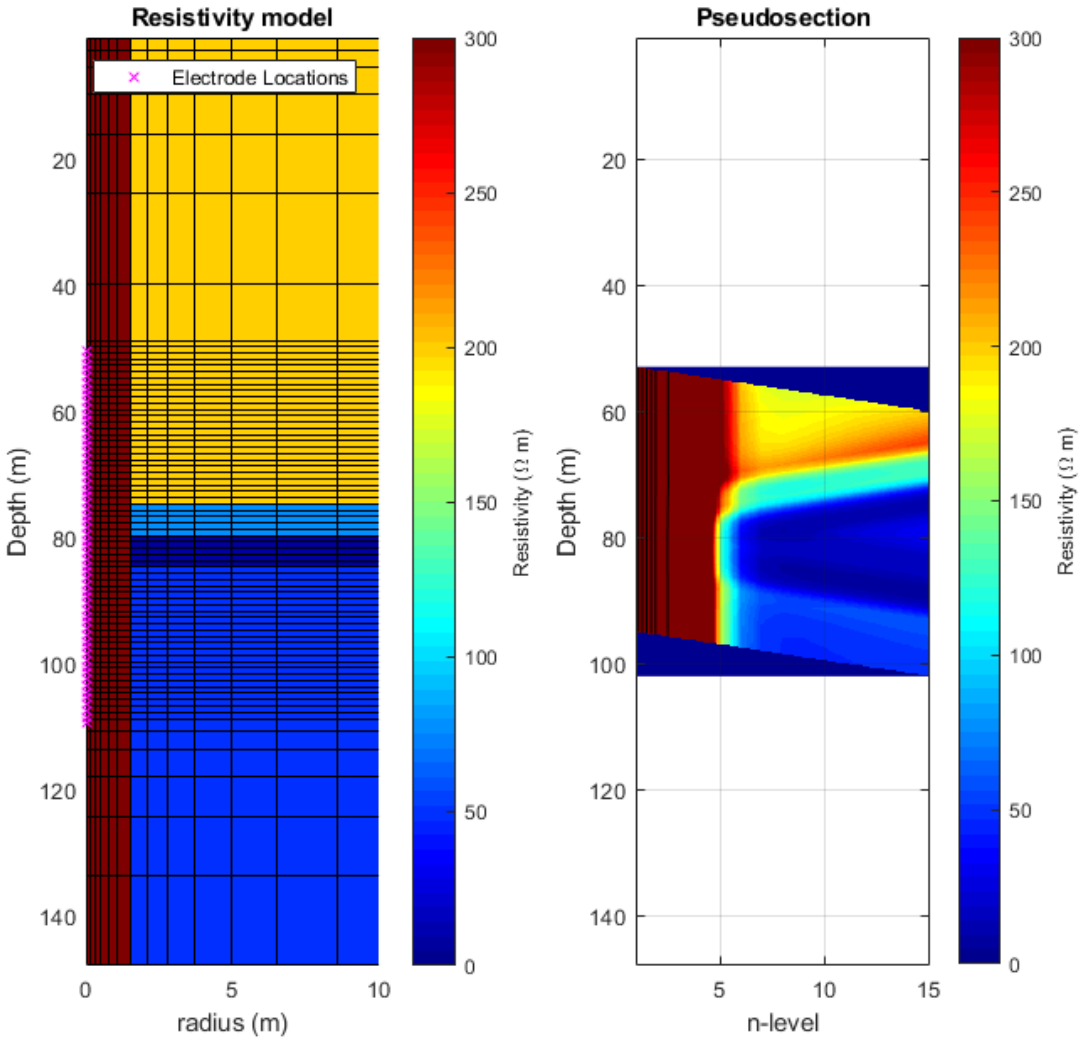

Figure 3.6.20: An illustration of the test model and the apparent resistivity pseudosection generated from that model

The final estimate produced by the inversion algorithm (Figure 3.6.20) is very close to the original model. The original model, final estimate, and estimate error are presented in Figure 3.6.21. In Figure 3.6.21 the error is below 1 %, which indicates that the inversion can match the input model for data simulated using the same discretization as the inversion algorithm.

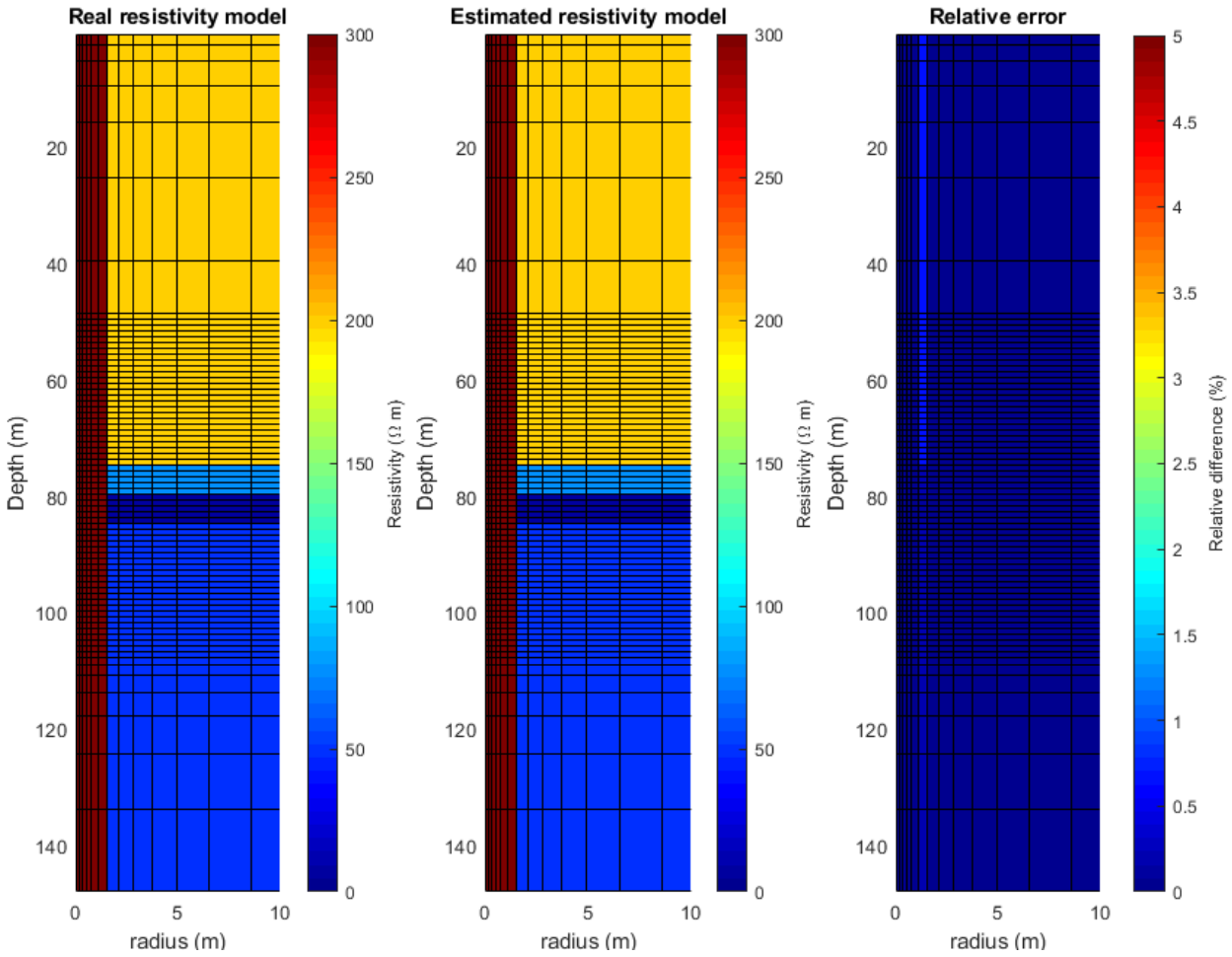

Figure 3.6.21: The true model, estimated model, and the difference between the true and estimated models

Chapter 4

Simulation

The simulation is intended to test the use of single-borehole ERT as a monitoring solution in the case of a freeze wall breach. There has not been a case where a freeze wall has been breached in the conditions described in this thesis, so the TDS concentration data and its effect on electrical resistivity has been simulated. A description of the geological model that the simulation is being contructed within, the details surrounding the simulation of the wall breach, and the results of the monitoring survey using single-borehole ERT are presented in the following subsections. The results of the simulation will be used as the basis for a discussion in the following section on the advantages and the limitations of the method as a monitoring solution for a freeze wall.

4.1 Geological model for simulation

For the simulated wall breach, a series of data from 10 wells were simulated from wells situated along the freeze wall. Figure 4.1.1 presents the layout of the wells in plan view.

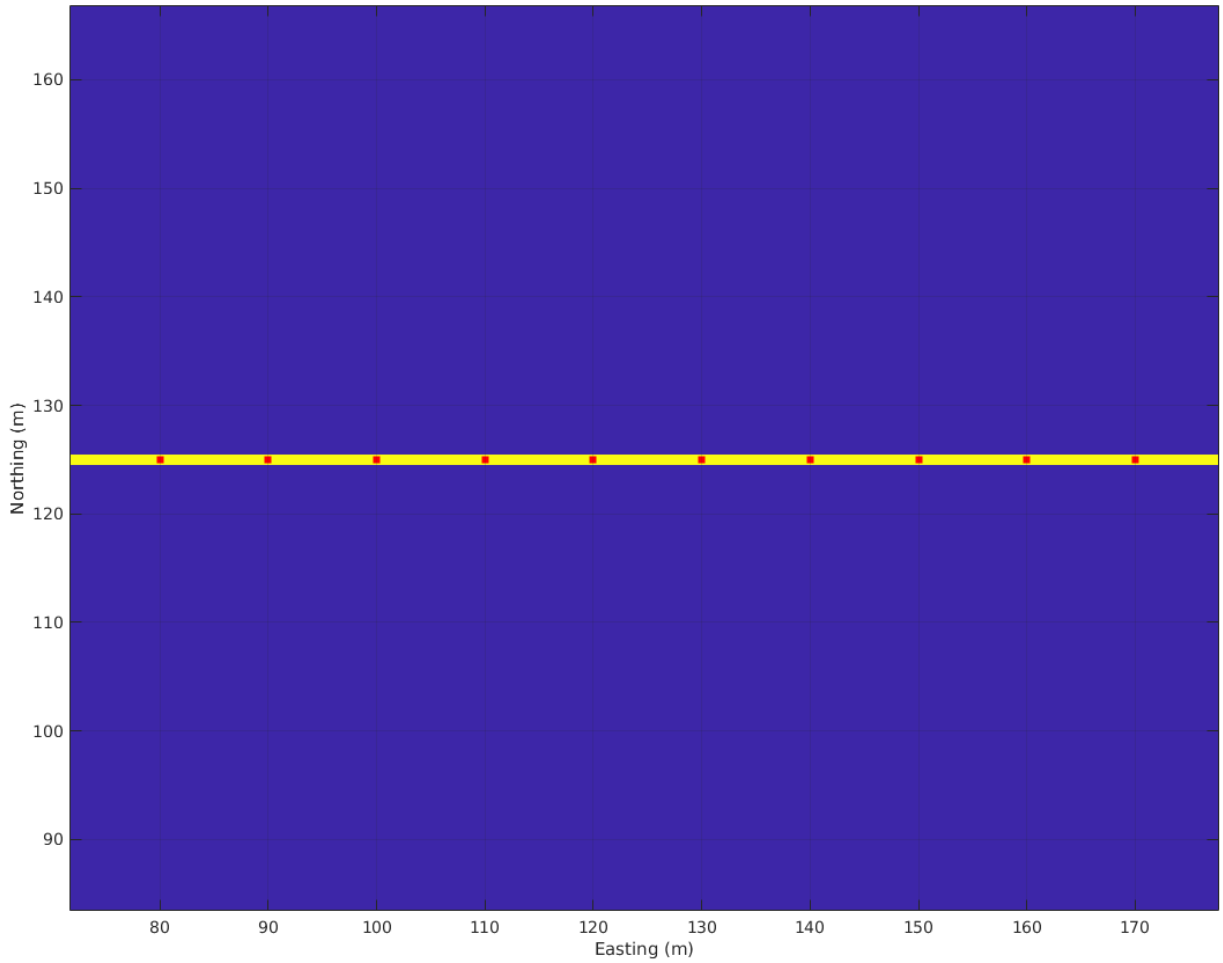

Figure 4.1.1: Plan view of the location of the freeze wall monitoring wells. The freeze wall is plotted in yellow and the wells are plotted as red dots

Figure 4.1.2 presents the baseline model cross section in electrical resistivity in the y-direction. In Figure 4.1.2, the layer above the aquifer has a resistivity of 100 Ω*m*, the layer below the aquifer has a resistivity of 75 Ω*m*, the aquifer resistivity on the outside of the mine is 6 Ω*m*, and the aquifer resistivity inside the mine is 304 Ω*m*. The resistivity values in the aquifer on the inside and outside of the wall were calculated using Archie's equation (3.4) and Crain's equation (3.5) with the following parameters:

Parameter	Value
cementation factor (m)	1.3
porosity (ϕ)	0.3
water saturation (S_w)	1
tortuosity (a)	1
saturation exponent (n)	2
water temperature	35 ° F
TDS outside of the wall	10000 ppm
TDS inside of the wall	100 ppm

The parameters on the mine (inside) of the wall are simplified, as the water on the mine side would be drawn down to facilitate mining, which would complicate the calculation of electrical resistivities on the mine side of the freeze wall as the water saturation would not be constant. An improvement to this simulation can be made by more accurately calculating the resistivities on the mine side of the freeze wall, but since the hydrogeological conditions on the mine side of the wall are beyond the scope of this study, the simplification will be used for the simulation.

The zones above and below the fresh water aquifer are assumed to be aquitards. This assumption is based on the cross section that was presented in Figure 2.1.1: the unit overlying the aquifer is the McMurray Formation, which is saturated with bitumen, greatly reducing its hydraulic conductivity; the unit below the aquifer is the Devonian Limestone, which has very low porosity, making it an aquitard. The assumption is not necessarily true, as the Devonian surface is an unconformity that has been subjected to karsting and vertical fracturing (Broughton, 2013); weathering on the Devonian surface from pre-Cretaceous deposition may make portions of the Devonian permeable.

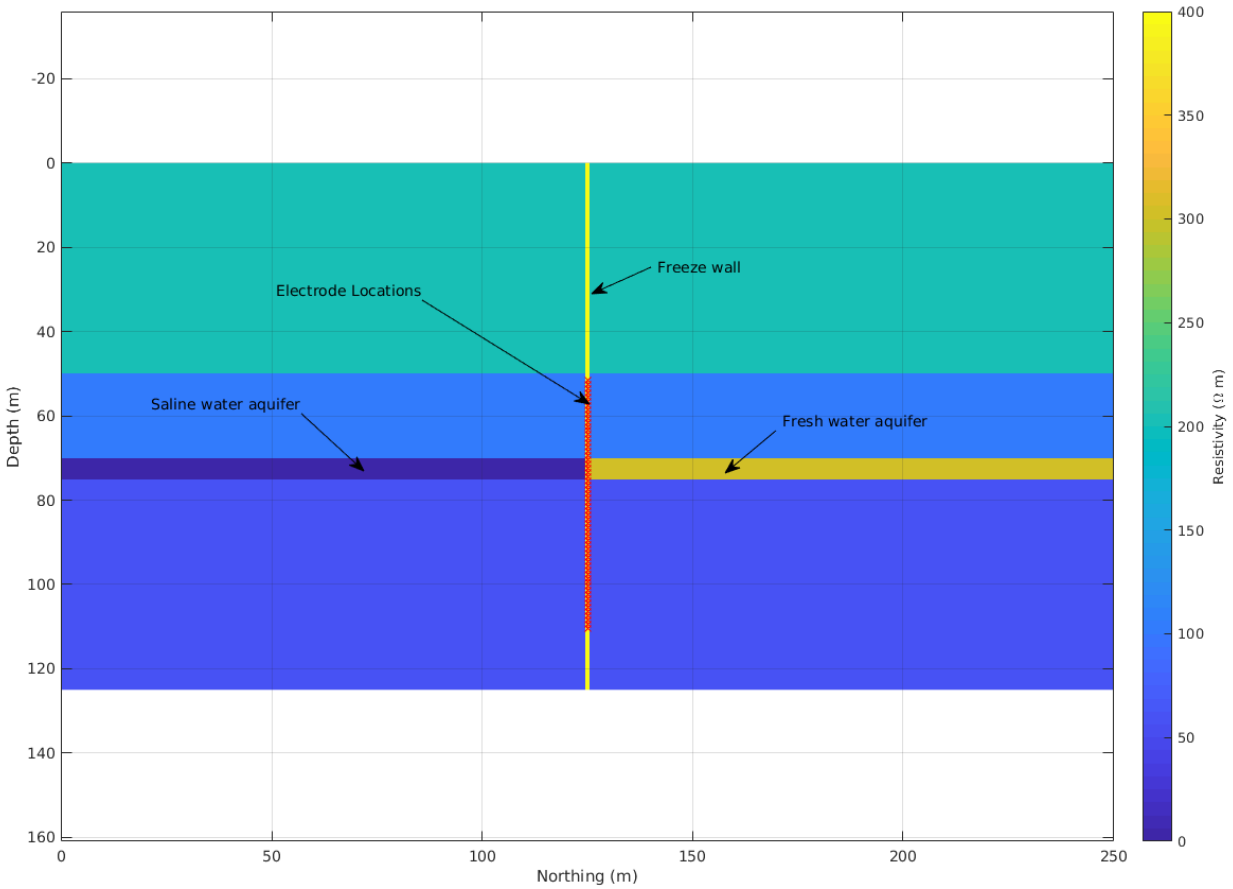

Figure 4.1.2: Illustration of the freeze wall in situ in section view. The electrode array location is marked by the red x's that sit within the freeze wall. On one side of the freeze wall there is a saline water aquifer, and on the other side there is a fresh water aquifer.

Figure 4.1.3 presents the initial resistivities of the basal McMurray aquifer in plan view. In Figure 4.1.3 the breach location is at 62 m E, and the monitoring wells are centred over the leak. On the north side of the freeze wall lies the low resistivity formation associated with the saline aquifer, and on the south side of the wall lies the relatively high resistivity formation associated with the non-saline aquifer.

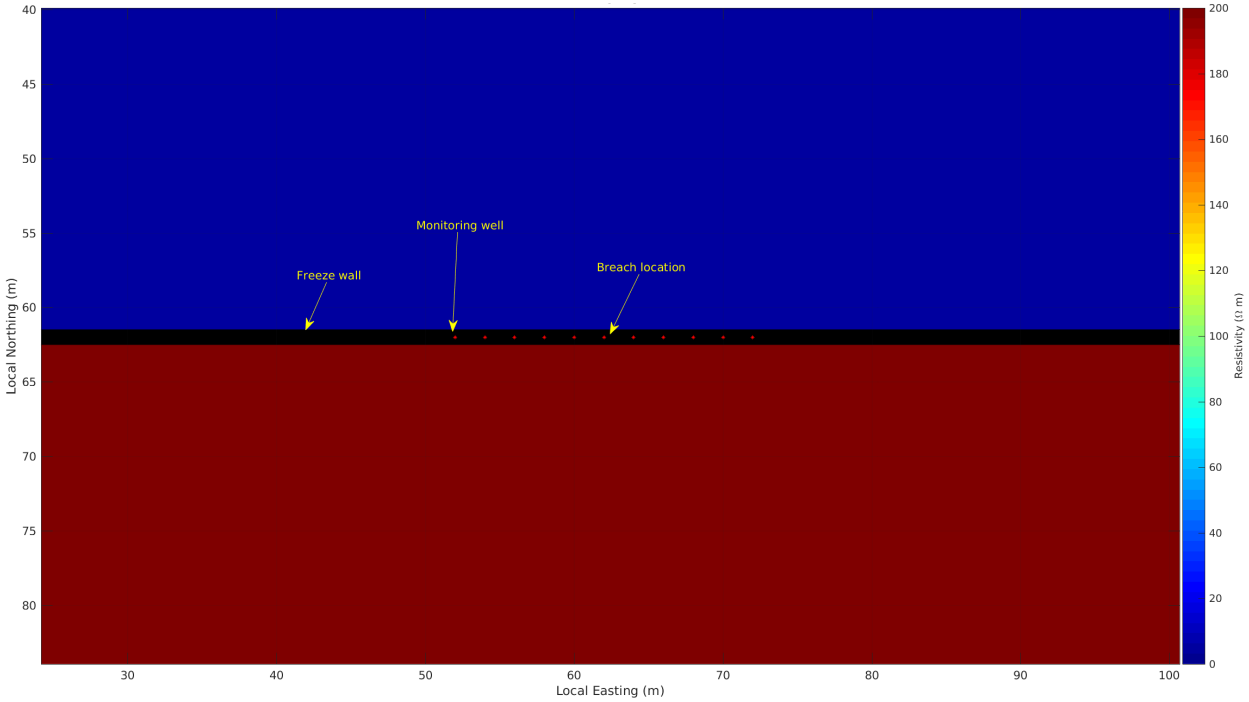

Figure 4.1.3: Map view of the electrical resistivities of the basal aquifer at the beginning of the simulation. The saline portion of the survey domain is in the north and the non-saline portion of the survey domain is in the south.

4.1.1 Breach simulation

For this thesis, within the basal McMurray aquifer, the dispersion coefficient (D_x,D_y) in Equation (3.1) was a constant value within the unfrozen portion at 0.5 L/min, and 0 L/min in the frozen portion. The initial concentration of the contaminant C is 10,000 ppm on the outside of the freeze wall, and 100 ppm on the inside of the freeze wall. The initial TDS value on the inside of the freeze wall was chosen for stability, as the resistivity of the pore water becomes excessively large at very low TDS. Figure 4.1.4 presents the initial concentration C in the basal McMurray aquifer.

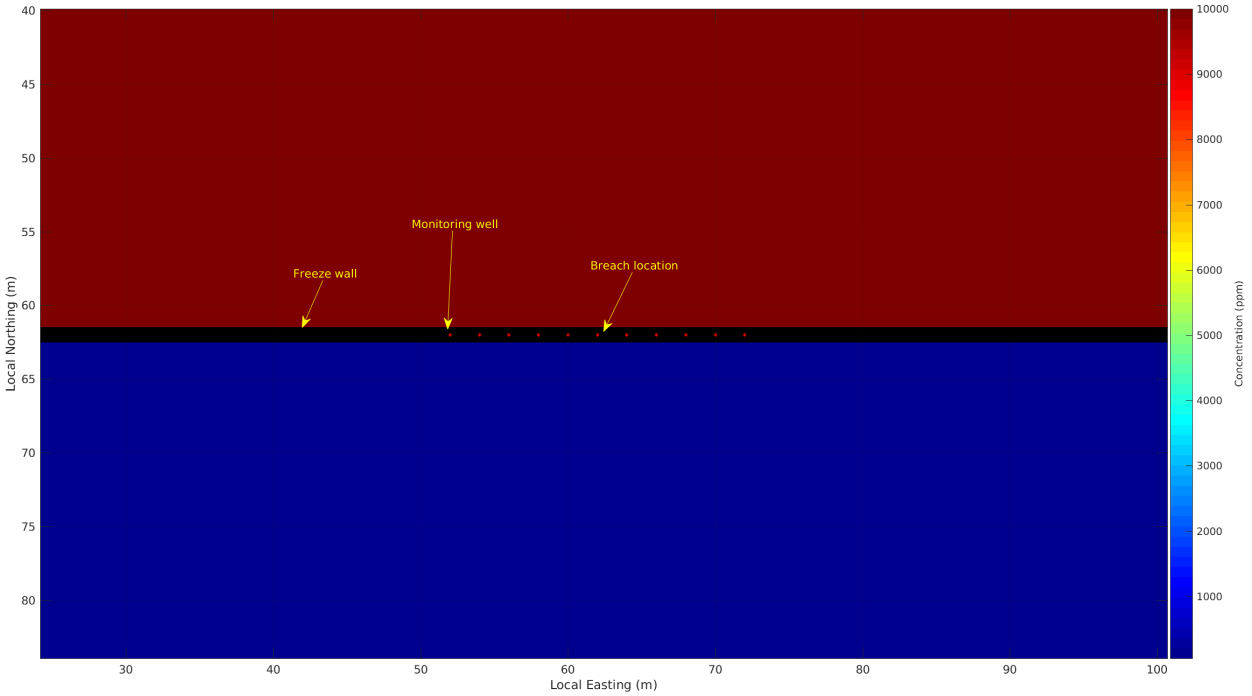

Figure 4.1.4: Map view of the initial concentration of chloride ions in the basal McMurray aquifer

The hydraulic conductivity used for the simulation was a constant 10^{-4} m/s within the unfrozen basal McMurray aquifer and a constant 10^{-17} m/s in the frozen portion of the wall. These hydraulic conductivities assume that the frozen portion of the wall is uniform, which is a simplification. In reality, the wall will not freeze in a uniform manner (cf. Dillon, H. and Andersland, O., 1966; Banin and Anderson, 1974; Xiao et al., 2017), but the freezing of an ice wall in a saline environment is

beyond the scope of thesis and the simplified model was used for the simulation. Figure 4.1.5 presents an illustration of the hydraulic conductivity in the survey domain.

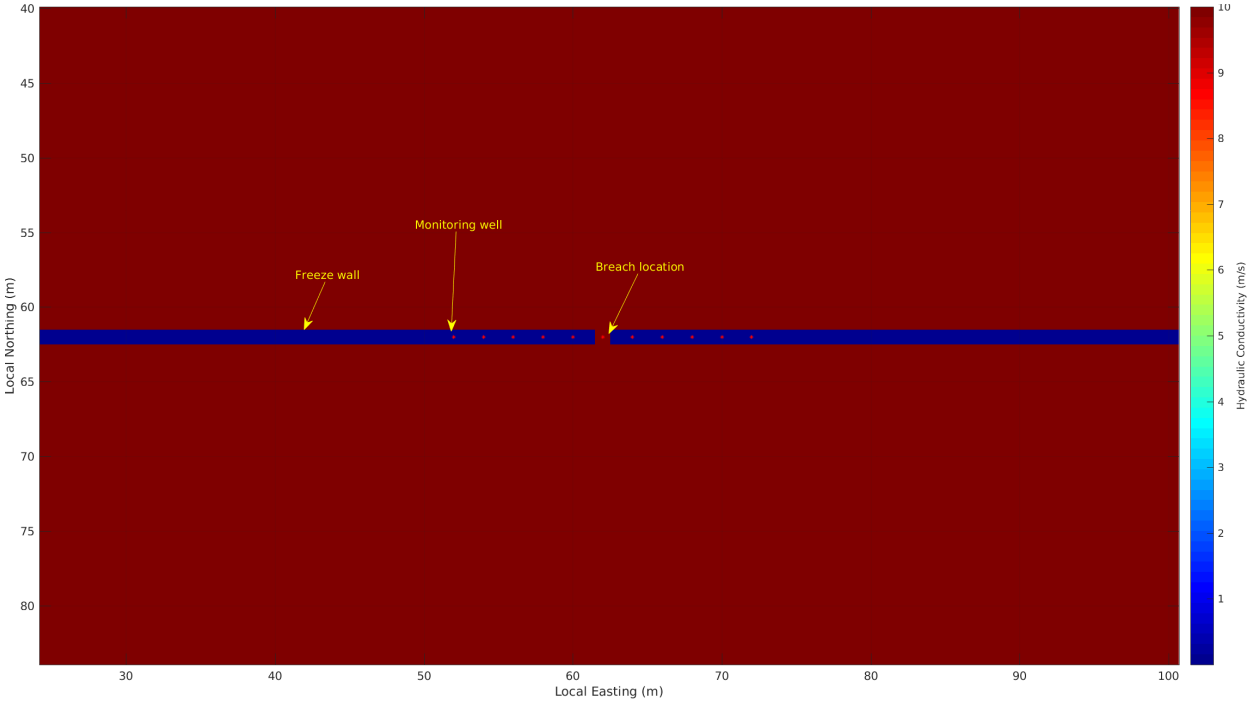

Figure 4.1.5: Map view of the hydraulic conductivity within the survey domain. At the breach location, the hydraulic conductivity is increased to match that of the formation, and allowing water to cross the wall.

The effective porosity used for the simulation was a constant 30% within the Basal McMurray aquifer, which was chosen on the basis of the well logs from Jo and Ha (2013). The hydraulic head level across the test area assumed a head of 400 m outside of the freeze wall, and 300 m on the inside of the wall, assuming that the mine is being de-watered for mining operations. Because the mine is being actively de-watered, the hydraulic head level for the entire simulation remains constant.

To simulate a leak in the wall, the hydraulic conductivity and dispersion coefficients for a small portion of the freeze wall were modified to match the aquifer, which allowed for contaminant transport to take place through the wall. The initiation of the breach is a simplification; a breach

in reality would likely not happen instantly, but instead, it would develop as a gradual increase of hydraulic conductivity over time.

The TDS concentrations from the simulation have been converted to electrical resistivity using Archie's equation (3.4), and are presented in Figures 4.1.6 and 4.1.7. The results displayed in Figures 4.1.6 and 4.1.7 will be used to test the algorithm described in this thesis. Figure 4.1.8 presents time-lapse graphs of the electrical resistivity along a profile perpendicular to the freeze wall centred at 62 m E, or directly over the breach.

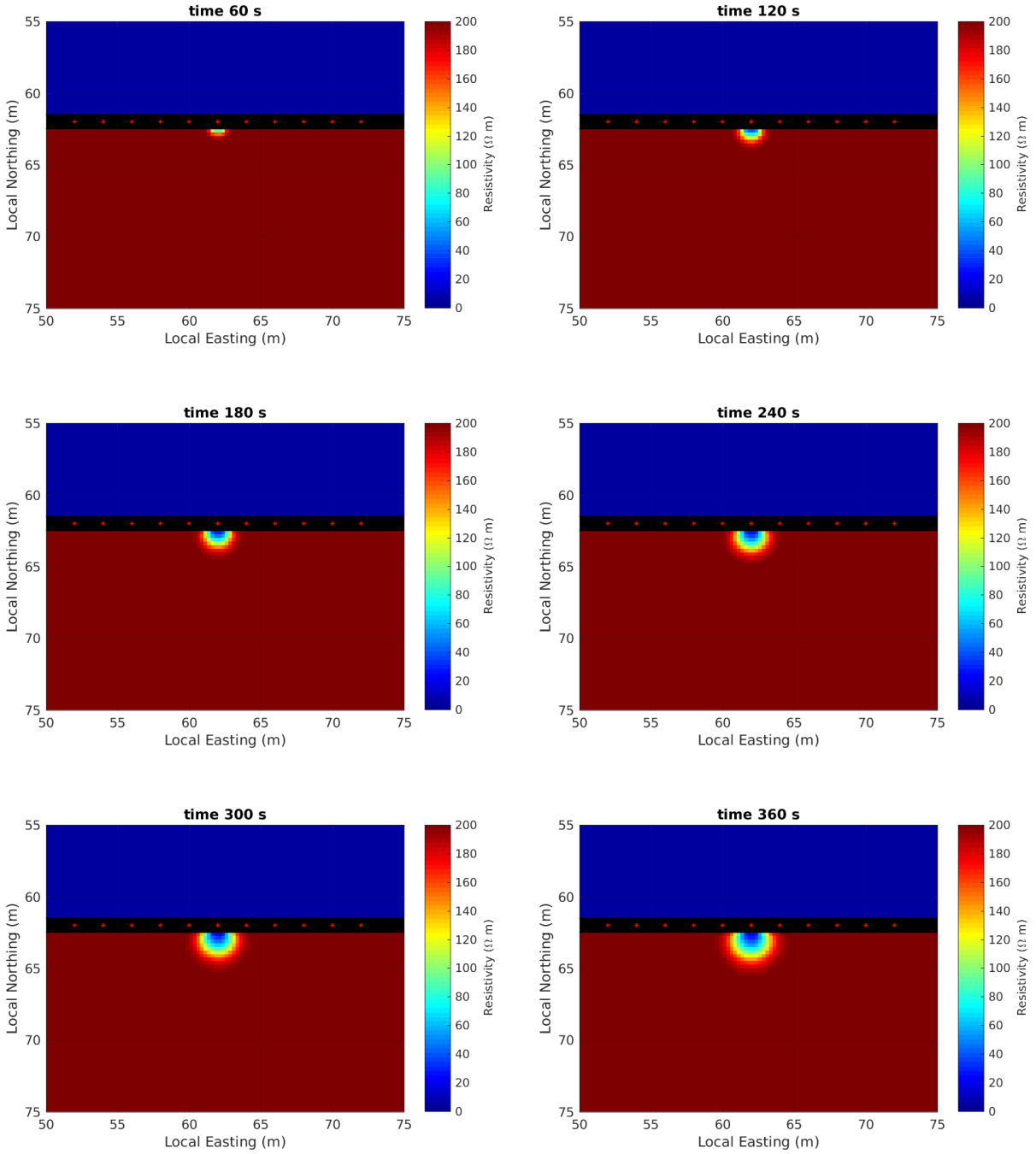

Figure 4.1.6: Simulated freeze wall breech at several time steps - converted to electrical resistivity using Archie's equation

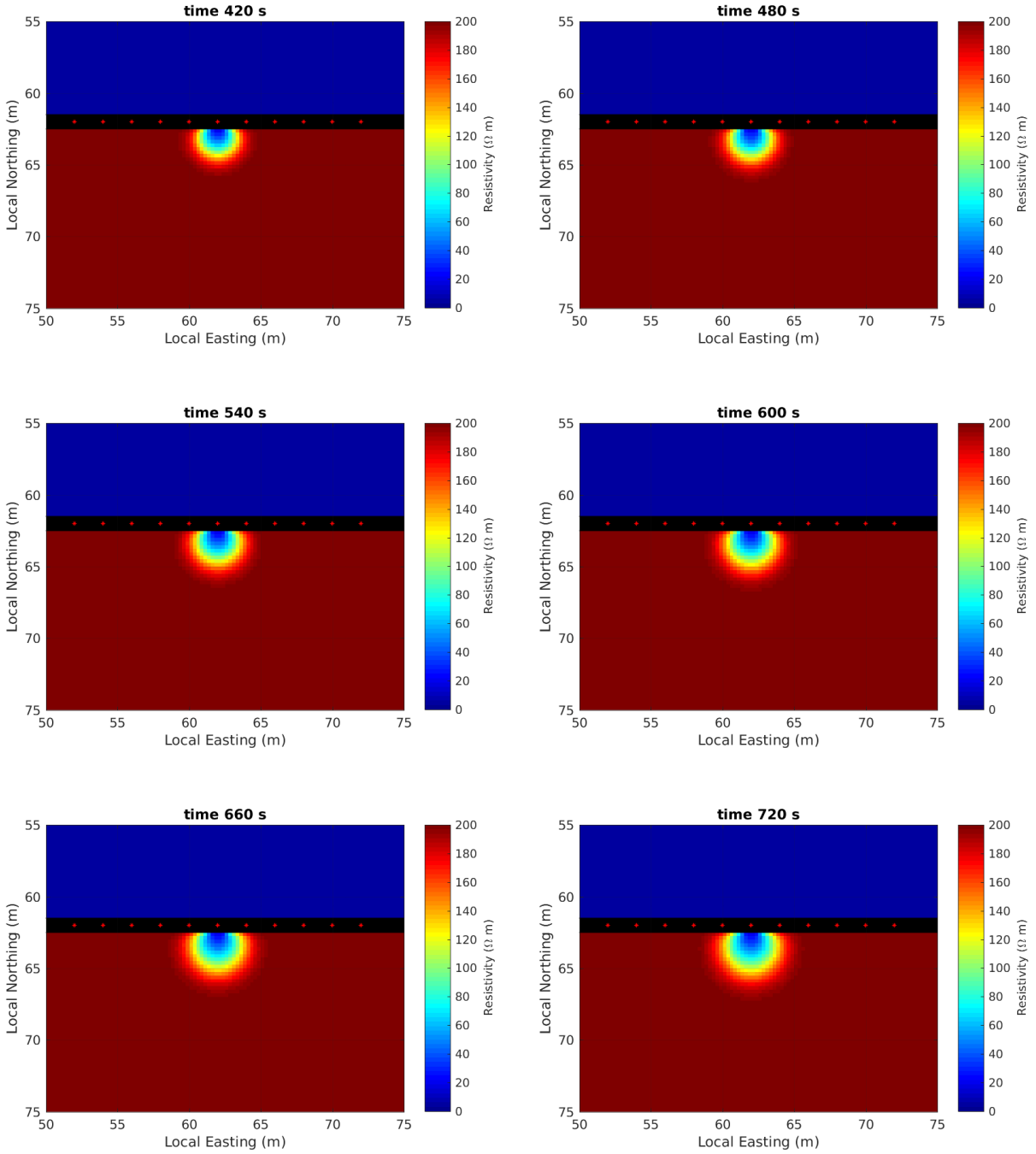

Figure 4.1.7: Simulated freeze wall breech at several time steps - converted to electrical resistivity using Archie's equation

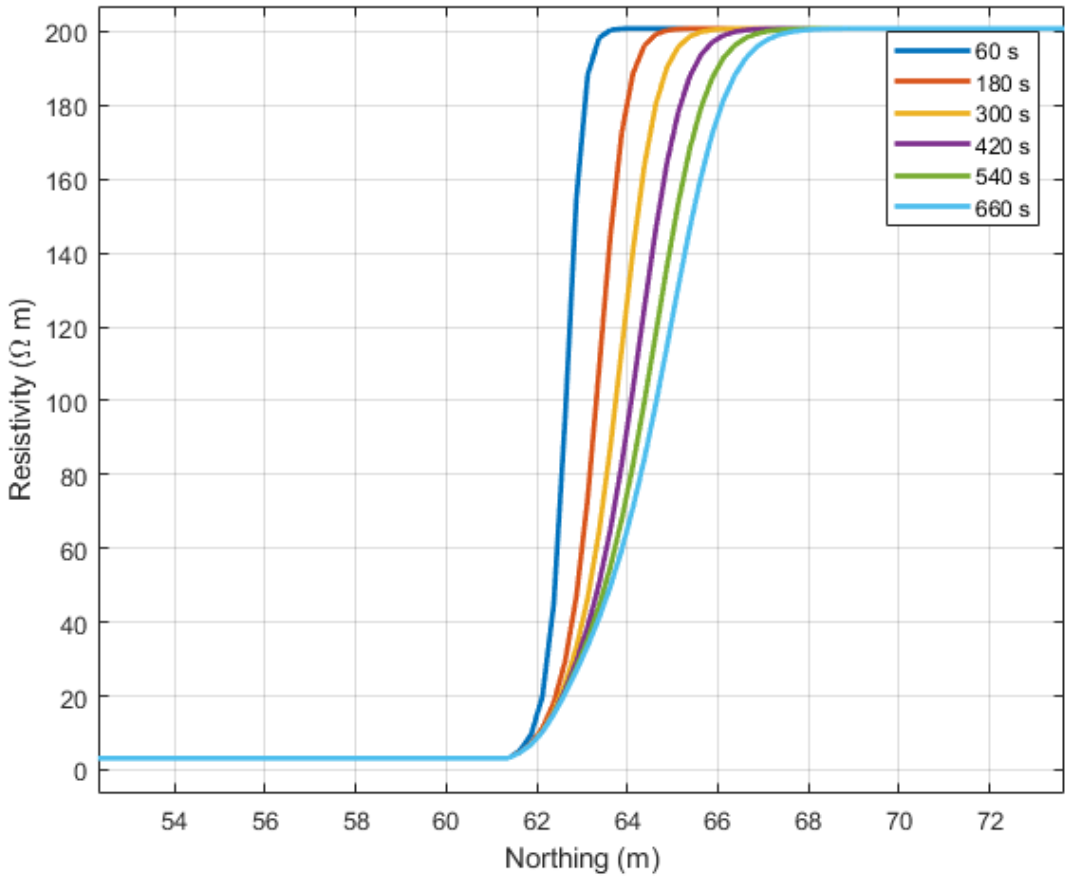

Figure 4.1.8: Graph of electrical resistivities within the basal aquifer along a profile perpendicular to the freeze wall. The X-position of the curves is at 62 m E, centred over the breach.

4.1.2 Data simulation

The data were simulated along the freeze wall at each of 11 borehole locations using the Cartesian discretization. The simulated model presented in Figure 4.1.6 was discretized at a 25 cm cell size and is presented in Figure 4.1.9.

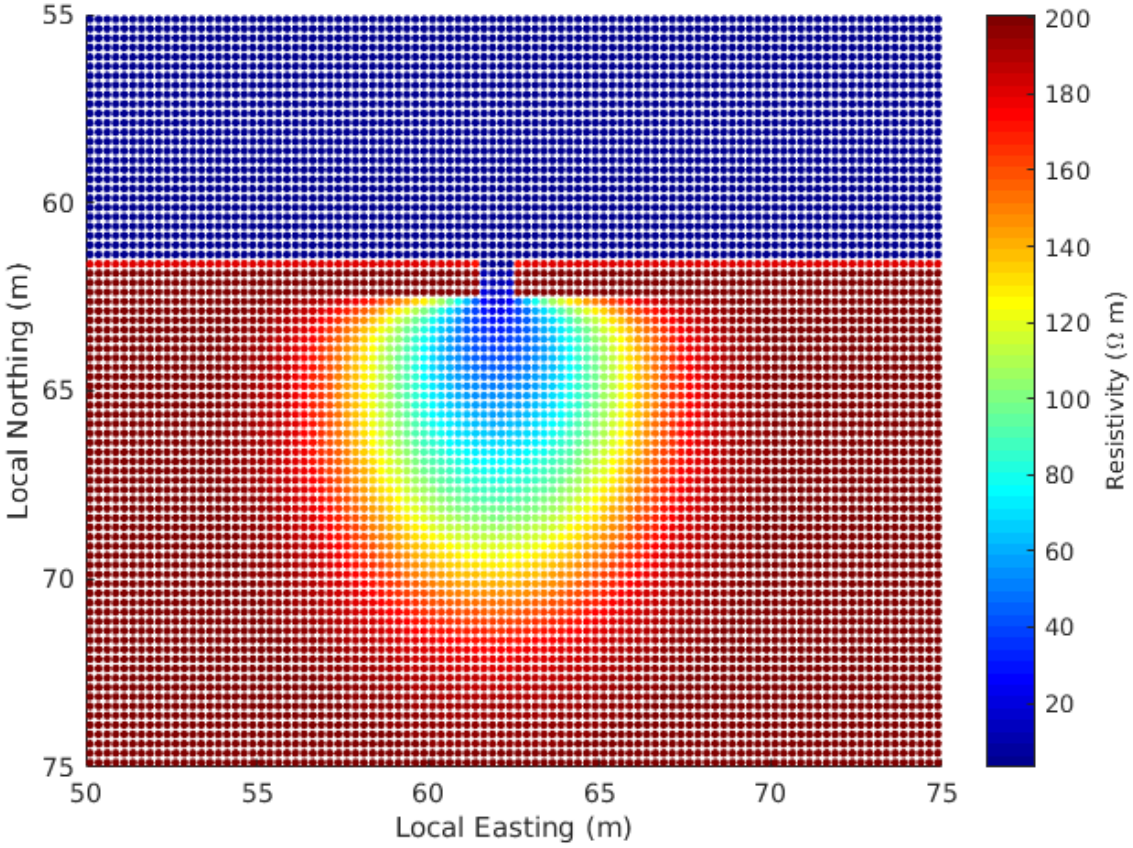

Figure 4.1.9: Illustration of the discretized model in plan view used to simulate data over the leak. The simulation was performed using 25 cm cells, spaced equally throughout the survey domain.

In Figure 4.1.9, the dots represent cell centres, and the colors represent the electrical resistivity. Simulating the data on this grid for the entire survey domain would be computationally expensive, and not practical for the average desktop computer, so a less expensive simulation procedure was used. For the simulation at each borehole, the full model was sampled using a grid with cell

size refinement near the borehole. Figure 4.1.10 presents an example of the interpolated grid cell locations relative to the borehole.

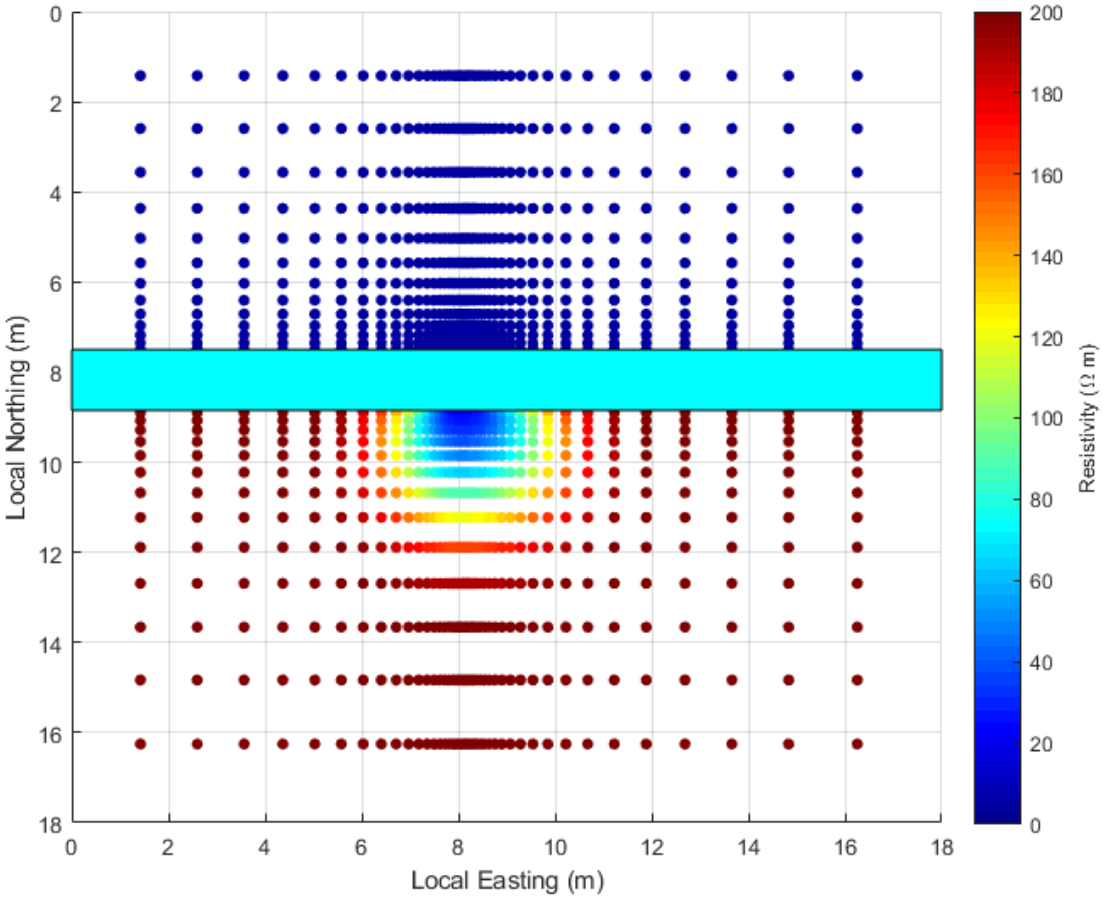

Figure 4.1.10: A map view of the cylindrical discretized model in plan view used during the inversion process. The variable discretization that is used causes the leak location to be reasonably well covered when the leak is close to the monitoring well being surveyed. The freeze wall is indicated by a cyan rectangle.

Figure 4.1.11 presents an example of the interpolated grid cell resistivities for a well at the breach location and far from the breach location. While the coarse mesh refinement at a distance from the borehole improves computation time, in some cases the breach is poorly resolved because it falls into the coarsly refined portion of the mesh. This may result in error due to the fact that the electrical resistivity changes rapidly around the breach, and that will not be captured at a great

resolution for wells that are farther from the breach location.

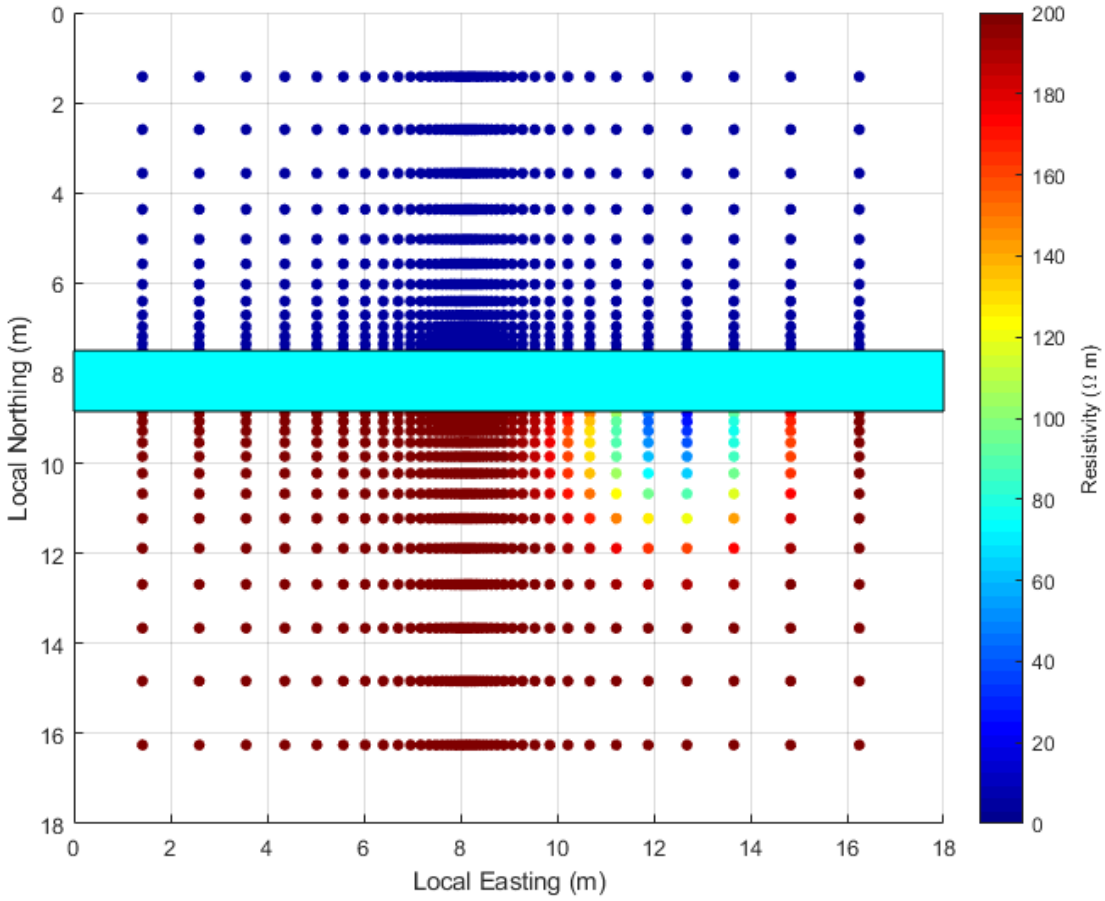

Figure 4.1.11: A map view of the cylindrical discretized model in plan view used during the inversion process. The variable discretization that is used causes the leak location to be sparsely covered when the leak is offset from the monitoring well being surveyed. The freeze wall is indicated by a cyan rectangle.

4.2 Presentation of simulation results

The simulated data are presented as pseudosections for the 11 drillholes along the freeze wall. Figures 4.2.1 to 4.2.3 present examples of the simulated data from the beginning of the experiment at $t = 2,\ 6,\ and\ 10\ min$ respectively.

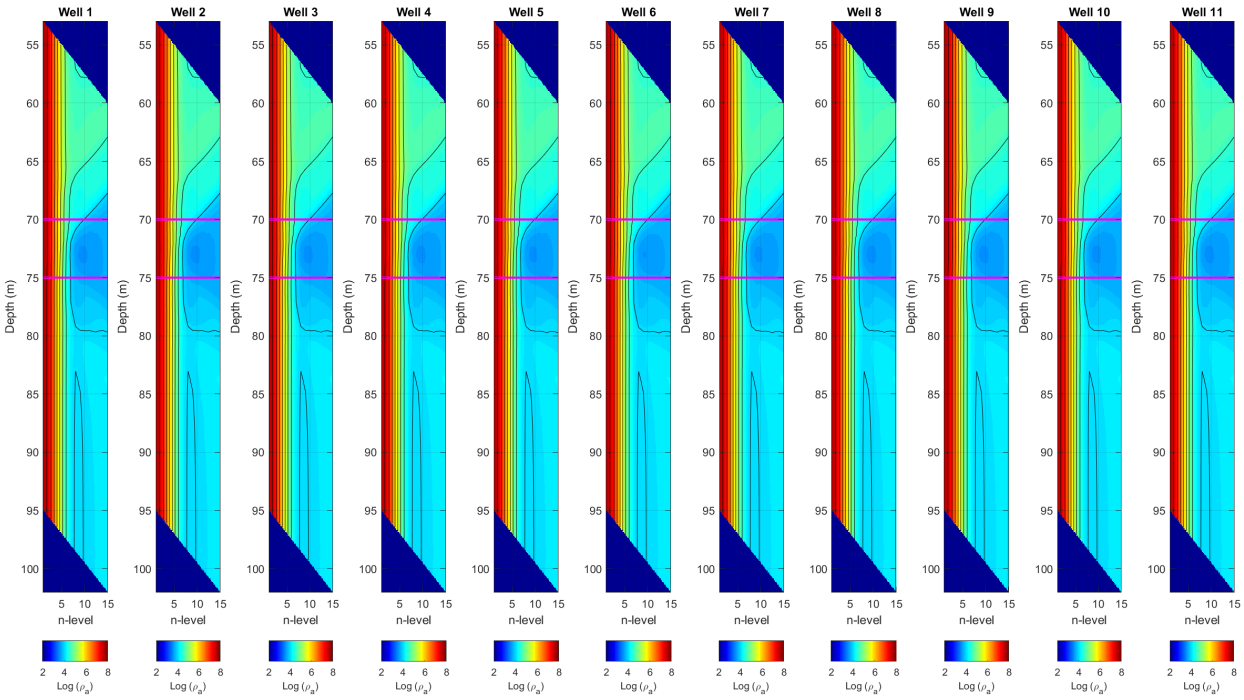

Figure 4.2.1: Simulated data from the beginning of the experiment (2 min). The top and bottom of the aquifer are indicated by magenta lines.

The simulated data are presented as difference plots from the beginning of the experiment (i.e. prior to the simulated breach). Figures 4.2.4 to 4.2.6 present difference plots at $t = 2,\ 6,\ and\ 10\ min$ respectively.

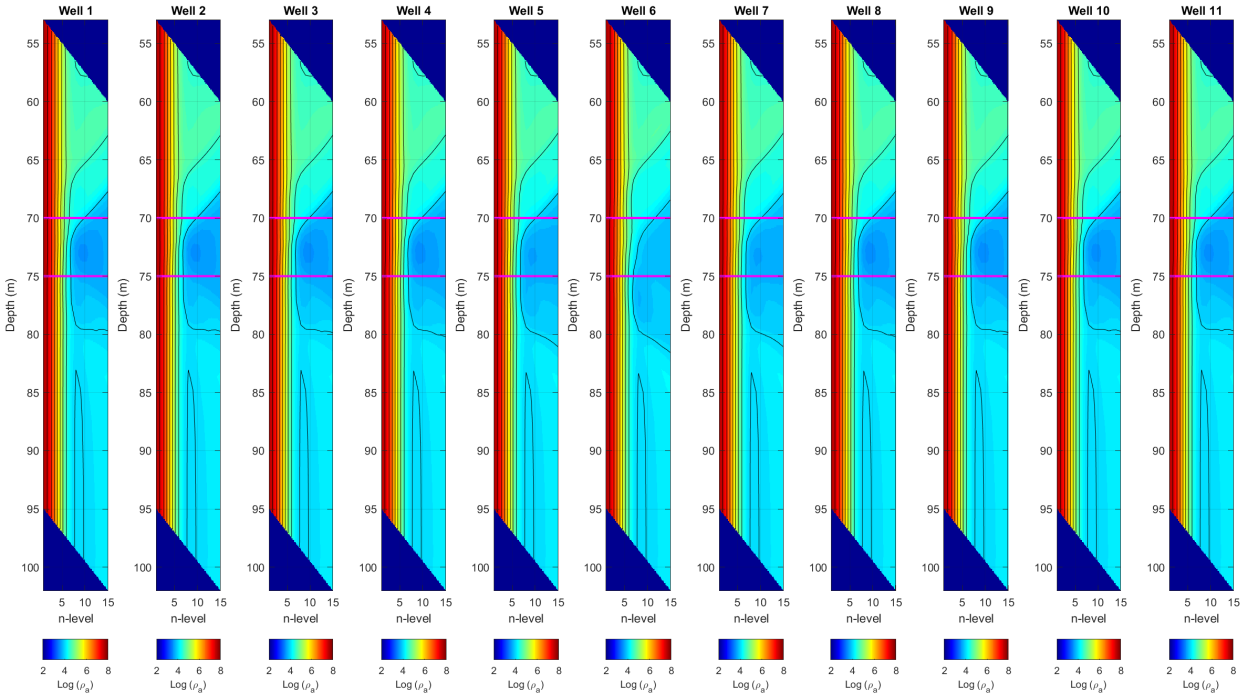

Figure 4.2.2: Simulated data from the middle of the experiment (6 min). The top and bottom of the aquifer are indicated by magenta lines.

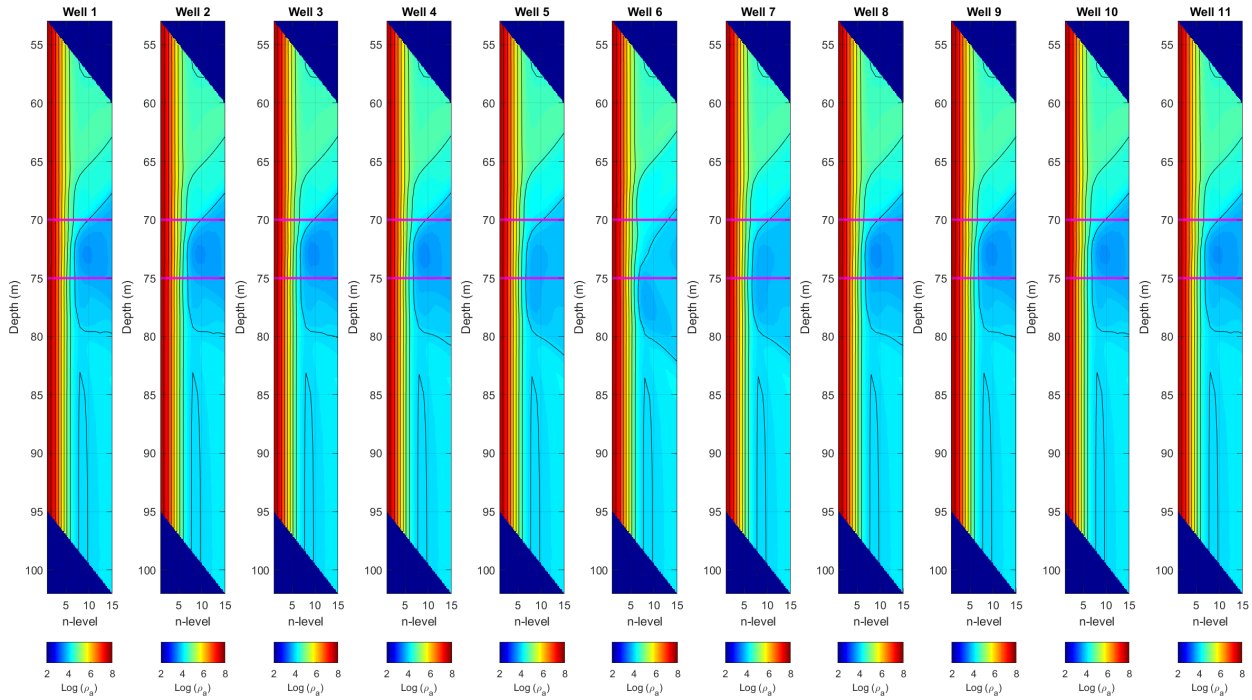

Figure 4.2.3: Simulated data from the end of the experiment (10 min). The top and bottom of the aquifer are indicated by magenta lines.

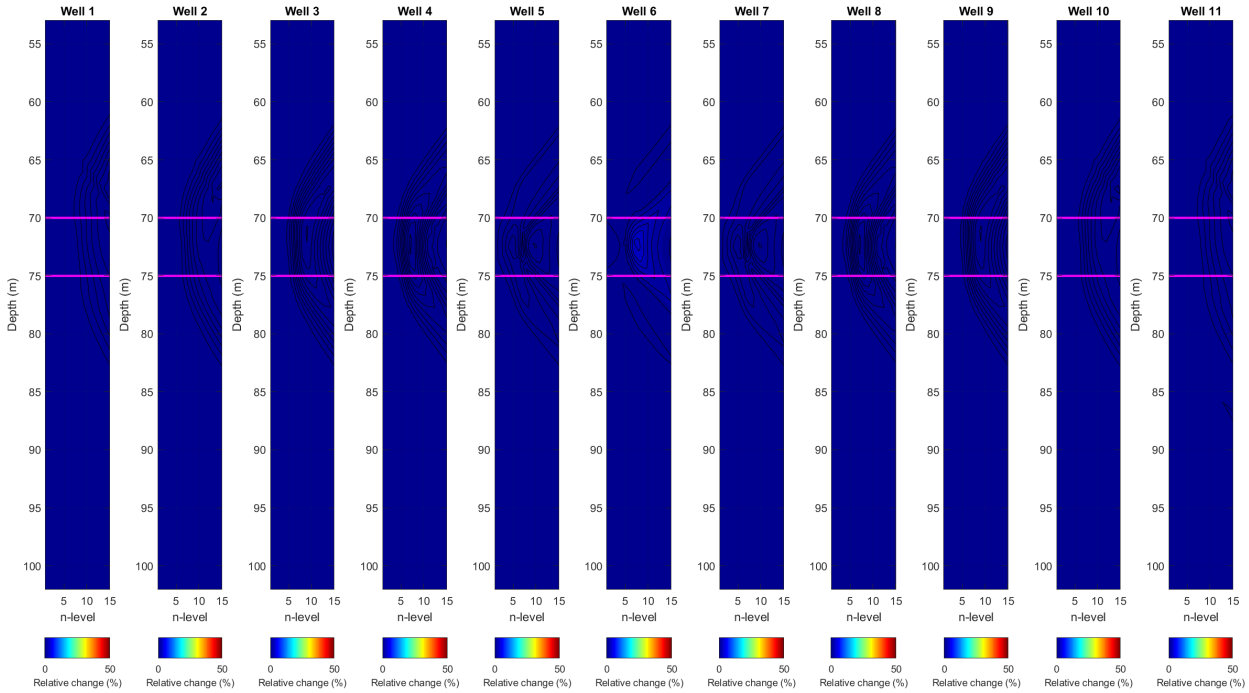

Figure 4.2.4: Simulated difference from the beginning of the experiment (2 min). The top and bottom of the aquifer are indicated by magenta lines.

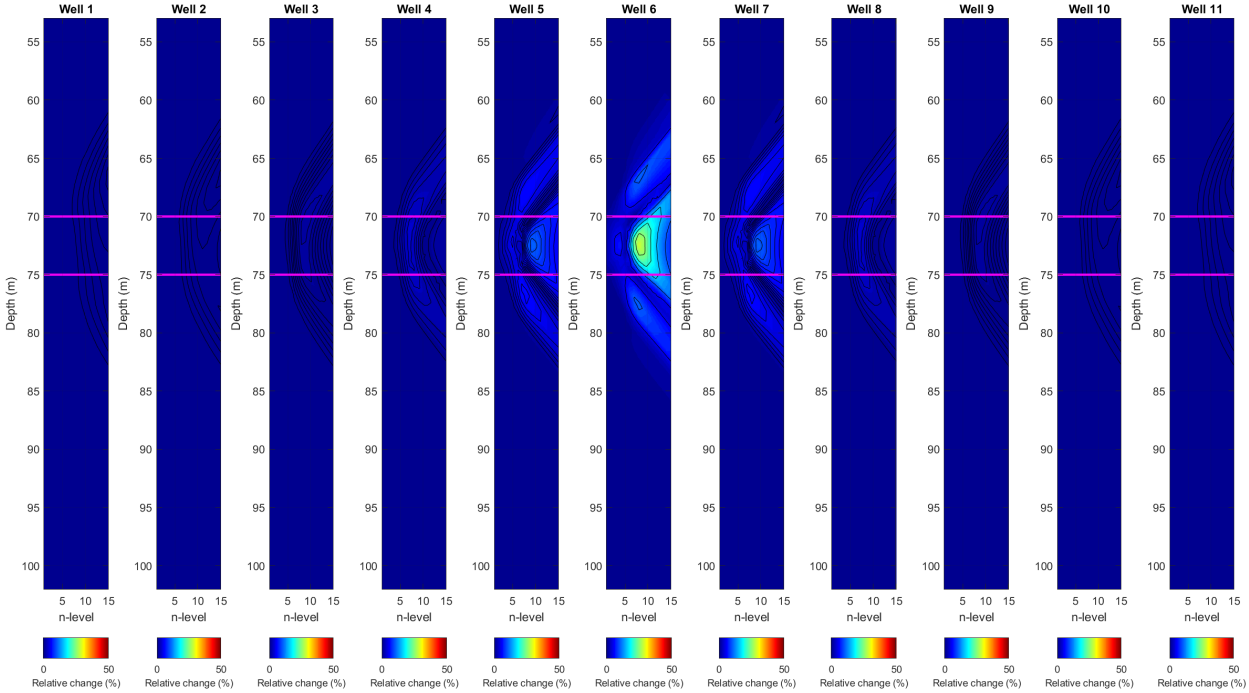

Figure 4.2.5: Simulated difference from the middle of the experiment (6 min). The top and bottom of the aquifer are indicated by magenta lines.

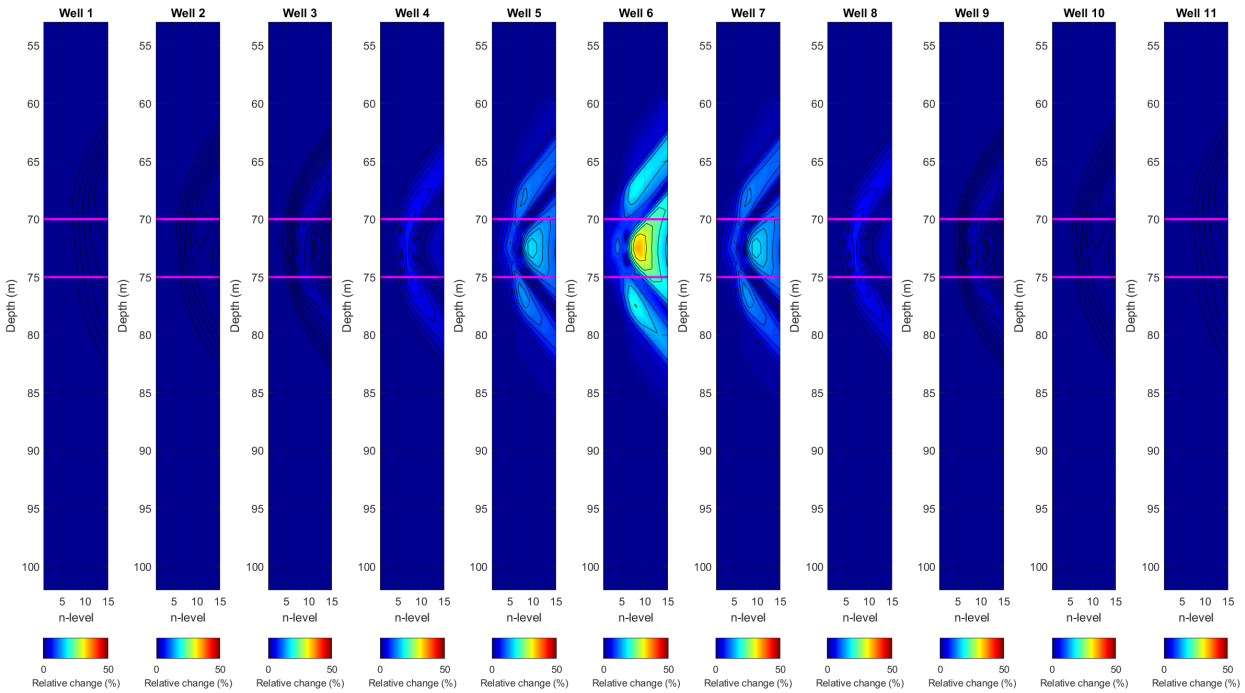

Figure 4.2.6: Simulated difference from the end of the experiment (10 min). The top and bottom of the aquifer are indicated by magenta lines.

4.2.1 Discussion of the raw data

The pseudosections in Figures 4.2.1 to 4.2.3 give an approximation of the distributions of resistivities adjacent to the boreholes that are being measured. Figure 4.2.7 presents and example of a single pseudosection from $t = 0$ *min*. In Figure 4.2.7, the high resistivities at low n-levels on the x-axis are due to the high resistivity of the freeze wall. At approximately n-level 5 on the x-axis, the apparent resistivities drop to much lower values and vertical variations in resistivity begin to appear. These vertical variations in resistivity are due to the variations in formation resistivities adjacent to the borehole. In this case, the lower resistivities centred at approimately 72.5 m depth are due to the saline aquifer. As the breach is simulated, changes in apparent resistivity should be expected to be centred on the basal aquifer.

In Figures 4.2.4 to 4.2.6, there are differences that are centred on the basal aquifer. This is illustrated in Figure 4.2.8. In Figure 4.2.8, the difference plots for well 6 at $t = 0,\ 5,\ 10,$ *and* 15 *min* are presented. In Figure 4.2.8 the difference increases as time progresses, and that difference is centred on the basal aquifer. The differences presented in Figure 4.2.8 indicate that at the breach location, there is a significant (25%) difference at $t = 5$ *min*, which means that a breach is detectable early during its progress. The hydraulic conductivities used for this simulation were very high; in a situation where the hydraulic conductivities are lower, the early stage detectibility of the breach will depend on the amount of noise.

To illustrate the effect of aquisition noise, the slides presented in Figures 4.2.1 and 4.2.4 are presented with 5% Gaussian noise added to the simulated survey data in Figures 4.2.9 and 4.2.10 respectively. Other sources of noise that were not included in this simulation include: geologic noise (ie. heterogenieties in the strata surrounding theboreholes); geometric noise (ie. borehole

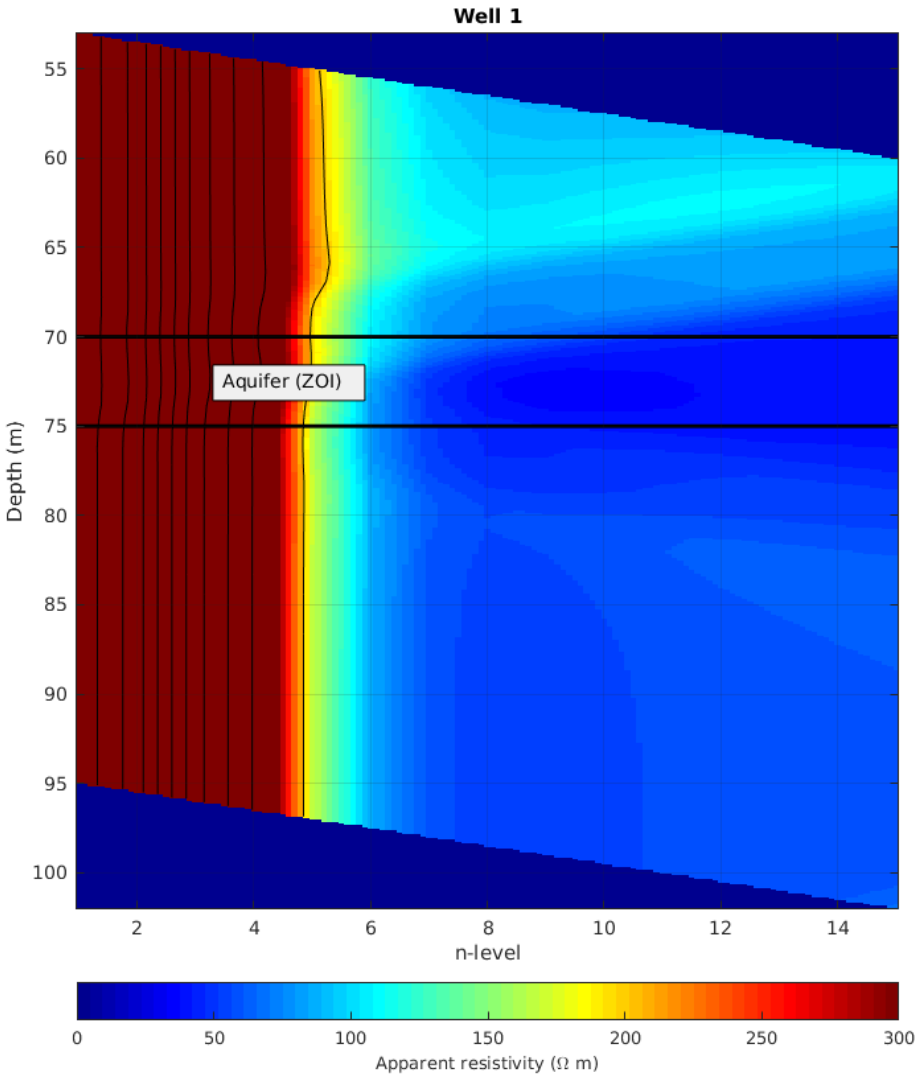

Figure 4.2.7: Simulated pseudosection for well 1 at t_0

deviations, or incorrect electrode locations); and stationary acquisition noise (ie. electrical noise from infrastructure). In Figure 4.2.10, the location of the breach is less clear than the case with no noise. The time elapsed between the beginning of the breach and when the breach is detectable will be limited by the severity of the aquisition noise.

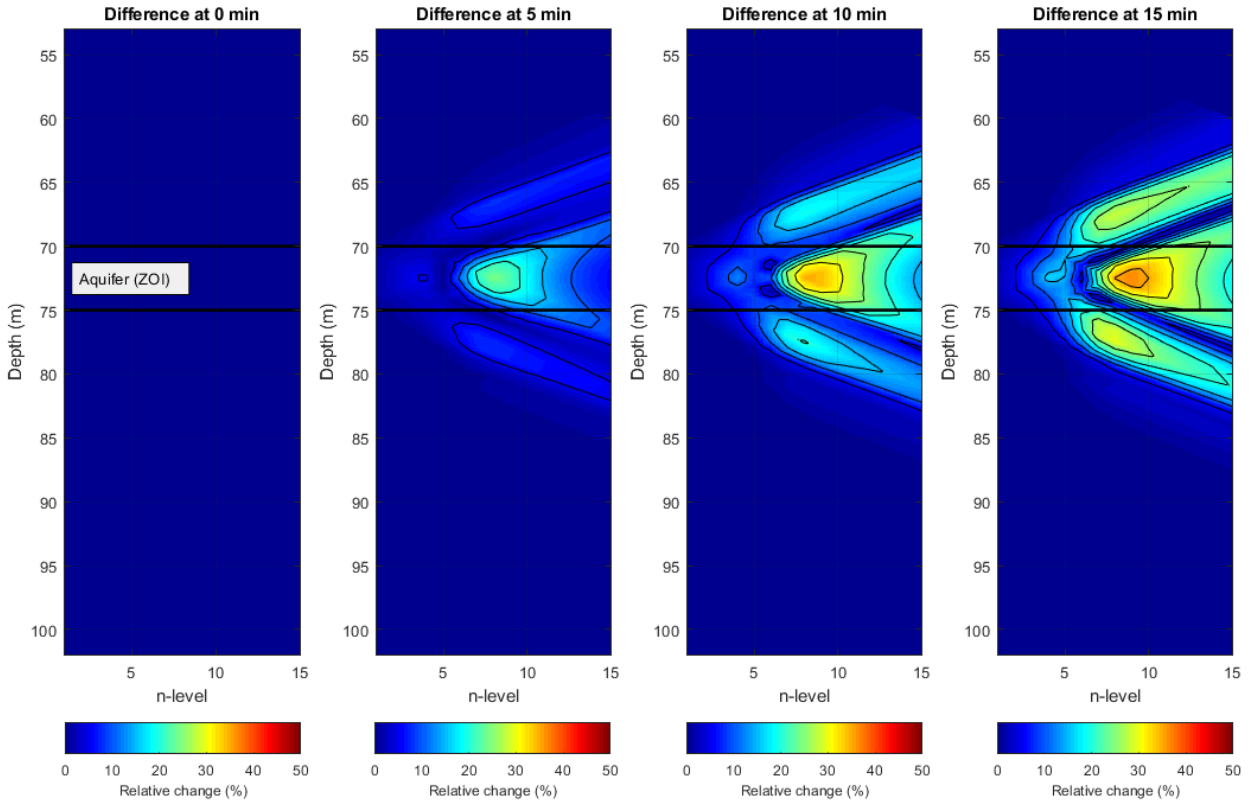

Figure 4.2.8: Simulated pseudosection differences at well 6 for $t = 0,\ 5,\ 10,$ *and* 15 *min. The top and bottom of the aquifer are indicated in black.*

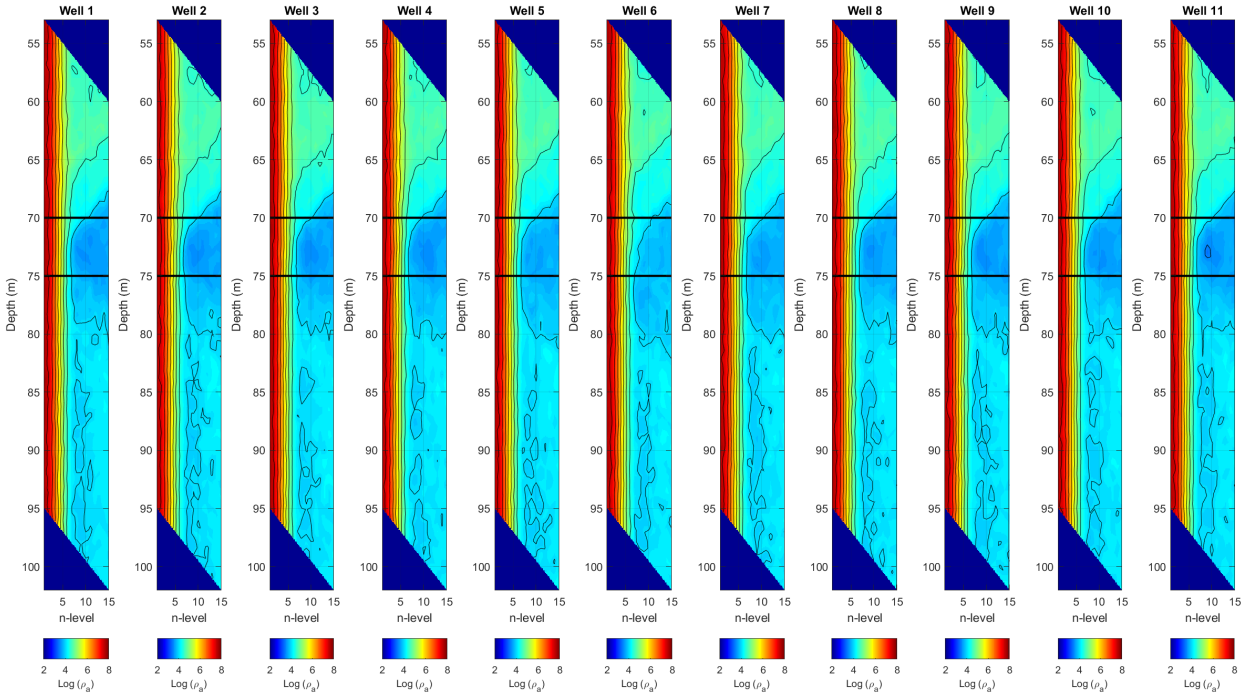

Figure 4.2.9: Simulated pseudosection with 5% noise for all wells at $t = 6$ min. The top and bottom of the aquifer are indicated in black.

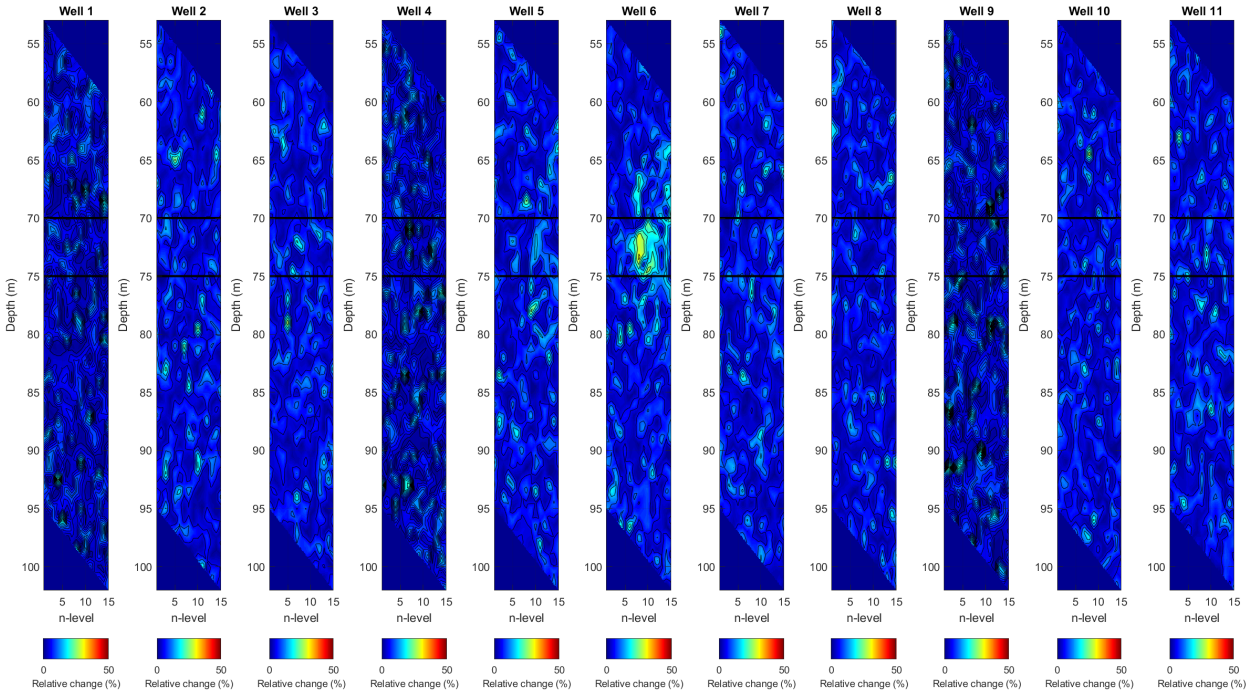

Figure 4.2.10: Simulated pseudosection differences with 5% noise for all wells at $t = 6$ min. The top and bottom of the aquifer are indicated in black.

On the basis of the raw data alone, it is possible to detect that there has been a breach, and it is possible to locate the breach laterally based on visual inspection using pseudosection plots of the raw data. The analysis of the raw data provides a great deal of information that the user needs to plan a remediation procedure (such as turning on the remediation freeze pipes) with very little computational effort. Figure 4.2.11 presents an example of a metric that can be used to indicate a change that requires a response. In Figure 4.2.11, the curves plotted are the L2 norms of the apparent resistivity pseudosections at 72.5 m depth, which is in the middle of the basal aquifer; the curves are from the 11 wells from the simulation, with well 6 being at the breach location. The curve for well 6 dips to the lowest value, which indicates that the breach is nearest to well 6. This can be used as an immediate response tool to detect the presence and location of a breach.

Although the breach location can be determined from the apparent resistivity pseudosections, the useful information is largely qualitative; no information can be obtained directly from the raw data that may indicate the quantity of contaminant that may have crossed the barrier. There may also be challenges in automating a remediation response on the basis of the raw data alone, as the differences spread out with radius.

For monitoring the freeze wall for a breach, a qualitative indication of where the breach is taking place and when it starts is the bulk of the information that is required for remediation, as this information can be used to initiate a reponse such as turning the freeze pipes back on in the affected area. Additional information, such as how much material has leaked across the wall, is nice to have for investigating the full impact of the breach, but may not be required to remediate the breach.

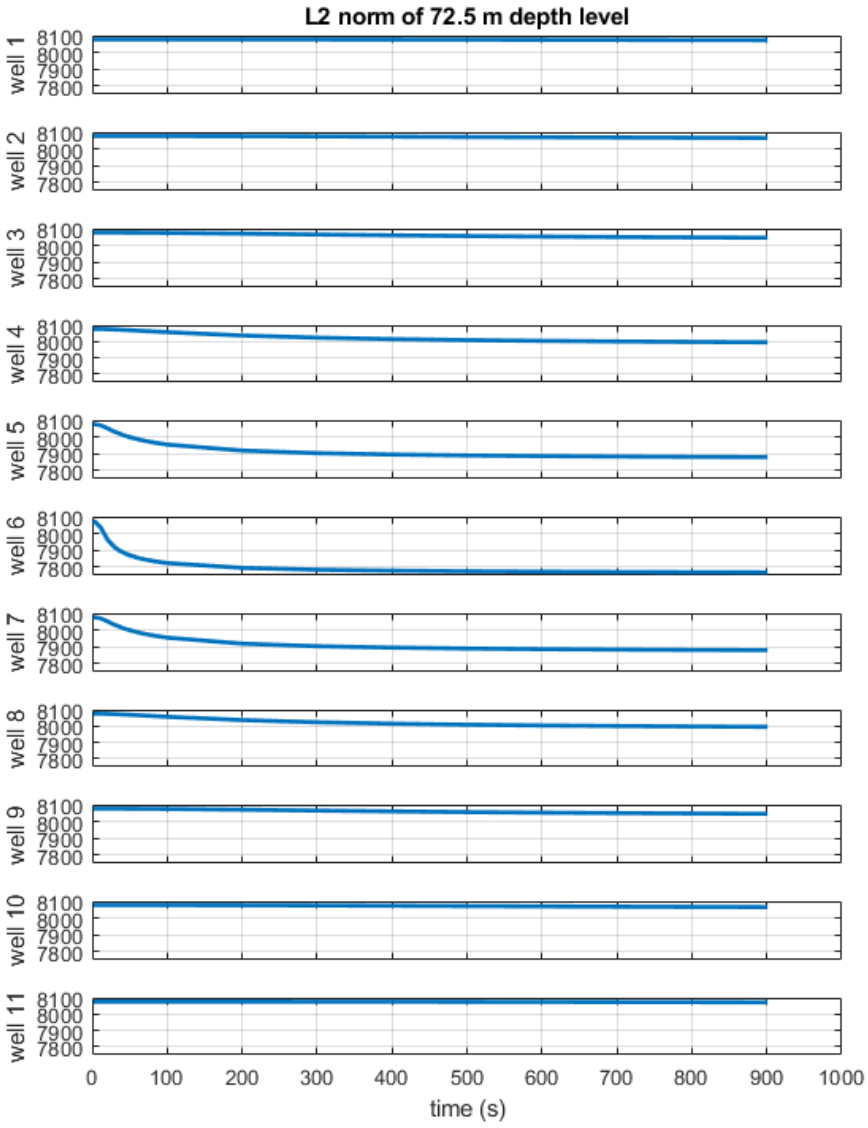

Figure 4.2.11: An illustration of the norm of the apparent resistivity values for a depth of 72.5 m throughout the experiment at the different wells. On the basis of this graph, it is possible to estimate that the breach is closest to well 6 as it shows the greatest impact.

4.3 Inversion of the simulation results

The inverted sections are presented as radial slices from the estimated cylindrical model with the hole being on the left side of each section at a radius of 0 m. At each time step, the sections for the 11 drillholes along the freeze wall are plotted as subplots of the same figure. Figures 4.3.1 to 4.3.3 presents examples of the inverted sections from $t = 2,\ 6,\ and\ 10\ min$ respectively. Figures 4.3.4 to 4.3.6 present examples of the differences between the inversion at $t = 0\ min$ and the inverted sections at $t = 2,\ 6,\ and\ 10\ min$ respectively.

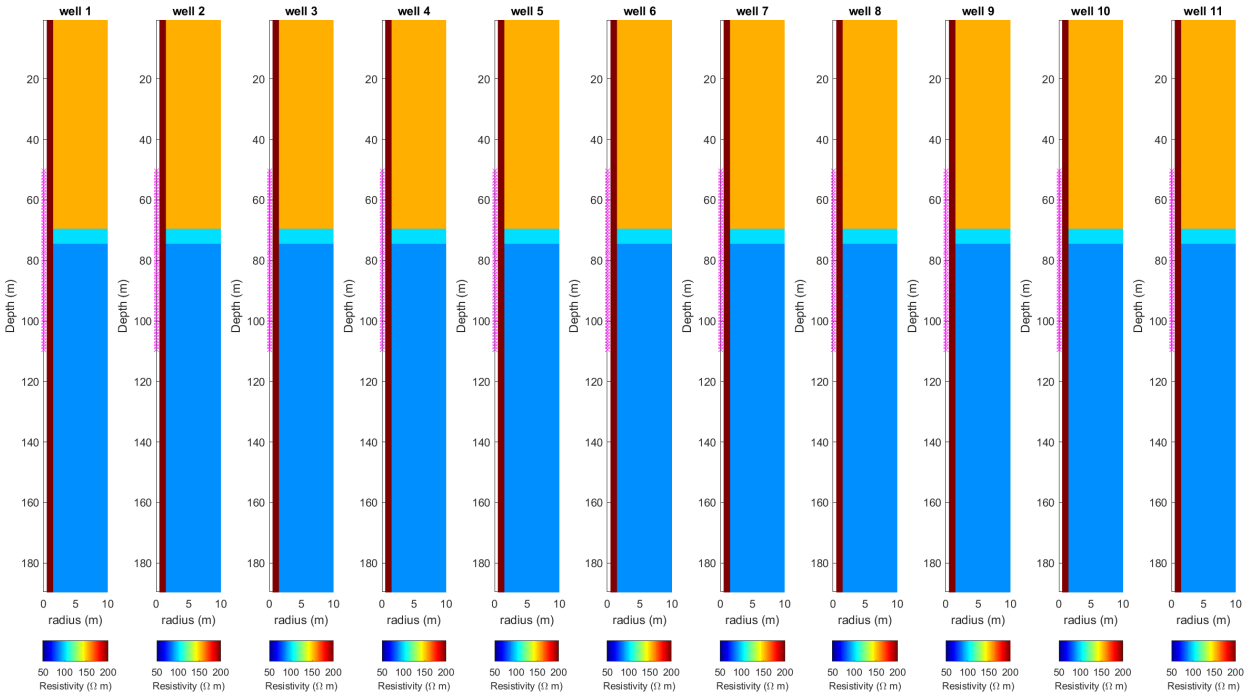

Figure 4.3.1: Inverted model from the beginning of the experiment (2 min). The electrode array is indicated in magenta.

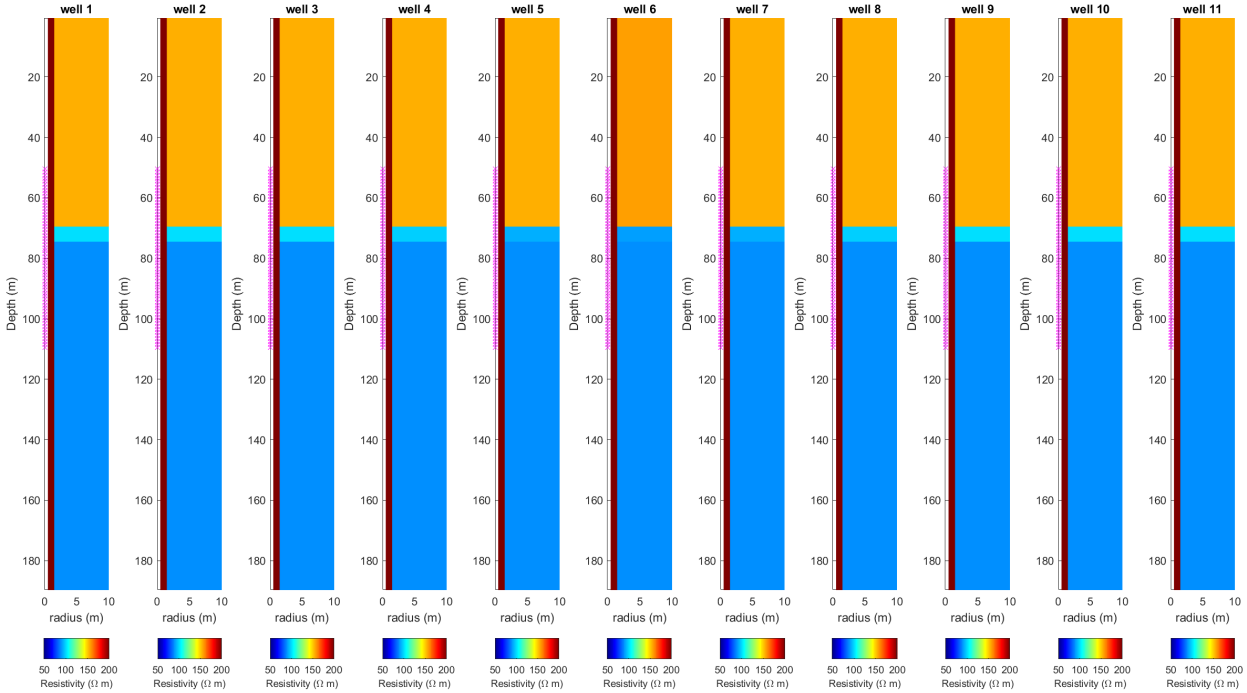

Figure 4.3.2: Inverted model from the middle of the experiment (6 min). The electrode array is indicated in magenta.

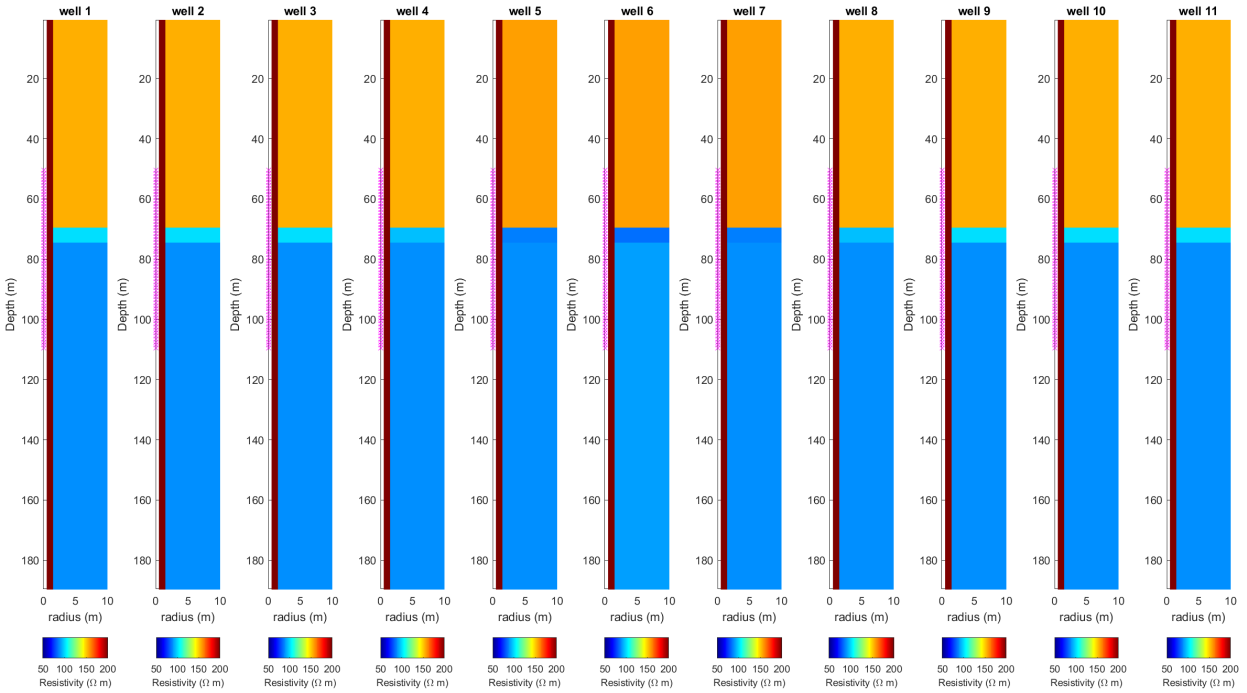

Figure 4.3.3: Inverted model from the end of the experiment (10 min). The electrode array is indicated in magenta.

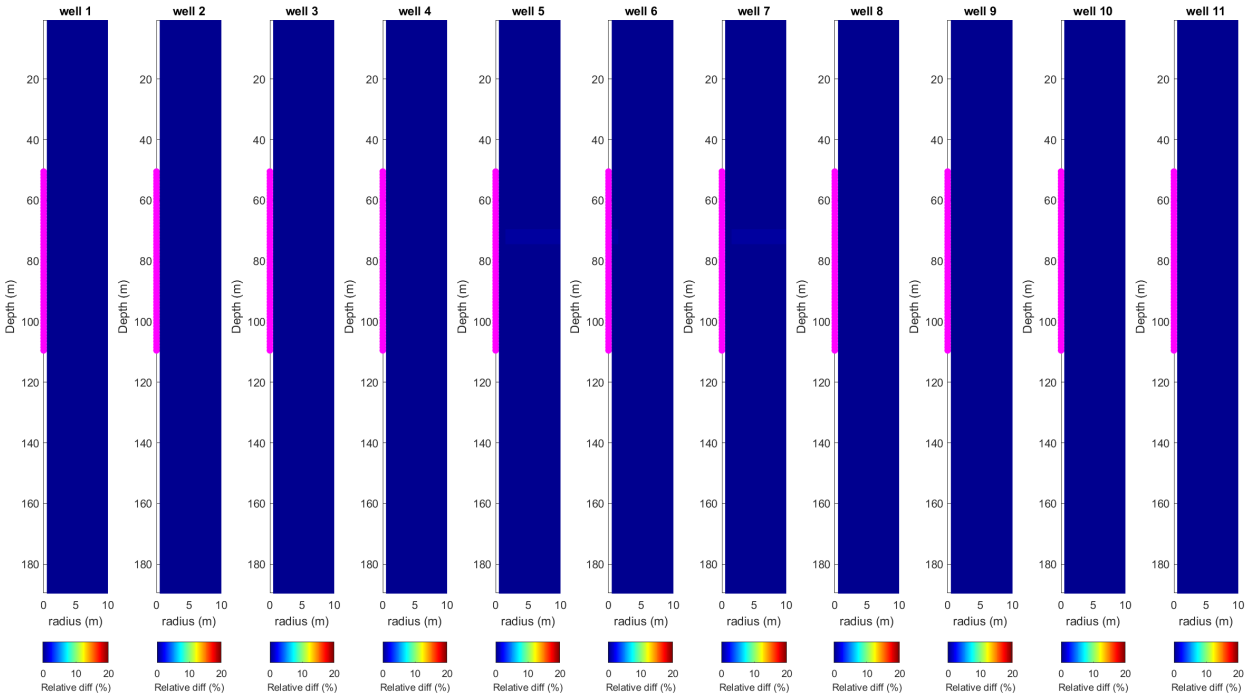

Figure 4.3.4: Inverted model difference from the beginning of the experiment (2 min). The electrode array is indicated in magenta.

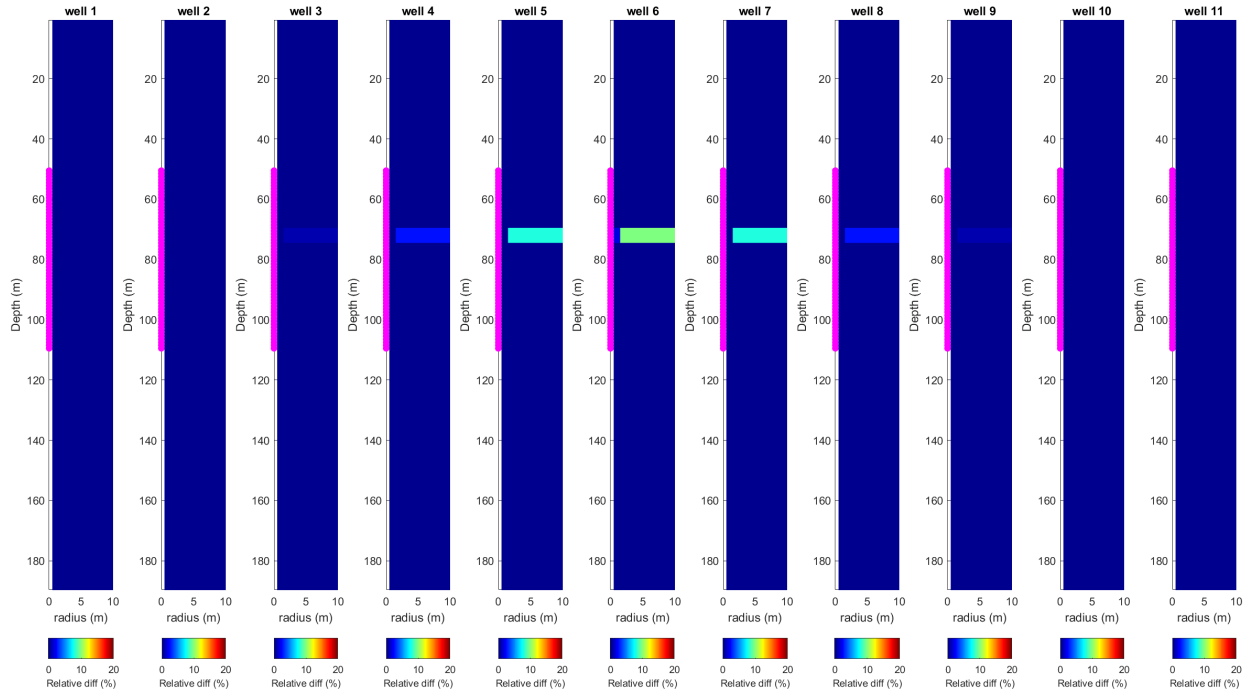

Figure 4.3.5: Inverted model difference from the middle of the experiment (6 min). The electrode array is indicated in magenta.

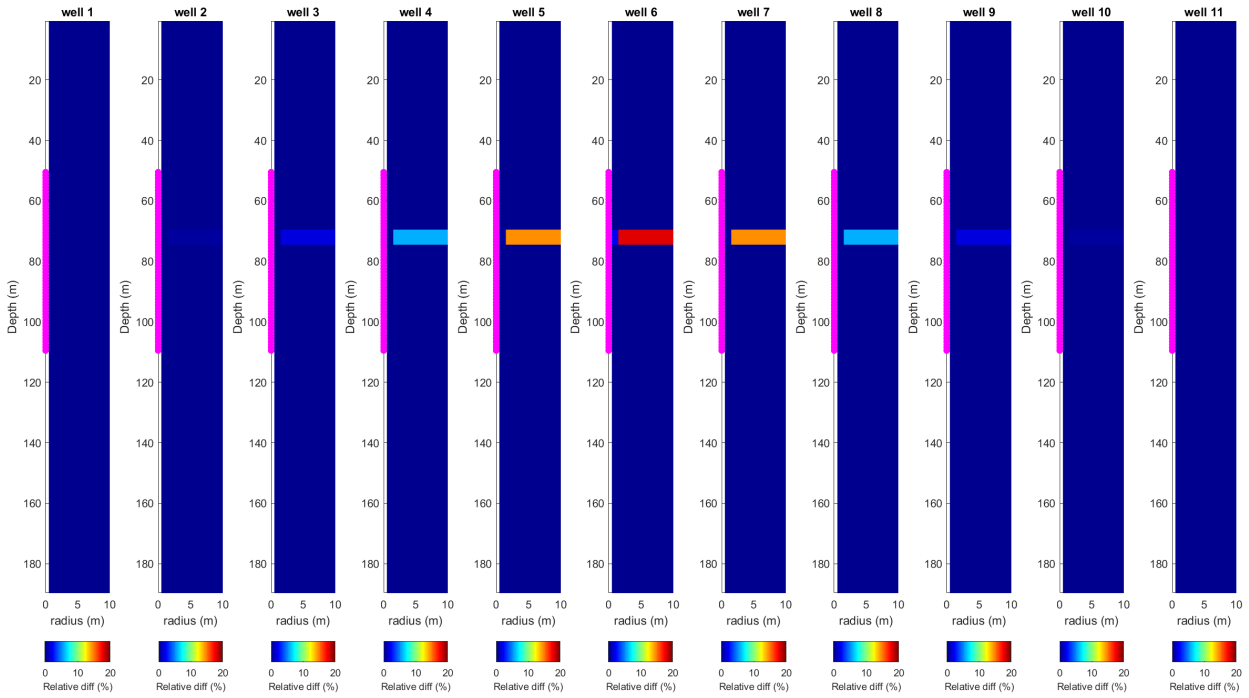

Figure 4.3.6: Inverted model difference from the end of the experiment (10 min). The electrode array is indicated in magenta.

4.3.1 Discussion of the inversion results

The inverted resistivity of the basal aquifer is a single value, which cannot represent the true resistivity value of the aquifer as it is not the same on both sides of the wall, nor is it the same at all distances from the wall for a given depth level. While it may not be possible to determine the true resistivity on the mine side of the freeze wall using the methods in this thesis, the relative changes in the inverted resistivity of the basal zone help to increase the precision of the location of the leak. In Figure 4.1.2, the stratigraphic section (ρ_f) is separated into three layers, as defined by the well tops and used in the inversion algorithm. The zone of interest (the basal aquifer) is the zone centred at approximately 70 m depth. Through the experiment (Figures 4.3.4 to 4.3.6), the inverted resistivity changes in the stratigraphic section are mainly in the zone of interest. This is illustrated in Figure 4.3.7. In Figure 4.3.7, the resistivities of the three layers throughout the course of the experiment are plotted in the upper three panels; in the lower three panels, the relative differences from the beginning of the experiment are plotted. The inversion results indicate that there are changes in all three layers. The apparent changes in the layers above and below the aquifer are due to residual error in the inversion process. These residual errors can be reduced, but there is a computational cost associated with the error reduction, and the benefit may be minimal. The relative change in the zone of interest (basal aquifer) is much larger than the relative change in the surrounding layers, indicating that the change is likely taking place in the basal aquifer, which in this case is true.

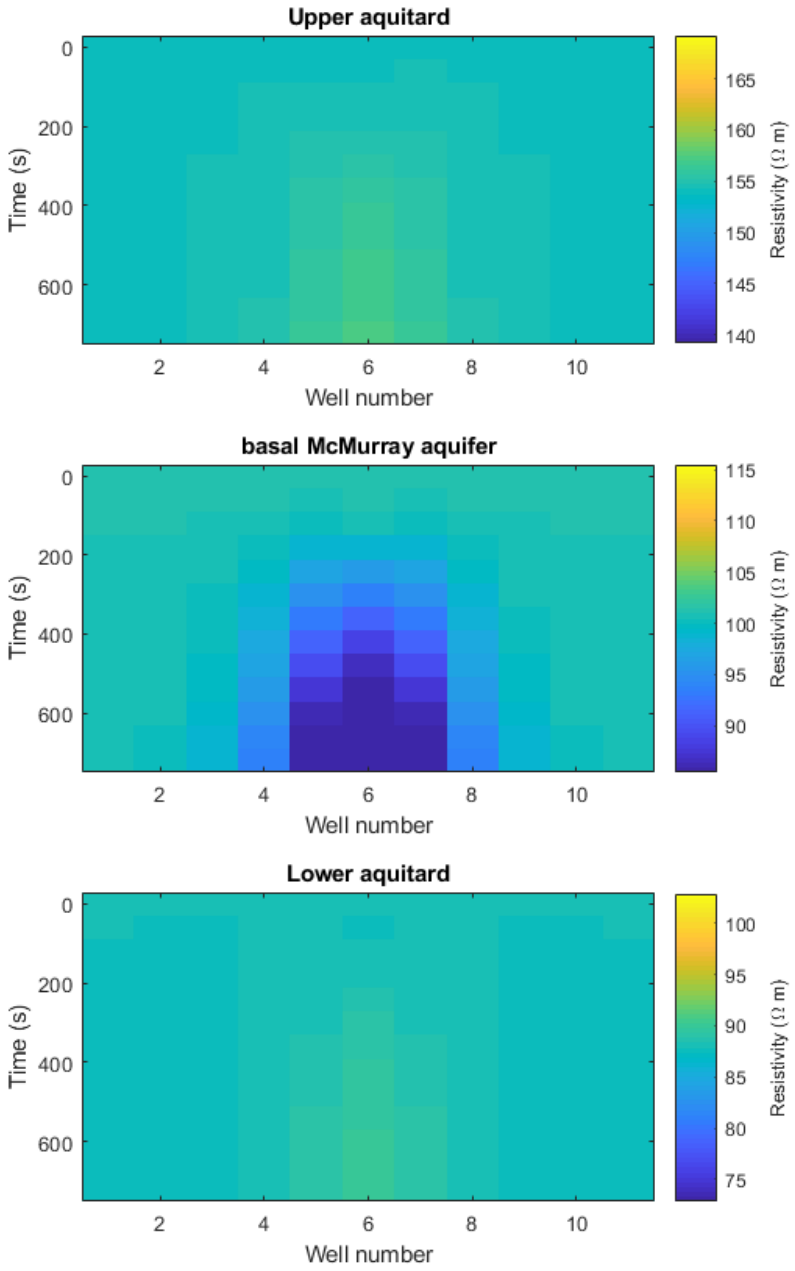

Figure 4.3.7: Inverted layer resistivities for the three model layers for each well (x-axis) and each time step (y-axis). The inverted resistivity values and differences clearly indicate that the leak is contained within layer 2.

Looking at the inverted resistivities along the wall over time similar to what is presented in Figure 4.3.7 allows the identification of the location of the leak. To identify the timing of the leak, it can be helpful to plot the formation resistivities from the well that is nearest to the leak over time; this is plotted in Figure 4.3.8. In Figure 4.3.8 the timing of the breach can be estimated to be fairly close to the true timing of the breach. In Figure 4.3.8 the initiation of the breach is plotted as a red line at t_0.

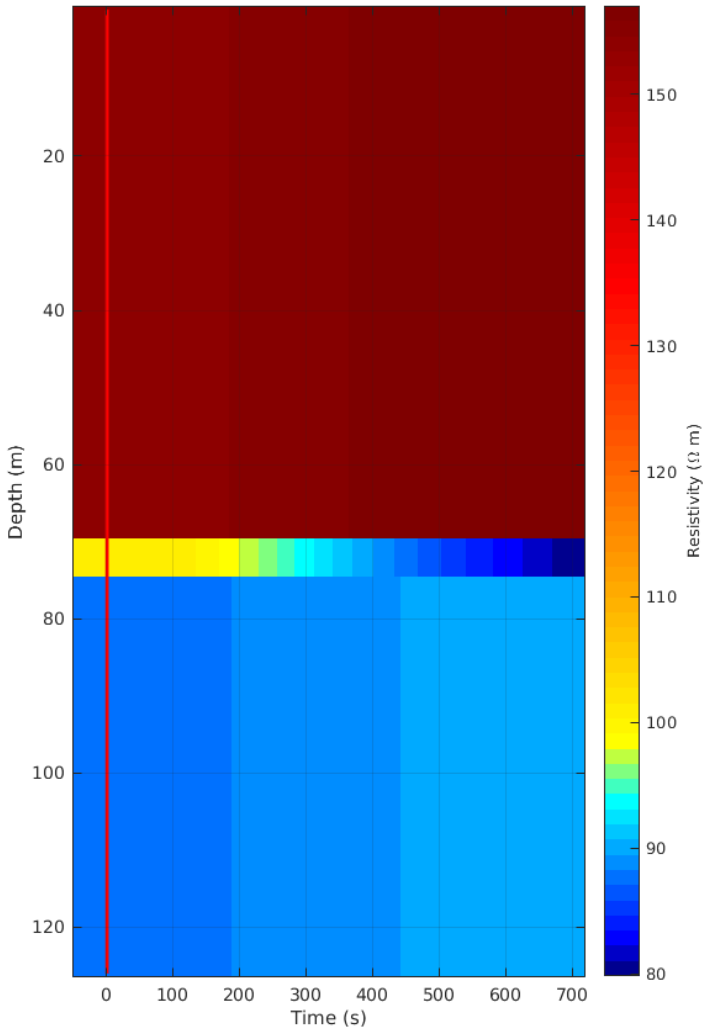

Figure 4.3.8: Estimated layer resistivities during the leak simulation for well 6 with no noise. The beginning of the leak is indicated by the red line.

To investigate the effect of noise on the inverted data, the simulation data were inverted with 5% gaussian noise added to the simulated potential differences. The inverted formation resistivities for the data with noise added are presented in Figure 4.3.9. In Figure 4.3.9, the noise has a significant impact on the inverted results. In the inversion of the noisy data, the breach location is still confined

to the zone of interest, but the lateral location of the breach is less clear.

Assuming that the location of the breach is known to be at well 6, the formation resistivities for well 6 during the course of the experiment are presented in Figure 4.3.10. In Figure 4.3.10 the timing of the initiation of the breach is not as clear as in the case with no noise, but can still be estimated in a similar time-frame. The estimated resistivities in each layer at well 6 with and without noise through the experiment are presented in Figure 4.3.11. In Figure 4.3.11 the inverted resistivities of the zone of interest with no noise shows a deflection of 4 Ωm between 120 and 180 seconds which may indicate a breach if it was known that there was little or no noise. The inverted resistivities of the zone of interest with noise shows a deflection of approximately 10 Ωm over the same 120 to 180 second window, which may also indicate a response. The resistivities of the layers above and below the zone of interest were not changed in the breach simulation but the estimated resistivities of these layers change a small amount. The 120 to 180 second window is a small time-frame to detect a wall breach, which in this case is due to the high hydraulic conductivities. If the aquifer hydraulic conductivities were higher, the time-frame for breach detection would also likely be higher.

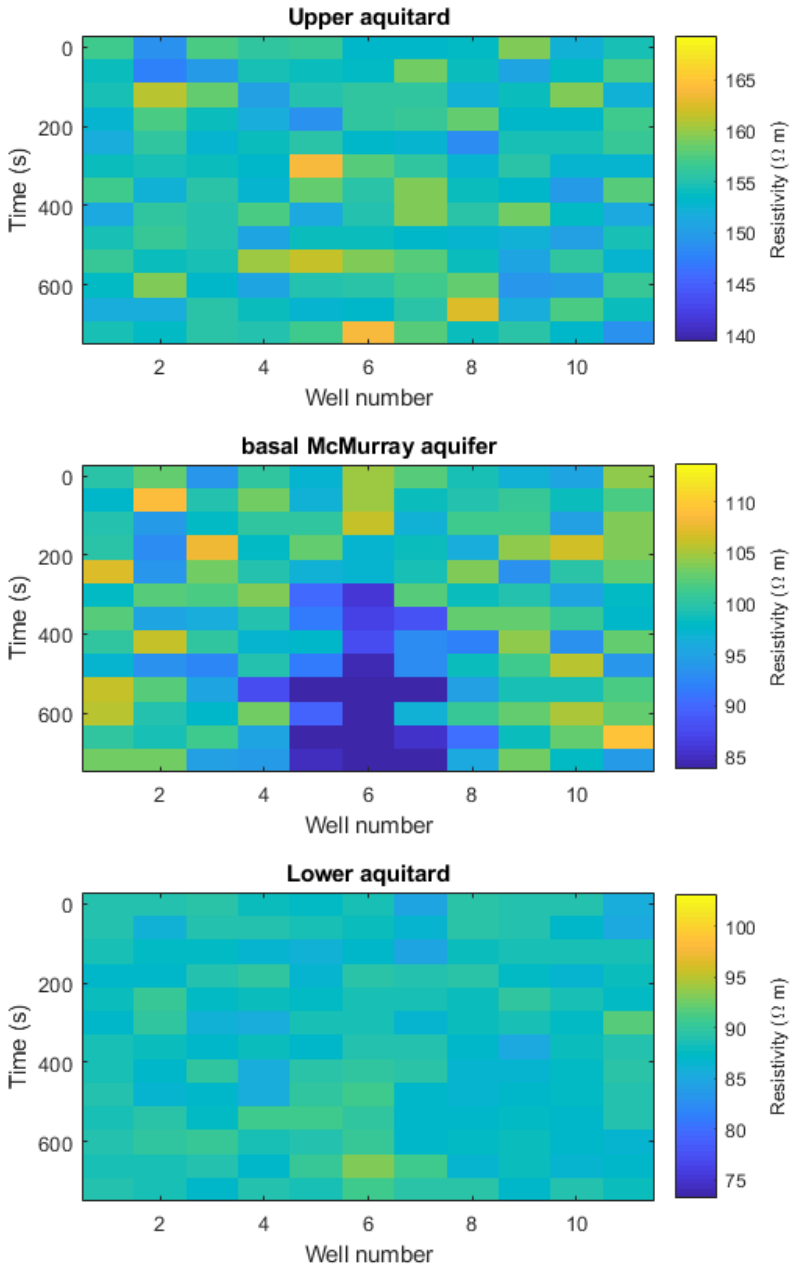

Figure 4.3.9: Inverted layer resistivities for the three model layers for each well (x-axis) and each time step (y-axis) for the case with 5 % added noise. The inverted resistivity values and differences clearly indicate that the leak is contained within layer 2.

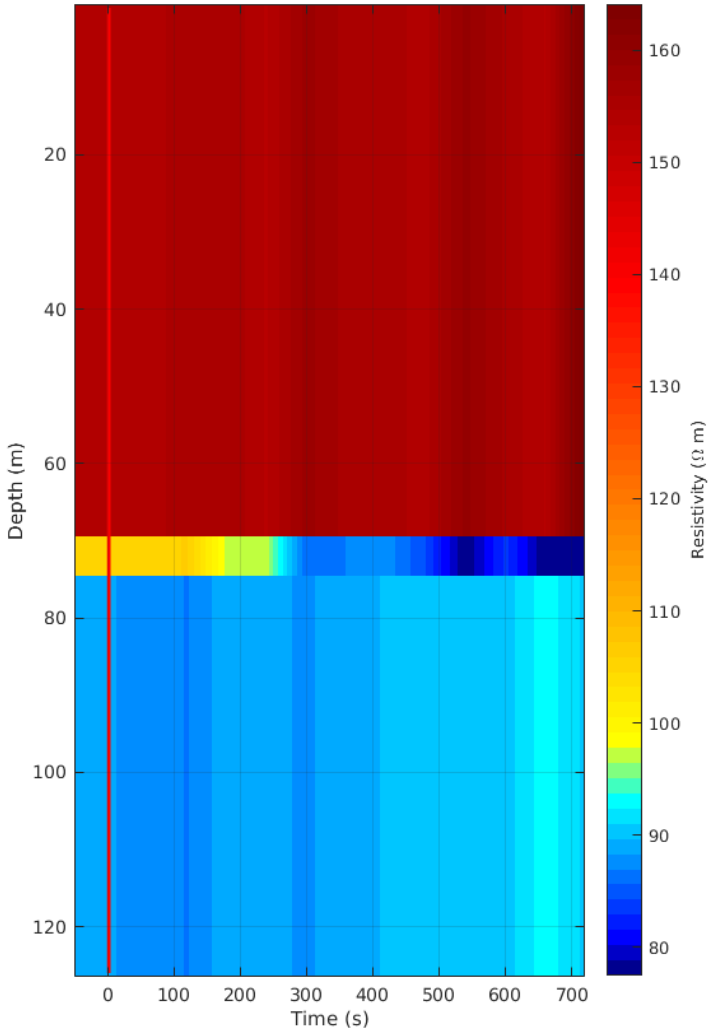

Figure 4.3.10: Estimated layer resistivities during the leak simulation for well 6 with 5 % added noise. The beginning of the leak is indicated by the red line.

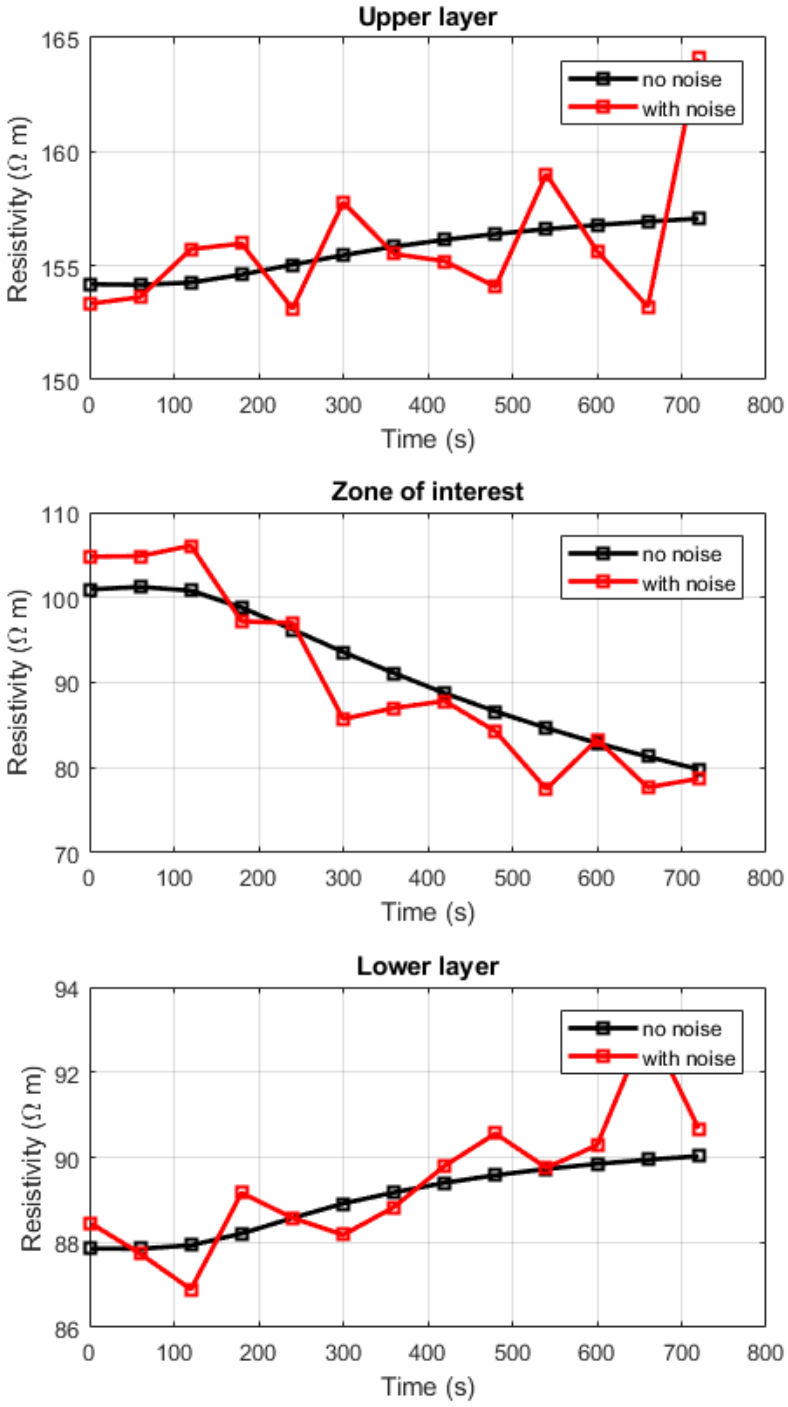

Figure 4.3.11: Estimated layer resistivities with and without noise

The results of the inversion of the simulated data demonstrate that the location and timing of the breach are clearly identified, even in the presence of 5% noise. While these results are more clear than the analysis of the raw data alone, they still offer the same basic information as the analysis of the raw data, at a computational cost. The added benefit of the inverted data may come if the system is used to automate a response, because of the fact that the location of the breach is more clearly identified in the inverted sections. Additional benefit of the inverted data is only likely to come from a quantitative analysis of the breach.

To gain a better understanding of the impact that noise has on how early the breach can be detected, an example simulation was run where there was no breach, but the 5% gaussian noise was added. The inverted layer resistivities for the example with no breach and 5% noise are presented in Figure 4.3.12. The inverted resistivities for well 6 for the example with no breach are presented in Figure 4.3.13. The resistivity values within the aquifer for the inverted sections with no breach but with 5% noise are presented in Figure 4.3.14. In Figure 4.3.14 the resistivity values range from 97 Ωm to 108 Ωm with a mean value at 101 Ωm and a standard deviation of 2 Ωm. This analysis allows us to estimate the required change in resistivity of the aquifer to trigger an alarm using risk analysis techniques similar to those used in geotechnical monitoring of retaining walls (Rainieri et al., 2013). The determination of a threshold for a change in resistivity that would require intervention would be based on a number of factors including: what is the cost associated with the remediation step, and by extension the cost of false alarms; what is the cost of an additional time-lag before detection; is there a point in a breach where the remediation step will no longer be effective? The analysis required for this determination is beyond the scope of this thesis, but it will need to be resolved for this monitoring technique to be used in practice.

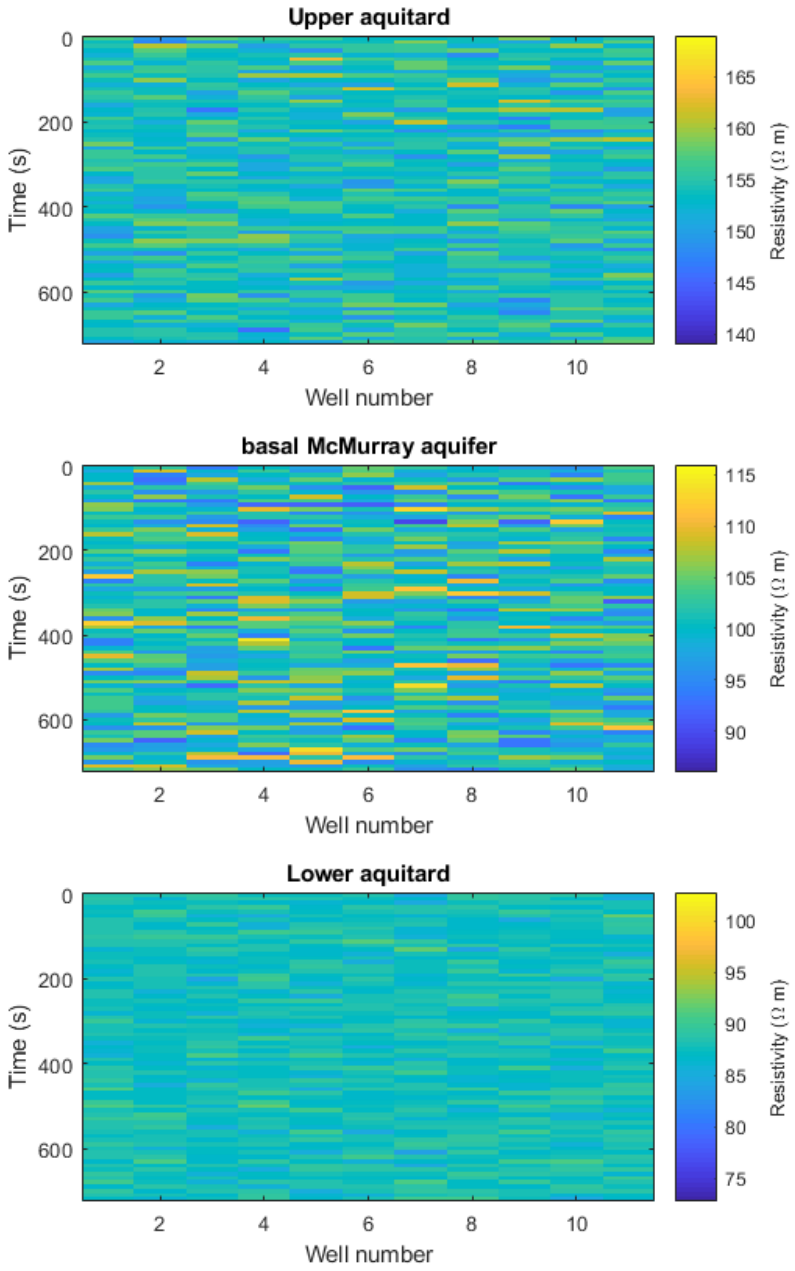

Figure 4.3.12: Inverted layer resistivities for the three model layers for each well (x-axis) and each time step (y-axis) for the case with no breach and 5 % noise.

To perform a quantitative analysis of the freeze wall breach will require a more accurate sim-

ulation to be run, or a lab-modelled breach. Even with a more appropriate breach simulation, the quantitative analysis of the breach using the cylindrical inversion algorithm is not trivial due to the fact that the cylinder centred at a borehole will be out of phase with a spherical breach at another location.

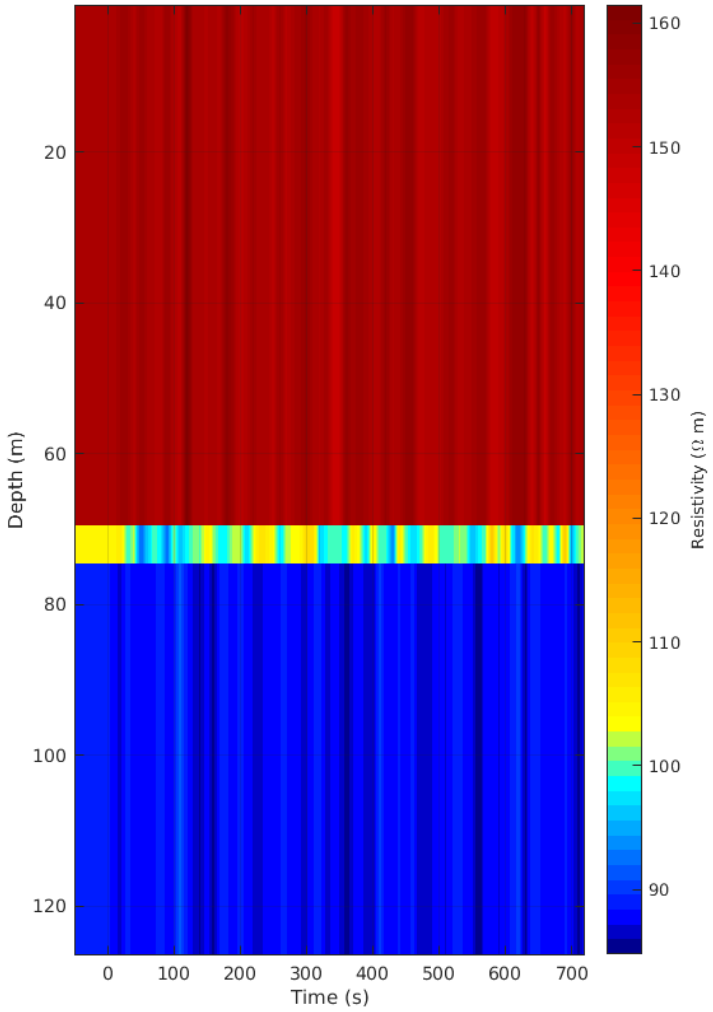

Figure 4.3.13: Inverted layer resistivities from well 6 for the case with no breach and 5 % noise. The data were simulated every 10 seconds for 720 seconds.

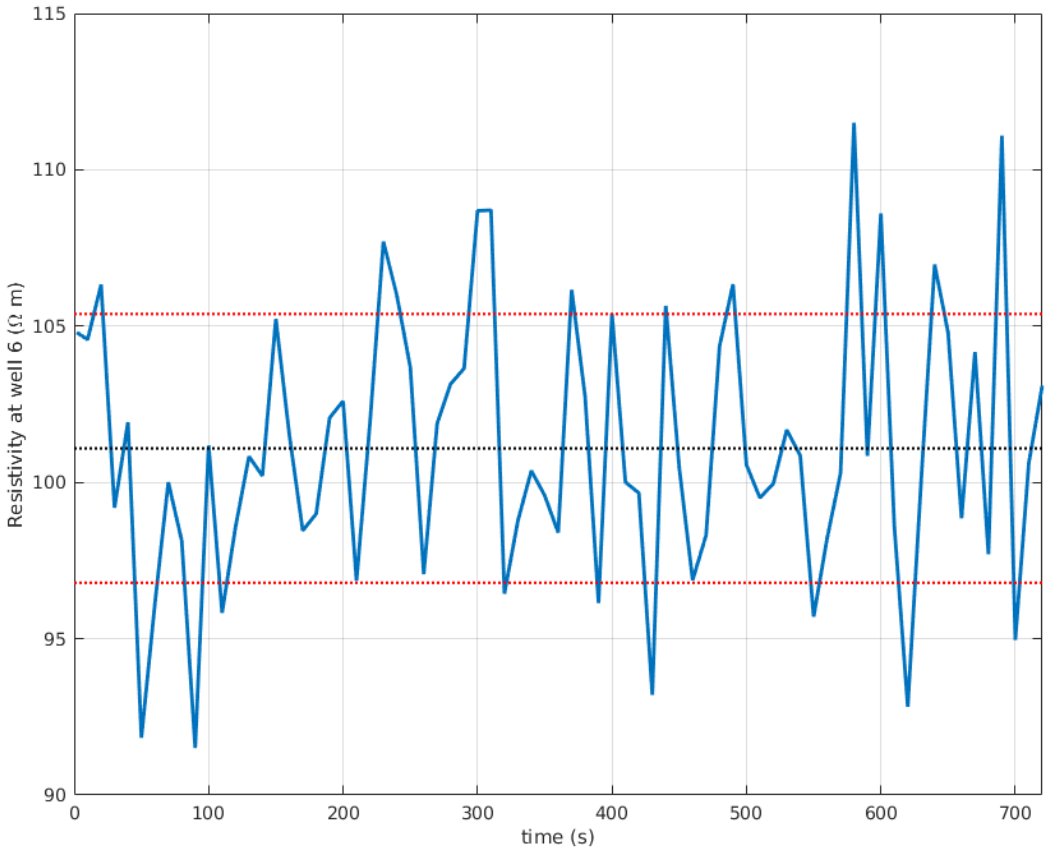

Figure 4.3.14: Inverted resistivity values from the zone of interest (aquifer) for well 6 with no breach and 5 % noise. Data for this chart were simulated every 10 seconds for 720 seconds. The mean value is 101.09 Ωm and is indicated by a black dashed line. The standard deviation is 4.29 Ωm and the mean value ± the standard deviation is indicated by red dashed lines

Chapter 5

Limitations of the current study

The monitoring approach described in this thesis represents a simplification of the ERT methods that are currently being used for monitoring the movement of saline water within the subsurface. For a monitoring that is on as large a scale as the freeze wall, a simplified approach allows the installation cost and computational cost to be reduced while still achieving the objectives of the survey. The simulation experiment in Chapter 4 showed that the approach has the potential to detect a leak at an early time and with a precision that is dependent mainly on the spacing of monitoring wells (proposed to be at the same spacing as the freeze wall installation wells). The timing of when the breach could be detected may depend on a number of factors that were not explored in this thesis including: the hydrogeolgic properties of the subsurface such as hydraulic conductivity, dispersion coefficient, chloride concentration difference, hydraulic head difference, and on the actual noise levels in the monitoring arrays. If this method were to be used to monitor a freeze wall these factors would need to be considered in order to understand the temporal precision with which this method could detect a leak.

The leak simulation example presented in this thesis showed a relatively quick saline water intrusion through the wall; the intrusion was several metres past the wall within 10 minutes of the initiation of the breach. In situations where the geophysical monitoring can be used to automatically initiate a response mechanism to correct the leak, the lag time between the survey and the imaging results is important.

From a qualitative point of view, the leak in the simulation could be detected on the basis of an

inspection of the raw-data pseudosections, which requires very little computation after each time. In a simple monitoring scenario, where an operator were inspecting the time-snapshots for leaks and then manually initiating an intervention procedure in the case of a leak, it may be acceptable to simply base the monitoring on an analysis of the raw data.

If a more sophisticated monitoring solution involving an automated response to a leak were to be implemented, inversion of the raw data may be necessary. The inverted models from each well, as shown by the simulation, can narrow the resistivity changes down to the stratigraphic layer of interest. In the simulation performed for this thesis, there is a discrepancy between the resistivities that were simulated and those that were inverted, which is due to a number of factors including: a discretization error in the Cartesian model; and the simplified cylindrical parameterization. The discrepancy in the absolute resistivities for this simulation is not critical because for monitoring, what we are trying to detect is a change, rather than the true resistivities. The magnitudes of the absolute resistivities are comparable, so the absolute values are not as important as the relative changes. The inverted models clearly indicated the timing and location of the leak to within a small window (< 200 s). The single-value resistivity for the basal aquifer in each well provides a way to easily integrate the results into an automatic response system to remediate the wall in the case of a leak.

With all geophysical methods there is always a cost to additional imaging efforts. By increasing the effort put into imaging the subsurface, it is generally always possible to obtain a more refined image. In reality, there is a practical limit to the imaging effort. In some cases cost is a limiting factor; increasing the cost of geophysical imaging can make alternative ways of obtaining the subsurface information more attractive than the geophysical method. In other cases time can be a limiting factor; the time required to reach a certain level of imaging can exceed a critical time

period for which action must be taken. The imaging effort for the objectives in this thesis are limited by a combination of cost and time.

There are methods using combinations of surface to borehole and cross-borehole ERT to image the wall in 3-D, which would give a more thorough image of the area surrounding the freeze wall, but these methods require a far more intrusive setup; many additional boreholes would be required to install the necessary electrode arrays, and this additional cost may be impractical for such a project to support. The setup described in this thesis does not provide the same level of imaging as a 3-D survey would, but at a fraction of the cost, it is effective at addressing the objective of the monitoring project: is the wall leaking?

5.1 Discussion of next steps

Throughout this thesis there have been a number of items that require additionial research to resolve that are beyond the scope of this thesis. These items include: investigating an appropriate technique for comparing the results of forward ERT models using different discretization schemes (Cartesian vs cylindrical); determining an appropriate approximation method for including the wall into the cyclindrical parameterization; investigating methods of using multiple single-borehole ERT datasets along the wall to quantify the amount of contaminant that has leaked through the wall; and determining an appropriate monitoring and response scheme that can optimize the number of false alarms created by an automatic monitoring system with the risk due to a delay in leak detection.

One potential method that may simplify the approach even further, while helping to avoid some of the problems due to simplification that have been described in this thesis would be to use

machine learning techniques to quantify the leak location and the amount of saline water that has leaked directly from the raw data. This may be achievable in this particular case because of the high level of model control in this environment, which will allow for a finite training dataset to be simulated to train the algorithm. This approach would preclude the need for inversion altogether and could be integrated seamlessly into an automatic response system.

Chapter 6

Conclusions

This thesis examined the problem of monitoring a freeze wall that is used to isolate a saline aquifer from a mine pit using electrical resistivity tomography. The problem of monitoring the freeze wall using geophysical techniques is difficult because of the scale of such a project, and the results herin demonstrated that this difficulty may be mitigated by taking a simplified approach to monitoring by using a series of single-borehole ERT measurements.

The simulation was aimed at answering the following questions:

1. Can the method detect a breach in the freeze wall?

2. Can the method quantify the amount of contaminant that leaks across the wall in the case of a breach?

To test this, a breach in the freeze wall was simulated and a series of monitoring wells were used to try to detect the breach. The results of the simulation indicated that the breach can be detected very early in the breach progress by a simple inspection of the raw data pseudosections, although the usefulness of the raw data pseudosections is limited because they require interpretation by an operator. A simplified cylindrical parametric inversion of the raw data provides a quantity for the zone of interest that can be acted upon automatically and may be more useful than an inspection of the raw data.

The simplified inversion, while computationally efficient, was not suitable to quantify the amount of contaminant that leaks across the wall, which is due to the simplified parameteriza-

tion used in the inversion. The second objective of quantifying the contaminant leak is one that would require a more computationally intense inversion algorithm or a different strategy.

On the basis of the results of the experiment, the main conclusion that can be made is that in this case, the simplified geophysical analysis may not provide a detailed map of the physical properties in the survey domain, but it can provide the necessary information that is required to detect the problem and mitigate it, which is the critical goal for this type of monitoring.

Bibliography

Archie, G. (1942). The Electrical Resistivity Log as an Aid in Determining Some Reservoir Characteristics. *Transactions of the AIME*, 146(01):54–62.

Awolusi, F., Fasesan, O., Adisoemarta, P., and Heinze, L. R. (2005). Analysis of Errors in Historical Use of Archie' s Parameters. In *Canadian International Petroleum Conference*, number 2.

Azar, J. H., Javaherian, A., Pishvaie, M. R., and Nabi-Bidhendi, M. (2008). An approach to defining tortuosity and cementation factor in carbonate reservoir rocks. *Journal of Petroleum Science and Engineering*, 60(2):125–131.

Banin, A. and Anderson, M. D. (1974). Effects of Salt Concentration Changes During Freezing on the Unfrozen Water Content of Porous Materials. *Water Resources Research*, 10(1):124–128.

Bergmann, P., Schmidt-Hattenberger, C., Kiessling, D., Rücker, C., Labitzke, T., Henninges, J., Baumann, G., and Schütt, H. (2012). Surface-downhole electrical resistivity tomography applied to monitoring of CO 2 storage at Ketzin, Germany. *Geophysics*, 77(6):B253—-B267.

Binley, A., Henry-Poulter, S., and Shaw, B. (1996). Examination of solute transport in an undisturbed soil column using electrical resistance tomography. *Water Resources Research*, 32(4):763–769.

Broughton, P. L. (2013). Devonian salt dissolution-collapse breccias flooring the Cretaceous Athabasca oil sands deposit and development of lower McMurray Formation sinkholes, northern Alberta Basin, Western Canada. *Sedimentary Geology*, 283:57–82.

Campanella, R. and Weemees, I. (1990). Development and use of an electrical resistivity cone for Groundwater contamination studies. *Canadian Geotechnical Journal*, 27:557–567.

Chambers, J. E., Wilkinson, P. B., Gunn, D. A., Ogilvy, R. D., Pearson, S. G., Kuras, O., Meldrum, P. I., Ghataora, G., and Burrow, M. (2007). Geoelectrical monitoring of seasonal moisture content changes in an earth embankment. *Near Surface*, (September 2007):3–5.

Chen, H., C. and Fang, J., H. (2011). Sensitivity Analysis of the Parameters in Archie's Water Saturation Equation. *The Log Analyst*, 239:39–44.

Commer, M., Doetsch, J., Dafflon, B., Wu, Y., Daley, T. M., and Hubbard, S. S. (2016). Time-lapse 3-D electrical resistance tomography inversion for crosswell monitoring of dissolved and supercritical CO2 flow at two field sites: Escatawpa and Cranfield, Mississippi, USA. *International Journal of Greenhouse Gas Control*, 49:297–311.

Crain, E. (1974). Crain's Petrophysical Handbook.

Daily, W. (1991). Cross-borehole resistivity tomography. *Geophysics*, 56(8):1228.

Daily, W. and Owen, E. (1991). Cross-borehole resistivity tomography. *Geophysics*, 56(8):1228–1235.

Daily, W. and Ramirez, A. L. (2000). Electrical imaging of engineered hydraulic barriers. *Geophysics*, 65(1):83.

Dillon, H., B. and Andersland, O., B. (1966). Predicting Unfrozen Water Contents in Frozen Soils. *Canadian Geotechnical Journal*, 111(2).

Dines, K. A. and Lytle, R. J. (1979). Computerized Geophysical Tomography. *Proceedings of the IEEE*, 67(7):1065–1073.

Donovan, J. (2011). Shell set to plug leak that created pond at oilsands mine.

Duriez, S. (2005). *On the Use of Groundwater Contaminant Transport Modelling in Risk Assessments*. PhD thesis, Chalmers University of Technology.

Feng, D. S., Dai, Q. W., and Xiao, B. (2014). Contrast between 2D inversion and 3D inversion based on 2D high-density resistivity data. *Transactions of Nonferrous Metals Society of China (English Edition)*, 24(1):224–232.

Flathe, H. (1954). Possibilities and limitations in applying geoelectrical methods to hydrogeological problems in the coastal areas of northwest Germany. In *European Association of Exploration Geophysicists*.

Fox, R. (1830a). On the Electro-Magnetic Properties of Metalliferous Veins in the Mines of Cornwall. *Philosophical Transactions of the Royal Society of London*, 120(1830):399–414.

Fox, R. (1830b). On the Electro-Magnetic Properties of Metalliferous Veins in the Mines of Cornwall. *Royal Society*, 120:399–414.

Fox, R. (1838). Report on some experiments on the electricity of metallic veins and the temperature of mines. *British Association for the Advancement of Science*, 6:133–137.

Fox, R. (1843). Notice of some experiments on subterranean electricity made in Pennance mine, near Falmouth. *Philosophical Magazine Series 3*, 23(155):491–496.

Friedel, S., Maurer, H., Herfort, M., and Van Meir, N. (2004). Application of single-hole geoelectrical tomography to characterize a coastal aquifer. In *SEG International Exposition and 74th Annual Meeting*, number October, pages 1–4.

Government of Alberta (2017). Oil Sands: Facts and Stats.

Hackbarth, D. (1980). The Athabasca Oil Sands. *Canadian Geotechnical Journal*, 17:131–136.

Hallenbach, F. (1952). Geo-electrical problems of the hydrology of west German areas. In *European Association of Exploration Geophysicists*.

Hamada, G., Assal, M., and Ali, M. (1995). Improved Technique to Determine Archie's Parameters and Consequent Impact on the Exactness of Hydrocarbon Saturation Values. In *First Joint Symposium of the CSPG and the Canadian Well Logging Society (CWLS)*, page 222.

Hamada, G. M. (2010). Analysis of Archie's parameters determination techniques. *Petroleum Science and Technology*, 28(1):79–92.

Hayley, K., Bentley, L. R., and Gharibi, M. (2009). Time-lapse electrical resistivity monitoring of salt-affected soil and groundwater. *Water Resources Research*, 45(7):1–14.

Inman, J., Ryu, J., and Ward, S. (1973). Resistivity inversion. *Geophysics*, 38(6):1088–1108.

Inman, J. R. (1975). Resistivity Inversion With Ridge Regression. *Geophysics*, 40(5):798.

Jo, H. R. and Ha, C. G. (2013). Basal water-bearing zone of the oil-sands deposits of the Cretaceous McMurray Formation at Christina Lake, Alberta, Canada. *Geosciences Journal*, 17(4):445–453.

Krulc, Z. and Mladenović, M. (1969). The application of geoelectrical methods to ground-water exploration of unconsolidated formations in semi-arid areas. *Geoexploration*, 7(2):83–95.

LaBrecque, D. J. (1996). The effects of noise on Occam's inversion of resistivity tomography data. *Geophysics*, 61(2):538.

LaBrecque, D. J. and Ward, S. (1988). Two-dimensional inversion of cross-borehole resistivity using multiple boundaries. In *58th Annual International SEG meeting*.

Loke, D. M. (1999). Electrical imaging surveys for environmental and engineering studies. Technical Report 1999.

Mahood, R., Verhoef, M., and Stoakes, F. A. (2012). Paleozoic Stratigraphic Framework beneath the Muskeg River Mine (Twp 95 , Rge 9 - 10W4): Controls and Constraints on Present. In *Geoconvention 2012: Vision*, pages 1–8.

Marquardt, D. (1963). An Algorithm for Least-Squares Estimation of Nonlinear Parameters. *Journal of the Society for Industrial and Applied Mathematics*, 11(2):431–441.

Maute, R., Lyle, W., and Sprunt, E. (1992). Improved Data-Analysis Method Determines Archie Parameters From Core Data (includes associated paper 24964). *Journal of Petroleum Technology*, 44(1):103–107.

McGinnis, L., Nakai, K., and Clark, C. (1973). Geophysical identification of frozen and unfrozen ground, Antarctica. *Permafrost*, pages 136–146.

Meligonitis, R., Galanopoulos, D., Hasiotis, T., and Velegrakis, A. (2016). Geo-electrical mapping of bedrock in Vatera Beach, Lesvos. In *Proceedings of the 14th International Congress of the Geological Society of Greece, Thessaloniki*, volume L, pages 2323–2331.

Nimmer, R. E., Osiensky, J. L., Binley, A. M., and Williams, B. C. (2008). Three-dimensional

effects causing artifacts in two-dimensional, cross-borehole, electrical imaging. *Journal of Hydrology*, 359(1-2):59–70.

Pekeris, C. L. (1940). Direct method of interpretation in resistivity prospecting. *Geophysics*, 5:31–42.

Pelton, W. H., Rijo, L., and Swift, C. (1978). Inversion of Two-Dimensional Resistivity and Induced-Polarization Data. *Geophysics*, 43(4):788.

Perri, M. T., Cassiani, G., Gervasio, I., Deiana, R., and Binley, A. (2012). A saline tracer test monitored via both surface and cross-borehole electrical resistivity tomography: Comparison of time-lapse results. *Journal of Applied Geophysics*, 79:6–16.

Picotti, S., Gei, D., Carcione, J. M., Grünhut, V., and Osella, A. (2013). Sensitivity analysis from single-well ERT simulations to image CO 2 migrations along wellbores. *The Leading Edge*, 32(2010):504–512.

Pidlisecky, A., Cockett, R., and Knight, R. (2013). Electrical Conductivity Probes for Studying Vadose Zone Processes: Advances in Data Acquisition and Analysis. *Vadose Zone Journal*, 12(1):1–12.

Pidlisecky, A. and Knight, R. (2008). FW2_5D: A MATLAB 2.5-D electrical resistivity modeling code. *Computers and Geosciences*, 34(12):1645–1654.

Rainieri, C., Fabbrocino, G., and De Magistris, F. S. (2013). An integrated seismic monitoring system for a full-scale embedded retaining wall. *Geotechnical Testing Journal*, 36(1):40–53.

Schima, S., LaBrecque, D., and Lundegard, P. (1996). Monitoring Air Sparging Using Resistivity Tomography. *Groundwater Monitoring and Remediation*.

Schlumberger, C. (1920a). Essais de Prospection Electrique du Sous-sol. *Acad. Sci. Comptes Rendus*, 170(9):519–521.

Schlumberger, C. (1920b). Etude de la prospection electrique du sous-sol. *Engineering Mining Journal*, 111:782–788.

Schlumberger, C. (1927). Prospection electrique par les procedes Schlumberger. Technical report.

Schlumberger, C. and Schlumberger, M. (1928). Decouverte pres de Hettenschlag d'un deuxieme dome de sel sous la plaine d'Alsace. *Acad. Sci. Comptes Rendus*, 186(7):445–446.

Schlumberger, C. and Schlumberger, M. (1930a). Depth of investigation attainable by potential methods of electrical exploration. *American Institute of Mining and Metallurgical Engineers*, 315:3–9.

Schlumberger, C. and Schlumberger, M. (1930b). Electrical studies of the earth's crust at great depths. *American Institute of Mining and Metallurgical Engineers*, 97:134–140.

Schlumberger, C. and Schlumberger, M. (1935). La prospection electrique du bassin salifere d'Alsace. *International Mines Congress*, 2:855–864.

Schlumberger, C., Schlumberger, M., and Leonardon, E. (1932). Electrical Coring; a Method of Determining Bottom-hole Data by Electrical Measurements. Technical Report 01.

Schlumberger, C., Schlumberger, M., and Leonardon, E. (1933). A new contribution to subsurface

studies by means of electrical measurements in drill holes. *American Institute of Mining and Metallurgical Engineers*, 110:273–289.

Schmall, P. and Maishman, D. (2007). Ground freezing a proven technology in mine shaft sinking. *Tunneling and Underground Construction Magazine*, (June):25–30.

Singha, K. and Gorelick, S. M. (2005). Saline tracer visualized with three-dimensional electrical resistivity tomography: Field-scale spatial moment analysis. *Water Resources Research*, 41(5):1–17.

Slater, L. (2007). Near surface electrical characterization of hydraulic conductivity: From petrophysical properties to aquifer geometries - A review. *Surveys in Geophysics*, 28(2-3):169–197.

Slater, L. and Binley, A. (1996). Determination of hydraulically conductive pathways in fractured limestone using cross-borehole electrical resistivity tomography. *European Journal of Environmental and Engineering Geophysics*, 1(1):35–52.

Slater, L., Binley, A. M., Daily, W., and Johnson, R. (2000). Cross-hole electrical imaging of a controlled saline tracer injection. *Journal of Applied Geophysics*, 44(2-3):85–102.

Slater, L. D., Binley, A., and Brown, D. (1997). Electrical Imaging of Fractures Using Ground-Water Salinity Change. *Ground Water*, 35(3):436–442.

Sopko, J. A. (2017). Coupled Heat Transfer and Groundwater Flow Models for Ground Freezing Design and Analysis in Construction. *Geotechnical Frontiers*, pages 1–11.

Sopko, J. A., Chamberland, R., and Washington, P. (2013). Remediation of Distressed Frozen Earth Cofferdams. In *International Conference on Case Histories in Geotechnical Engineering*.

Tripp, A. C., Hohmann, G., and Swift, C. (1984). Two-dimensional resistivity inversion. *Geophysics*, 49(10):1708.

Tsourlos, P., Ogilvy, R., Meldrum, P., and Williams, G. (2003). Time-lapse Monitoring in Single Boreholes Using Electrical Resistivity Tomography. *Journal of Environmental and Engineering Geophysics*, 8:1–14.

Van Nostrand, R. G. and Cook, K. L. (1966). *Interpretation of resistivity data*. Number 499.

Waxman, M. and Thomas, E. (1974). Electrical Conductivities in Shaly Sands-I. The Relation Between Hydrocarbon Saturation and Resistivity Index; II. The Temperature Coefficient Of Electrical Conductivity. *Journal of Petroleum Technology*, 26(2):213–226.

Wenner, F. (1912). The four-terminal conductor and the Thomson bridge. *Bulletin of the Bureau of Standards*, 8(3):559.

Wenner, F. (1916). A method of measuring earth resistivity. *US Department of Commerce and Labor, Bureau of Standards*, pages 469–478.

Wightman, D. M. and Pemberton, S. G. (1997). The Lower Cretaceous (Aptian) McMurray Formation; an overview of the Fort McMurray area, northeastern Alberta. *Petroleum geology of the Cretaceous Mannville Group, Western Canada. Memoir - Canadian Society of Petroleum Geologists*, Memoir 18:312–344.

Xiao, Z., Lai, Y., You, Z., and Zhang, M. (2017). The Phase Change Process and Properties of Saline Soil During Cooling. *Arabian Journal for Science and Engineering*, 42(9):3923–3932.

Zohdy, A. (1964). The auxilary point method of electrical sounding interpretation, and its relationship to the Dar Zarrouk parameters. In *34th Annual International SEG Meeting*.

Zohdy, A. and Jackson, D. (1969). Application of deep electrical soundings for groundwater exploration in Hawaii. *Geophysics*, 34(4):584–600.